UNIVERSITAT POLITÈCNICA
DE CATALUNYA
BARCELONATECH

Spatio-temporal quality metrics for satellite SAR interferometric data

Yismaw A. Wassie

ADVERTIMENT La consulta d'aquesta tesi queda condicionada a l'acceptació de les següents condicions d'ús: La difusió d'aquesta tesi per mitjà del repositori institucional UPCommons (http://upcommons.upc.edu/tesis) i el repositori cooperatiu TDX (http://www.tdx.cat/) ha estat autoritzada pels titulars dels drets de propietat intel·lectual **únicament per a usos privats** emmarcats en activitats d'investigació i docència. No s'autoritza la seva reproducció amb finalitats de lucre ni la seva difusió i posada a disposició des d'un lloc aliè al servei UPCommons o TDX. No s'autoritza la presentació del seu contingut en una finestra o marc aliè a UPCommons (*framing*). Aquesta reserva de drets afecta tant al resum de presentació de la tesi com als seus continguts. En la utilització o cita de parts de la tesi és obligat indicar el nom de la persona autora.

ADVERTENCIA La consulta de esta tesis queda condicionada a la aceptación de las siguientes condiciones de uso: La difusión de esta tesis por medio del repositorio institucional UPCommons (http://upcommons.upc.edu/tesis) y el repositorio cooperativo TDR (http://www.tdx.cat/?locale- attribute=es) ha sido autorizada por los titulares de los derechos de propiedad intelectual **únicamente para usos privados enmarcados** en actividades de investigación y docencia. No se autoriza su reproducción con finalidades de lucro ni su difusión y puesta a disposición desde un sitio ajeno al servicio UPCommons No se autoriza la presentación de su contenido en una ventana o marco ajeno a UPCommons (*framing*). Esta reserva de derechos afecta tanto al resumen de presentación de la tesis como a sus contenidos. En la utilización o cita de partes de la tesis es obligado indicar el nombre de la persona autora.

WARNING On having consulted this thesis you're accepting the following use conditions: Spreading this thesis by the institutional repository UPCommons (http://upcommons.upc.edu/tesis) and the cooperative repository TDX (http://www.tdx.cat/?locale- attribute=en) has been authorized by the titular of the intellectual property rights **only for private uses** placed in investigation and teaching activities. Reproduction with lucrative aims is not authorized neither its spreading nor availability from a site foreign to the UPCommons service. Introducing its content in a window or frame foreign to the UPCommons service is not authorized (framing). These rights affect to the presentation summary of the thesis as well as to its contents. In the using or citation of parts of the thesis it's obliged to indicate the name of the author.

UNIVERSITAT POLITÈCNICA
DE CATALUNYA
BARCELONATECH

SPATIO-TEMPORAL QUALITY METRICS FOR SATELLITE SAR INTERFEROMETRIC DATA

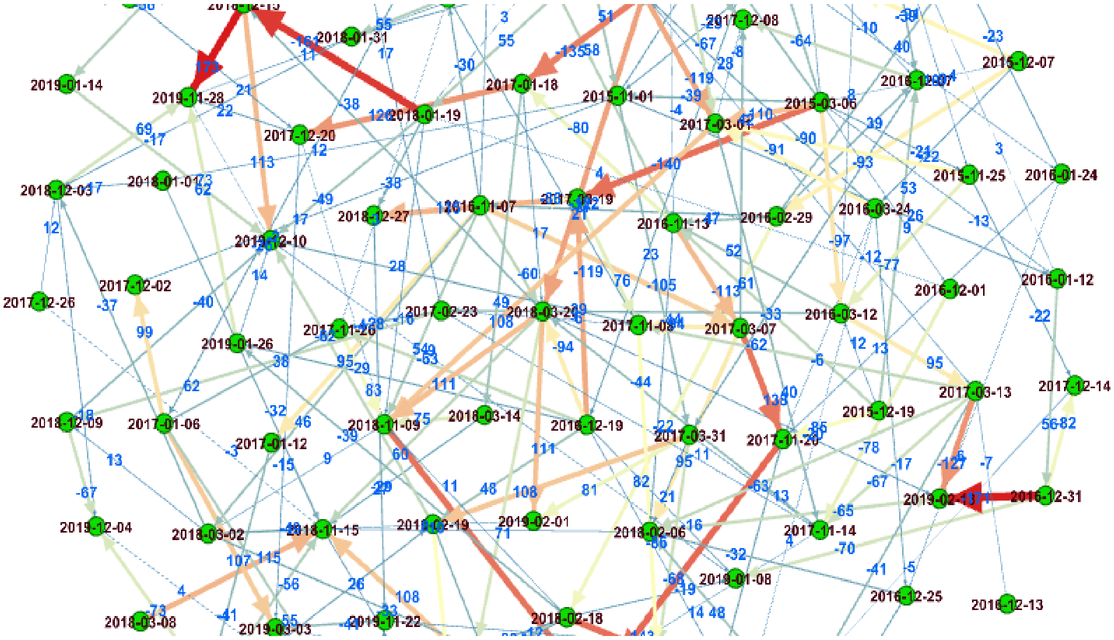

by

Yismaw A. Wassie

Barcelona, Spain

June 2023

SPATIO-TEMPORAL QUALITY METRICS FOR SATELLITE SAR INTERFEROMETRIC DATA

Yismaw A.Wassie

Supervisors:
Dr Michele Crosetto, CTTC
Dr Oriol Monserrat, CTTC

Tutor:
Prof Càrol Puig Polo, UPC

A PhD dissertation submitted to the Universitat Polytècnica
de Catalunya Doctoral School for the degree of
Doctor of Philosophy
in
Aerospace Science and Technology

Department of Physics
UNIVERSITAT POLITÈCNICA DE CATALUNYA (UPC)

Barcelona, Spain
June 2023

UNIVERSITAT POLITÈCNICA DE CATALUNYA
BARCELONATECH

cttc
Advanced research for everyday life

Spatio-temporal quality metrics for Satellite SAR Interferometric data

A PhD dissertation

By:

Yismaw A. Wassie

Supervisors:

Dr Michele Crosetto
Department of Remote Sensing, Geomatics Research Unit,
The Telecommunication Technology Center of Catalunya (CTTC)

Dr Oriol Monserrat
Department of Remote Sensing, Geomatics Research Unit,
The Telecommunication Technology Center of Catalunya (CTTC)

Tutor:
Prof Càrol Puig Polo
Department of Civil and Environmental Engineering, Polytechnic University of Catalonia (UPC)

ACKNOWLEDGMENT

First and foremost, I would like to express my deepest gratitude to my supervisor Dr. Michele Crosetto for the invaluable support, guidance, and constructive feedback he has provided throughout my dissertation development. His expertise and insights have been instrumental in shaping my research and the realization of the dissertation. His openness to discussion even during tight schedules has been a testament to his dedication to my success. I also owe my gratitude to my co-supervisor Dr. Oriol Monserrat who has always been around in times of need. His consistent encouragement and commitment to my success have also been a source of motivation and inspiration. I am also indebted to Professor Puig, my tutor, for the exceptional follow-up and support in ensuring a smooth and efficient period as a PhD student at UPC. I appreciate the time and effort, all my supervisors have invested in reviewing my work and providing constructive feedback that has greatly enriched the findings of the dissertation to its current form.

I am also deeply grateful to the AGUAR— Agència de Gestió d'Ajuts Universitaris i de Recerca, for sponsoring my PhD study covering various conferences and summer schools expenses at the international level that also enables me to share unforgettable experiences with experts in the field. The opportunity and support of the Centre Tecnològic de Telecomunicacions de Catalunya— CTTC, Universitat Politècnica de Catalunya—UPC, and Bahir Dar University—BDU have been immense as well. Moreover, I would like to

acknowledge the European Space Agency (ESA) for making Sentinel-1 data, used in this dissertation, available free of charge. The research facilities and resources at CTTC and UPC contributed to a huge extent in using those data and generally achieving the objectives of the dissertation. Of course, my experience wouldn't have been as smooth as it was, hadn't the Department of Mathematics at BDU supported and allowed me to pursue my study abroad.

I am thankful to all individuals who contributed to the PSIG processing and analysis tools and to colleagues at the remote sensing department of the Geomatics division at CTTC for the insights during the (in) formal discussions we held at different instances. The discussions were enlightening to deepen my knowledge in the field. Moreover, the experience with fellow PhD candidates and visiting researchers at CTTC were invaluable—I thank you all for making my time memorable despite the uncertain pandemic crisis. Last but not least, I would like to pass on my heartfelt gratitude to my family and friends for their unwavering moral support, understanding, and motivation. My appreciation also goes to all open source communities who have generously shared their knowledge, expertise, and time and contributed in some way or another to the success of my study.

Y.A.Wassie
Barcelona, Spain

SUMMARY

The increasing availability of RADAR images collected by constellations of satellites for monitoring Earth's surface and its changes over time prompt the development of several interferometric SAR (InSAR) algorithms and methodologies. The widely known Multi-temporal InSAR (MT-InSAR) techniques, generally, aim at extracting the temporal evolution of displacements of targets with coherent scattering behavior from a stack of SAR acquisitions that are taken from the same area and processed relative to temporal and spatial references. On the other hand, due to the complex nature of SAR measurements, addressing all possible model parameters in a comprehensive manner is still challenging and is a source of error and misinterpretation. As a well-established spaceborne geodetic technique with various applications, the accuracy of MT-InSAR products does matter, and hence potential error sources must be mitigated. The accuracy of displacement time-series (TS) estimates, in many cases, is governed by the quality and number of exploited images, associated interferograms, and selected measurement points. Such data and derived results are heavily influenced by factors, including environmental conditions at times of measurement acquisition and the processing algorithms used. Incomplete representations of factors in modeling MT-InSAR measurements may, as well, lead to omission errors and hence an incorrect estimation and interpretation of the displacement TS. Any uncertainty in the accuracy of the MT-InSAR products compromises their reliability in sensitive applications. In line with this, tools to detect, identify, and classify interferometric measurements that are particularly impacted by phase unwrapping (PhU) errors had been developed with the aim to identify and mitigate potential errors in the data— ultimately improving the quality and valuing the worth of MT-InSAR measurements. Thereby leveraging the power of the technique for a wide range of applications, including land subsidence analysis, and infrastructure monitoring.

These tools make use of estimated phase residuals derived from a redundant network of unwrapped interferograms to formulate threshold-based quality scores as indicators of the reliability of the measurement points, images in a TS, images, and interferograms. Multiple pairs of baseline-constrained Sentinel-1 SAR images were considered to assess the potential of the tools to automatically detect, identify, and mitigate errors in the framework of the PSIG processing chain. The techniques were applied pixel by pixel in space and time to associate reliability scores highlighting the influence of global and local PhU errors in the course of the phase estimation. Experiments from Sentinel-1 A/B SLC dataset had generally justified that error mitigation strategies which include the exclusion of less reliable measurements from the network had relieved the impacts of errors and improved the TS estimation. Another important aspect of the thesis is the use of the point score tool as a post-PhU pixel filtering technique. The methodology contributes by providing quantitative information on the percentage of reliable pixels immediately after the PhU step. The experiments in this regard justified that the tool adds extra dimensions to common pixel selection techniques and is responsible for mitigating limitations on PhU error correction methodologies. Using it in conjunction with existing point selection techniques further guaranteed the inclusion of reliable points in the process. Generally, the results demonstrated that the proposed techniques significantly improved the quality of InSAR data by, for instance, excluding erroneous points automatically from millions of measurement points. Besides, implications for various applications that rely on MT-InSAR datasets— such as those used in monitoring mining areas and infrastructures and those ground deformations induced either by natural or anthropogenic phenomena, have been justified. Potential avenues for future research to further improve the qualities of interferometric products including the quantification of interferometric measurement point location uncertainties are also envisioned.

RESUMEN

La creciente disponibilidad de imágenes RADAR, adquiridas por constelaciones de satélites para monitorear la superficie de la Tierra y sus cambios a lo largo del tiempo, ha impulsado el desarrollo de varios algoritmos y metodologías de SAR interferométrico (InSAR). Las conocidas técnicas Multi-temporal InSAR (MT-InSAR) tienen como objetivo extraer la evolución temporal de los desplazamientos de puntos medidos. Esto se realiza sobre blancos con un comportamiento de dispersión coherente en una pila de adquisiciones SAR sobre la misma área, que se procesan en relación con referencias temporales y espaciales. Debido a la naturaleza compleja de las mediciones SAR, abordar todos los parámetros posibles del modelo de manera integral sigue siendo un desafío y es una fuente de error y mala interpretación.

Como una técnica geodésica bien establecida y con varias aplicaciones, la precisión de los productos MT-InSAR es importante y, por lo tanto, se deben mitigar las posibles fuentes de error. La precisión de las estimaciones de las series de desplazamiento, en muchos casos, depende de la calidad y el número de imágenes explotadas, los interferogramas asociados y los puntos de medición seleccionados. Tales datos y los resultados derivados están fuertemente influenciados por diferentes factores, incluidas las condiciones ambientales en los momentos de adquisición de la medición y los algoritmos de procesamiento utilizados. Cualquier incertidumbre en la precisión de los productos

MT-InSAR compromete su fiabilidad en aplicaciones sensibles. En línea con esto, se han desarrollado herramientas para detectar, identificar y clasificar las mediciones interferométricas que se ven particularmente afectadas por los errores de desarrollo de fase, con el objetivo de identificar y mitigar posibles errores en los datos, mejorando en última instancia la calidad de las mediciones de MT-InSAR. Aprovechando así el potencial de la técnica para una amplia gama de aplicaciones, incluido el análisis del hundimiento de la tierra y el monitoreo de la infraestructura.

Estas herramientas utilizan residuos de fase estimados derivados de una red redundante de interferogramas enrollados para formular índices de calidad basados en umbrales como indicadores de la fiabilidad de los puntos de medición, de las imágenes en una serie temporal, en imágenes y en interferogramas. Se consideraron varios pares de imágenes SAR de Sentinel-1 con restricciones de referencia para evaluar el potencial de las herramientas para detectar, identificar y mitigar errores automáticamente en el marco de la cadena de procesamiento PSIG. Las técnicas se aplicaron píxel por píxel en el espacio y el tiempo para asociar índices de fiabilidad que resaltaran la influencia de los errores de desarrollado de fase globales y locales, en el curso de la estimación de fase. Los experimentos del conjunto de datos Sentinel-1 A/B SLC generalmente corroboran la estrategia de mitigación de errores, que incluyen la exclusión de mediciones menos confiables de la red aliviaron los impactos de los errores y mejoraron la estimación de las series temporales. Otro aspecto importante de la tesis es el uso de la herramienta de índice de fiabilidad score como técnica de selección de píxeles. La metodología contribuye proporcionando información cuantitativa sobre el porcentaje de píxeles fiables inmediatamente después del paso del desarrollo de fase. Los experimentos en este sentido justificaron que la herramienta agrega dimensiones extra a las técnicas comunes de selección de píxeles y es responsable de mitigar las limitaciones en las metodologías de corrección de errores de desarrollo. Usarlo junto con las técnicas de selección de puntos existentes garantizó aún más la inclusión de puntos fiables en el proceso. En general,

los resultados demostraron que las técnicas propuestas mejoraron significativamente la calidad de los datos InSAR, por ejemplo, al excluir puntos erróneos automáticamente a partir de millones de puntos de medición. Además, se han justificado las implicaciones para varias aplicaciones que se basan en conjuntos de datos MT-InSAR, como los que se utilizan para monitorear áreas e infraestructuras mineras y aquellas deformaciones del suelo inducidas por fenómenos naturales o antropogénicos. También se prevén posibles vías de investigación futura para mejorar aún más las cualidades de los productos interferométricos, incluida la cuantificación de las incertidumbres de ubicación de los puntos de medición interferométrica.

CONTENTS

LIST OF FIGURES

LIST OF TABLES

NOMENCLATURE

List of Abbreviations

APS	Atmospheric phase screen
COSMO-SkyMed	COnstellation of small Satellites for the Mediterranean basin Observation
CTTC	Centre Tecnològic de Telecomunicacions de Catalunya
DEM	Digital elevation model
DePSI	Delft persistent scatterer SAR interferometry SAR
DInSAR	Differential interferometric synthetic aperture RADAR
DS	Distributed scatterers
Envisat	Environmental Satellite
ERS	European Remote Sensing Satellite
ESA	European space agency
GACOS	Generic Atmospheric Correction Online Service for InSAR
GNSS	Global navigation satellite system
GPS	Global positioning system
ICEYE	Finnish small SAR satellite constellation
InSAR	Interferometric synthetic aperture RADAR

ISRO	Indian Space Research Organization
IW	”Interferometric Wide Swath” mode of SAR operation
LAMBDA	Least-squares AMBiguity Decorrelation Adjustment
LOS	Line of sight
LP_s	Low-pass spatial filter
LS	Least square
MCF	Minimum cost flow
MT-InSAR	Multi-temporal Interferometric Synthetic Aperture RADAR
NASA	National Aeronautics and Space Administration
NISAR	NASA-ISRO Synthetic Aperture Radar
PhU	Phase Unwrapping
PS	Persistent scatterers
PSI/PSInSAR	Persistent scatterer SAR interferometry
PSIG	Persistent scatterer SAR interferometry of the Geomatics research unit at CTTC
QI	Quality indicators
RADAR	Radio detection and ranging
RADARSAT	RADAR Satellite
RCC	Radar cross section
SAOCOM	Satélite Argentino de Observación Con Microondas
SAR	Synthetic aperture RADAR
SBAS	Small BAseline Subset
SCR	Signal to clutter ratio
Sentinel-1	Earth observation satellite mission by the European Space Agency
SHP	Statistically homogeneous pixels
SLC	Single Look Complex
SNR	Signal to noise ratio
StaMPS	Stanford Method for Persistent Scatterers

STUN	Spatio-Temporal Unwrapping Network
SVD	Singular value decomposition
TerraSAR-X	German Earth observation satellite
TOPS	Terrain Observation by Progressive Scans
TOPSAR	Terrain Observation with Progressive Scans SAR
TS	Timeseries
UTM	Universal Transverse Mercator
ZTD	Zenith total delay

CHAPTER 1

INTRODUCTION

1.1 Background

Spaceborne Synthetic Aperture RADAR (SAR) is an active remote sensing imaging system that provides information about a target surface by measuring reflected energy in the microwave region of the electromagnetic spectrum. Processing backscattered signals of SAR systems gives a complex-valued image, where the amplitude indicates the strength of the signal response of a resolution cell on the ground and the argument is interpreted as the phase shift between emitted and received signal. The phase is also interpreted as the fraction of one complete wave cycle and is determined primarily by the distance between the satellite antenna and the ground targets [1]. SAR images are considered one of the greatest technological leaps ever contributed to the field of remote sensing [2]. Since the early 1990s, broad and significant developments have emerged in using SAR technology for a wide range of remote sensing applications, especially DEM generation and deformation monitoring. The main data sources were ERS-1/2, Envisat and Radarsat. Later in 2014, the constellation of Sentinel-1 with a short revisit time–has further boosted the exploitation and development of Multi-temporal Interferometric SAR (MT-InSAR) techniques for monitoring natural resources and infrastructures. MT-InSAR, nowadays represents a mature and well-established technique that is widely applied for geophysical applications [3].

MT-InSAR techniques, generally, aim at extracting the temporal evolutions of deformations of targets with coherent scattering behavior from a stack of SAR acquisitions of the same area relative to spatial and temporal references. Specifically, surface deformation maps, and displacement timeseries of target points are main products of a standard MT-InSAR analysis from interferometric measurements. Interferometric measurements are obtained by computing the phase difference between complex-valued SAR images acquired over the same area, taken from slightly different sensor positions [4]. The technique can detect subtle surface deformations with wide coverage and high spatial resolution [5]. Its capability to deliver measurements in all weather conditions and in locations that are inaccessible, remote, or hazardous [6] is also a plus compared to traditional geodetic techniques. Such advantages make the approach applicable for monitoring ground deformation induced by natural (e.g., landslides, volcanic eruptions, glaciers and earthquakes) and anthropogenic phenomena resulted from the extraction or injection of resources such as water, gas, salt, and oil [1], [7]–[11].

In the broader sense, MT-InSAR techniques include Persistent Scatterer (PS) methods [12] that identify pixels based primarily on their amplitude variation in time or the Small BAseline Subset (SBAS) approach [13] which considers the correlation of phases in space [7] mainly to respond to one of the limits of the PS techniques–low measurement point density in non-urban areas [13], [14], by incorporating so-called distributed scatterers (DS). Because of the reflection dominance of PSs within a resolution cell—the PS techniques are resistant to geometric and temporal decorrelations [12]. On the other hand, to reduce those effects— SBAS approach seeks to minimize the spatial and temporal baselines [7]. In doing so, thresholds of baselines may sometimes result in multiple independent subsets. In this case, a Singular Value Decomposition (SVD) method becomes a viable option to link measurements from different subsets as in the work of [15]. Prior to the extension of the method to full resolution [16], the primary focus of SBAS method was to estimate large-scale deformations from lower-resolution multi-looked SAR images. Generally, SBAS techniques are often convenient in peri-urban areas and the PS interferometry (PSI) technique is proved effective in urban areas due to the dominance of man-made features [17]. Besides, in contrast to PS pixels that are characterized by one dominant scatterer, DS pixels contain multiple independent scatterers that are statistically homogeneous and partially coherent within a resolution cell [18]. A hybrid of PS and DS [7], [19] techniques is also another approach commonly practiced with the objective to increase the density of measurement points and to maximize the amount of information to be retrieved from interferograms [20]. This approach addresses decorrelation noise relative to DSs by retrieving the optimized phase history of all possible interferometric pairs [18]. With unprecedented big InSAR datasets coming from current and future satellite missions (such as: Sentinel-1, NISAR, Capella, ICEYE, refer to Figure 2.5 for more), the computational efficiency of PS and DS methods is; however, questionable [20]. For SB analysis the problem, however, can be relieved by excluding some of the images [20]. Sequential estimation of deformation parameters [21], [22] can also play substantial role.

Many variants of the above MT-InSAR algorithms have also been adapted at different blocks of the respective MT-InSAR processing chain— the optimal phase estimation based on integer least square (LS) [23], the phase triangulation algorithm [19], or adaptive phase optimization [18] are among the techniques employed to improve estimated phase quality. Use of low and high pass filters to lessen the effects of the atmospheric phase screen after the PhU is also among the strategies. StaMPS [24] method employs a spatially correlated deformation with no prior assumption about its temporal nature. The PSs in this case are selected using a PS probability estimator based on the dispersion of amplitudes and a temporal measure of the phase noise coherence. A method that exploits both the StaMPS and SBAS interferogram configurations is also used as well [7]. Moreover, STUN [25], [26], adapt the LAMBDA method by exploiting a bootstrap estimator with an integer LS search to perform the temporal PhU before the spatial PhU. It uses a stochastic model to describe the atmosphere term. DePSI [27] also makes use of the integer LS, bootstrap and ambiguity function to resolve the temporal ambiguity function, followed by a spatial PhU in the first-order network of PSs, which is later densified after the APS filtering. Likewise, the phase inversion algorithm based on ℓ_1- norm minimization [28] and phase closure technique [29] have also been implemented to correct PhU errors. A combination of temporal and spatial [30] or 3D PhU algorithms have also been discussed in literature [31]–[33].

Baseline differences, atmospheric effects and land cover changes appear to threaten the success of many of the above methods and hence the qualities of final products. Abrupt topographic changes, high deformation gradient, discontinuities and/or noise are among the triggering factors that often lead to the failure of commonly used Itoh's smoothness assumption [34]– that partly attributes to the so-called PhU errors. Particularly, the estimated time series qualities are impacted by the spatial density of measurement points, signal to noise ratio of radar targets, locations of the reference point and number and temporal distributions of image acquisitions. Besides, considering the spectrum of quality indices— the ensemble coherence estimator, the covariance matrix of the parameters, the variance factor, the standard deviation of displacements and the spatio-temporal consistency test are among the techniques worth mentioning [35]. All except the ensemble coherence are insensitive to PhU errors [35]. On the other hand, the model dependence of the ensemble coherence metric [12] on the reference point makes it difficult to draw the reliability of delivered results [36]. The spatio-temporal consistency index [36] is, as well, spatially variable and its contribution is hindered for sparsely distributed measurement points. Nonetheless, the spatio-temporal PhU [37], [38] is yet a challenging problem that leads to the incorrect estimation of deformation time-series (TS). The inevitable nature of the errors, as well as the issue being barely addressed so far, and due to the in-sensitiveness of already available quality estimates to PhU errors calls for more quality metrics [35].

1.2 Objectives

This thesis is aimed at developing a tool to detect, identify, and classify MT-InSAR measurements thereby retrieving reliable products by resolving PhU errors. Particularly, the thesis is devoted to:

- investigate the sources of PhU errors in MT-InSAR and their impact on deformation measurements.
- formulate quality indicators to MT-InSAR measurements processed in the framework of small baseline MT-InSAR processing chain.
- associate a reliability flag highlighting the influence of PhU errors to measurement points, interferograms, images and images in a TS.
- propose and validate an extended point selection strategy from quality scores.
- evaluate the effectiveness of the proposed methods on a real-world Sentinel-1 datasets.

The tools make use of estimated phase residuals derived from a redundant network of unwrapped interferograms to formulate threshold-based quality scores as indicators of the reliability of the measurements. Multiple pairs of baseline-constrained Sentinel-1 SAR images were considered to assess the potential of the tools to automatically detect, identify, and mitigate errors in the framework of the PSIG processing chain. Using a redundant network, in this case, contributed to the detection of reliable measurements by uncovering gross and systematic errors affecting estimated TS [39], [40]. Generally, complementing MT-InSAR processing chains with such QIs will facilitate interpretations of products and help to build the trust and confidence of end users to integrate MT-InSAR products in their decision-making, as well.

To illustrate the proposed approach, the thesis is delimited to the small baseline methodology from Sentinel-1 SAR single-look complex (SLC) datasets. Sentinel-1 is a two-satellite constellation, designed and developed by ESA and funded by the European Commission, with the primary objective of providing C-Band SAR data continuity following the end of ERS-1/2 and ENVISAT missions. The repeat cycle has been notably reduced from 35 days for ERS-1 and ERS-2 or 30/35 days for ENVISAT to 6 days for Sentinel-1A/B satellite constellation[†]. Sentinel-1 constellation provides a large geographical coverage, and rapid data dissemination to support operational applications, such as land monitoring or emergency services. The first satellite of the constellation, Sentinel-1A, was launched on April 2014, following which the second satellite, Sentinel-1B, was launched in April 2016. The default acquisition mode of Sentinel-1 for land services corresponds to the interferometric wide swath with TOPS [42]. In this acquisition mode, the radar beam scans back and forth three times within a single swath, referred to as sub-swaths, resulting in a higher quality and homogeneous image throughout the swath, compared with scanSAR. This choice of the dataset has rooted in the fact that a fully connected interferograms network can be easily guaranteed, and hence an unbiased small baseline network inversion could be achieved from Sentinel-1 constellation [43]. For this purpose, Sentinel-1 SLC datasets accessed from NASA's Alaska Satellite Facility platform (`https://search.asf.alaska.edu`) or the European Space Agency (ESA) Open Access Data Hub (`https://scihub.copernicus.eu`) were used. The processing and analysis of intermediate and final outputs were then performed in the framework of the PSI processing chain, PSIG [44] of the Geomatics research unit of the Centre Tecnològic

---

[†] As Sentinel-1B satellite terminates its operation on December 23, 2021, currently the only operational Sentinel-1 satellite is Sentinel-1A with a revisit time of 12 days [41].

de Telecomunicacions de Catalunya (CTTC).

1.3 Thesis outline

The thesis is organized into five chapters. Preliminary concepts that are essential blocks for the rest of the chapters, from the theoretical to the practical perspectives, are presented in chapter two. It incorporates the main MT-InSAR principles, models, and the generic processing chain involving phase inversion and spatiotemporal PhU techniques. The third chapter is dedicated to brief quality metrics and their formulations which is one of the main contributions of the thesis. The main processing chain of the thesis and associated uncertainties in MT-InSAR techniques are also discussed here. Proposed metrics are illustrated with real redundant Sentinel-1 datasets in chapter four. This also includes the applications and demonstrations of QIs as an extended version of commonly used MT-InSAR measurement point selection strategies. Finally, a summary of the main contributions and future perspectives is presented in the fifth chapter. Articles and conference papers published in the course of this thesis development are also presented in the appendices section along with other supplementary information.

CHAPTER 2

MT-INSAR DATA PROCESSING AND ANALYSIS FUNDAMENTALS

2.1 Introduction

The synthetic aperture in SAR imaging system is used to simulate a larger antenna aperture by combining multiple radar signals collected over a distance traveled by a moving antenna. The technique improves the resolution of the SAR image, allowing for more detailed information to be extracted from the radar data. By considering the phase difference of two SAR images, the change in distance between the satellite and the ground surface can be estimated for the purpose of monitoring infrastructures, mining activities or land subsidence due to groundwater extraction or oil and gas production. A stack of such SAR images is combined and analyzed using MT-InSAR techniques to create a time series of measurements that show the stability of target points on the surface of the earth over time. Main preliminary concepts including InSAR principles, models and MT-InSAR processing chain involving phase inversion and spatio-temporal phase unwrapping techniques are reviewed in this chapter.

2.2 InSAR Principles

The principle of Satellite InSAR is based on the interference of two SLC SAR images acquired from slightly different positions at different times. As the phase information of SLC images is proportional to the sensor-target distance in the range direction, the phase difference between two images can be exploited to derive information about the displacement of a target during two SAR image acquisitions. This section presents satellite SAR missions, acquisitions geometry, working principles and generic interferometric data processing algorithms.

2.2.1 SAR image acquisition

Interferometric SAR data can be generated by employing along-track, across-track, or repeat-track interferometry [4], [45]. The latter one also called repeat-pass interferometry, is the focus of this thesis — requires precise flight path location to effectively realize its objectives. It has a proven success record for satellite SAR missions [45]. The geometric aspect of the repeat pass interferometry is illustrated in Figure 2.1 for satellites supposed to take scenes at times t_1 and t_2 respectively from positions p_1 and p_2.

SAR imaging system uses the motion of a satellite to create a large ”synthetic” antenna aperture that allows the technique to capture high-resolution images of the Earth’s surface from space. While the satellite is moving, SAR sends out a series of radar pulses and records the return echoes. One of the fundamental equations in radar theory— the radar equation, relates the received power to the transmitted power, the radar cross-section (RCS) of the target ρ^0, the range to the target, R and the properties of the radar system.

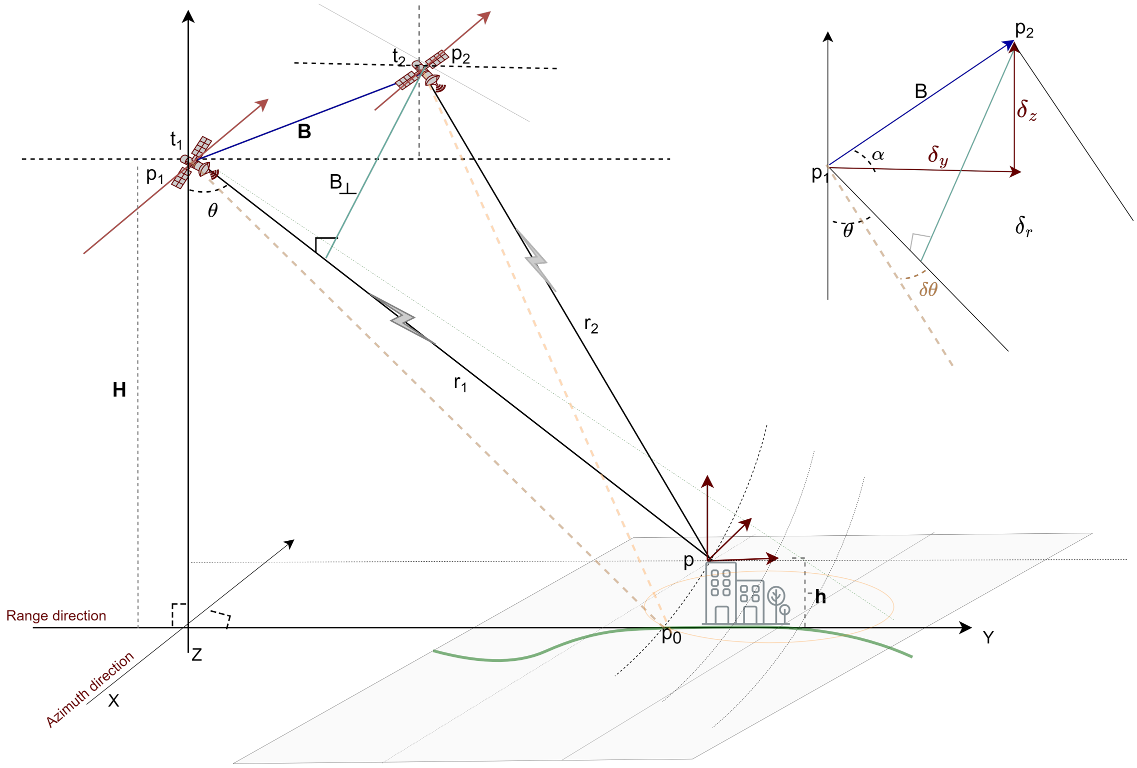

Figure 2.1: Geometry of repeat-pass SAR interferometry.

The equation can be expressed as [46], [47]:

$$P_r = P_t \times \frac{G^2 \lambda^2 \rho^0}{(4\pi)^3 R^4 a_k} \tag{2.1}$$

where P_r is the received power, P_t is the transmitted power, G is antenna gain, λ is the wavelength of the radar signal, and a_k stands for the losses related to absorption in the propagation medium. The a_k term is a rather complex function that takes into account the dimensions and the dielectric constants of the scatterer material and depends on the frequency and polarization of the incident wave. By combining the echoes from many different pulses, taken over a period of time, SAR is able to build up a detailed picture of the Earth's surface. In this regard, the azimuth and range resolutions are among the crucial parameters that determine the level of detail in the radar image.

2.2.1.1 Azimuth and range resolutions

As the satellite moves, each new pulse overlaps with the previous pulse, effectively extending the length of the antenna which is the key to achieving high azimuth resolution. The azimuth resolution is determined by the width of the radar beam in the cross-range direction and the speed at which the radar platform is moving. A narrower beam and slower platform speed will result in better azimuth resolution [48], [49].

$$\alpha_{az_{\text{max}}} = \frac{L_s}{2} \tag{2.2}$$

where L refers the antenna size. This result shows that the azimuth resolution is equal to half the size of the physical antenna and is independent of the distance between the sensor and the target point. Moreover, for two point targets that are separated in the slant range direction by $\delta\rho_s$, the corresponding echoes will be separated by a time difference δt equal to:

$$\delta t = \frac{2\delta\rho_s}{c} \tag{2.3}$$

where c is the speed of light and factor 2 is account for the signal round-trip propagation. As the smallest separable time difference in the radar receiver is equal to the effective time length τ of the pulse, the ground range resolution is given by [48], [49]:

$$\begin{aligned} \delta r_{\text{g}} &= \frac{c\tau}{2\sin\theta} \\ \delta r_{\text{g}_{\text{max}}} &\approx \frac{c}{2B_w} \quad \text{for} \quad B_w \approx \frac{1}{\tau} \quad \text{and} \quad \theta = \frac{\pi}{2}\text{rad} \end{aligned} \tag{2.4}$$

where c is the speed of light, θ is the incident angle and B_w is the bandwidth of the radar system. A wider bandwidth means higher resolution and better target identification but requires more power and can suffer from more interference. On the other hand, narrower bandwidth means lower resolution, but higher efficiency and less susceptibility to interference. In general, there are often trade-offs between the azimuth and range resolution parameters which makes it challenging to achieve higher resolutions in both dimensions simultaneously. For example, a shorter pulse duration can improve range resolution but may also reduce the amount of energy in the radar pulse, leading to a lower signal-to-noise ratio and reduced sensitivity. Similarly, a narrower beam can improve azimuth resolution at the expense of the amount of energy that is transmitted toward the target, which can again lead to a lower signal-to-noise ratio and reduced sensitivity. For further reading on SAR image formation algorithms, readers are advised to refer [46], [50]–[52] among many other resources in the field.

2.2.1.2 SAR measurements

To acquire a radar image, a side-looking radar sensor from space transmits a signal to the Earth and measures the complex return of the back-scattered pulses. The received signals are digitized and stored together with annotated transmission/reception times and create raw data with coarse resolution in the flight direction due to physical length restrictions of the radar antenna [53]. The fact that every target on earth is illuminated by many pulses during the sensor trajectory, the raw data are subsequently combined to build a long antenna and create a SAR image with much higher resolution [53]. In a SAR image, a pixel is sampled in an azimuth and slant-range coordinate system associated with a unique rectangular resolution cell on the ground. Each pixel of a focused SLC image corresponds to a complex number, Z that carries the amplitude A and the fractional phase of the received signal denoted by Φ.

$$\mathrm{Z} = \mathrm{A}\exp(\mathrm{j}\Phi), \quad \text{for} \quad \Re(\mathrm{Z}) = \mathrm{A}\cos\Phi \quad \Im(\mathrm{Z}) = \mathrm{A}\sin\Phi \quad \text{and} \quad \mathrm{j}^2 = -1 \tag{2.5}$$

where A $= \sqrt{(\Re(Z))^2 + (\Im(Z))^2}$ and $\Phi = \arctan\frac{\Re(Z)}{\Im(Z)}$. In Equation 2.5, j stands for the imaginary unit and the $\Re(Z)$ and $\Im(Z)$ respectively denote the real and imaginary parts of the complex signal Z. While amplitude values are associated with the amount of electromagnetic energy backscattered towards the sensor, phase values are related to the sensor-to-target distance, called the (slant) range and denoted by **r**. The range can be expressed as an integer number of wavelengths, λ plus any fraction of a wavelength remaining. Hence, the phase recorded by the radar signal would either be zero or just this fraction of a cycle— ranging from 0 to 2π as phase values are known modulo 2π. Properties of scatterers in a scene and sensor parameters like wavelength, polarization, look angle, and resolution affect SAR image pixel brightness. The dominant parameters generally influencing the radiometric interpretation of SAR images are surface roughness, local incidence angle, scatterer density and dielectric constant [54].

2.2.1.3 SAR Interferometry

In the case of repeat-pass interferometry, a single SAR satellite system illuminates the same area at different times and map reflected signals from slightly different orbits. The resulting SAR image is a two-dimensional array of pixels of observed targets on the ground-range plane projected onto the slant-range plane. Set of phase differences derived from a pair of SAR images forms an important class called interferograms. For two coregistered SLC images $\mathfrak{C}_m$ and $\mathfrak{C}_n$, the interferogram is the set of phase differences obtained by multiplying elements of $\mathfrak{C}_m$ with the complex conjugate of the corresponding element of $\mathfrak{C}_n$ (Equation 2.6) and will have the same geometry as the input images:

$$Z_{\mathfrak{C}_m} Z^*_{\mathfrak{C}_n} = |Z_{\mathfrak{C}_m}|\,|Z_{\mathfrak{C}_n}|\, e^{j\Delta\Phi_{mn}} \tag{2.6}$$

where $\Delta\Phi_{mn}$ is the wrapped phase difference of $Z_{\mathfrak{C}_m}$ and $Z_{\mathfrak{C}_n}$ and $*$ is the complex conjugate operator. That is, if ${\mathfrak{C}_m}^{\Phi}$ and ${\mathfrak{C}_n}^{\Phi}$ are sets of phases associated to images $\mathfrak{C}_m$ and $\mathfrak{C}_n$, respectively, then the interferogram in the azimuth-range plane can be described in a set as: $\{\Delta\Phi_{\mathrm{mn}} : \Delta\Phi_{\mathrm{mn}}(x,y) = \Phi_{\mathrm{n}}(x,y) - \Phi_{\mathrm{m}}(x,y) \wedge \Delta\Phi_{\mathrm{mn}}(x,y) \in [-\pi,\pi)$ for $\Phi_{\mathrm{m}} \in \mathfrak{C}_{\mathrm{m}}{}^{\Phi}$ and $\Phi_{\mathrm{n}} \in \mathfrak{C}_{\mathrm{n}}{}^{\Phi}\}$. Figure 2.2 illustrates examples of interferogram and amplitude images derived from a complex SLC image. SAR interferometry is applied in geophysical monitoring of natural hazards (earthquakes, volcanoes, landslides), time-series analysis of surface deformation (subsidence, uplift, and structural stability analysis), topographic mapping, and glacier motion analysis.

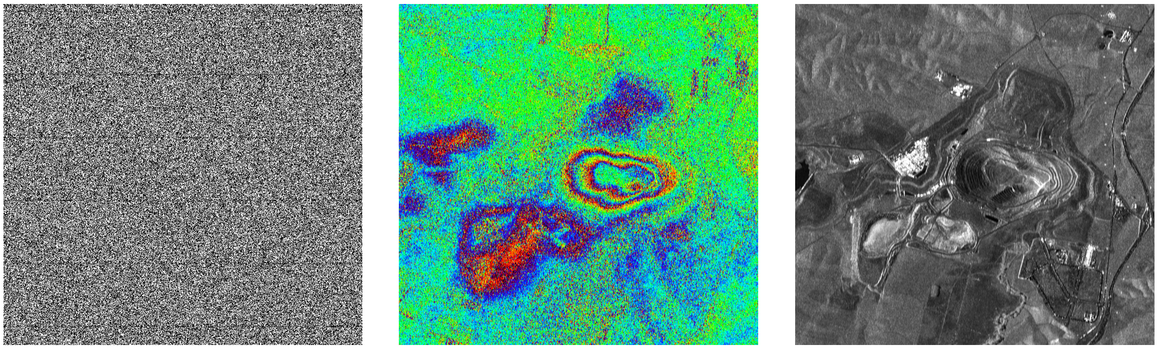

(a) Complex measurements (b) Phase differences (c) Mean amplitudes

Figure 2.2: Example of a subset of a complex image (a) interferogram (b) and mean amplitude image (c) from Sentinel-1 satellites in the radar geometry taken from a copper mine area in Sevilla, Spain. The interferogram has a perpendicular baseline of 145m and a temporal baseline of 6 days derived from images acquired on 2017-12-23 and 2017-12-29. The color codes (dark blue to red) in (b) represent wrapped values in $[-\pi,\pi)$. The mean amplitude information was computed from 123 images in ascending mode.

2.2.2 Interferometry for topographic mapping

When two radar satellites from different positions, say p_1 and p_2, image the same point, p on the ground— using the two-way travel of the signals, the phase difference $\varphi = \Delta\Phi$ can be written in terms of the slant range differences, δr as

$$\varphi \approx \frac{4\pi}{\lambda}\delta r \tag{2.7}$$

Denoting $\mathbf{r}$ for $|\overrightarrow{p_1p}|$, we get $|\overrightarrow{p_2p}| = \mathbf{r} + \delta\mathbf{r}$. Making use of the parallel ray approximation [55], the following equations can be derived.

$$(\mathbf{r} + \delta\mathbf{r})^2 = \mathbf{r}^2 + B^2 - 2\mathbf{r}B\sin(\theta - \alpha) \tag{2.8}$$

where α is the baseline tilt angle. Since $\delta r << \mathbf{r}$, we also have [56]:

$$\delta\mathbf{r} = \frac{B^2}{2\mathbf{r}} - B\sin(\theta - \alpha) \tag{2.9}$$

Since $B << \mathbf{r}$, from Equation 2.7 is rewritten as:

$$\varphi = \frac{-4\pi}{\lambda} B\sin(\theta - \alpha) \tag{2.10}$$

From which, we also derive:

$$\delta\varphi = \frac{-4\pi}{\lambda} B\cos(\theta - \alpha)\delta\theta \tag{2.11}$$

where $B_\perp = B\cos(\theta - \alpha)$ is the perpendicular baseline component. To see the effect of local topography on the interferometric phase, let's consider a target point p_0 located on the reference plane. Using Equation 2.10 the phase shift at p_0 is reformulated as:

$$\varphi_0 \approx \frac{-4\pi}{\lambda} B\sin(\theta_0 - \alpha) \tag{2.12}$$

where θ_0 represents the look angle corresponding to p_0. Flattened phase difference which is obtained by removing the flat Earth phase is [56]:

$$\delta\varphi_{flat} \approx \frac{-4\pi}{\lambda} B\cos(\theta_0 - \alpha)\delta\theta \tag{2.13}$$

Moreover, the height above the reference datum of point, p as a function of the phase difference is given by [1]:

$$h_p = -\frac{\lambda}{4\pi}\frac{r\sin(\theta_0)}{B\cos(\theta_0-\alpha)}\delta\varphi \tag{2.14}$$

Equation 2.14 illustrates the height ambiguity associated to the phase difference $\delta\varphi$. Equivalently, the phase difference due to topography is:

$$\delta\varphi_{topo} = -\frac{4\pi}{\lambda}\frac{B_\perp}{r\sin(\theta_0)}h_p \tag{2.15}$$

Equ 2.15 indicates the sensitivity of the height and the perpendicular baseline are directly proportional.

However, to fully exploit the potential of the satellite SAR technique, the various components leading to the phase difference should be resolved. As demonstrated from Equation 2.7- 2.15, the occurrence of backscatter phase change between observations and the effect of the atmosphere contributes to the range difference and hence hinders isolating parameters of interest from interferograms. Prior information such as precise orbital info, DEM, ground truth, meteorological data, or phase contributions due to atmospheric propagation delay change are among the rich information to be used in the phase compensation. Section 2.3 is devoted to addressing most of these parameters. Likewise, Section 2.2.3 presents geometric distortions resulting from changes in the viewing angle of a satellite SAR system. SAR satellite missions and Sentinel-1 satellite constellation, in particular, are also discussed in Section 2.2.4.

2.2.3 Geometric distortions

In zero Doppler coordinates, the SAR imaging geometry is approximated by the azimuth and the range [57]. The former refers to the relative position along the antenna flight trajectory, and the latter indicates the distance of a point in a plane orthogonal to the antenna trajectory. Due to the side-looking viewing geometry (Figure 2.3) inherent to

Satellite SAR imaging systems, terrain features often appear to be distorted.

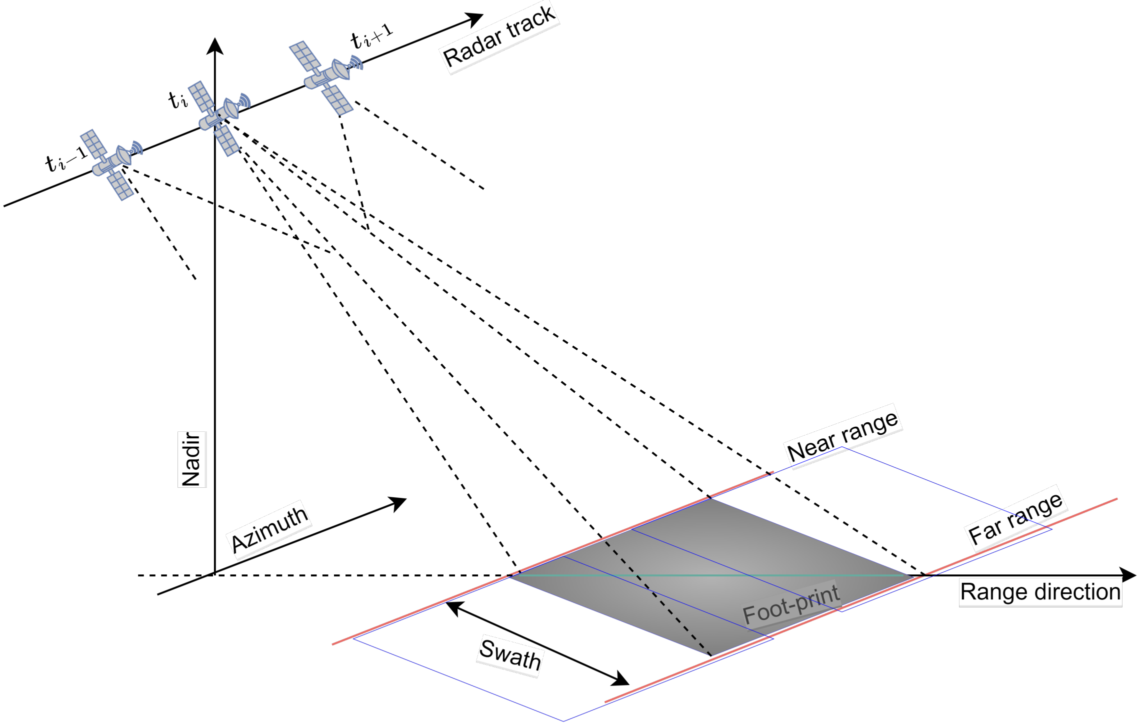

Figure 2.3: Side-looking radar imaging geometry

Widely known effects include: foreshortening, layover, and shadow [49], [58] (Figure 2.4). Foreshortening corresponds to compression or dilation of the resolution pixel on the ground and layover produces an inversion of the image geometry. Shadow, on the other hand, doesn't produce any backscatter signal and, as a result, has no contribution to the image geometry [49]. As can be seen from Figure 2.4(a), the slope between points A and B will get foreshortened into the image area $A'B'$. The amount of foreshortening depends both on the system's look angle θ and on the slope angle α, and reaches its maximum if $\theta \rightarrow \alpha$. Once the slope angle exceeds the incidence angle, the slope produces a layover. For instance, in layover situations— the tops of mountains are imaged ahead of their base (see projections of points B and C in Figure 2.4(b)) and backscatter from mountain slopes

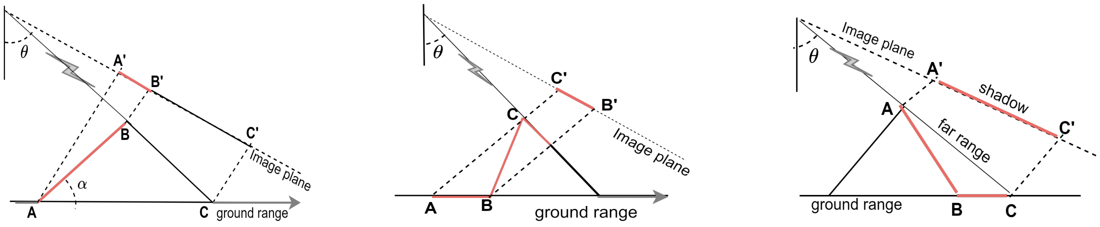

(a) Foreshortening (b) Layover (c) Shadow

Figure 2.4: Examples of geometric distortions: Foreshortening ($-\theta < \alpha < \theta$), layover ($0 < \alpha < \theta$) and shadow ($\alpha \leq \theta - \frac{\pi}{2}$).

will overlay with image information at closer and farther image ranges. Both foreshortening and layover can be reduced if the look angle θ is increased; however, larger θ will, on the other hand, create an image shadow (Figure 2.4(c)). Hence, topography-related image distortions cannot be entirely removed, and image acquisitions from more than one viewpoint may be necessary to minimize all three imaging effects jointly.

2.2.4 SAR Satellite missions

Multiple SAR satellites revolve along near-polar orbits providing observation data with different frequencies and resolutions for various applications. These SAR systems have an oblique imaging geometry with respect to the flight direction that can either be ascending or descending. The satellite viewing direction is called the line of sight (LoS) with inclination angle (θ) ranging from 20 to 50° from the nadir [59]. A list of some satellite SAR missions with their sensor parameters is presented in Figure 2.5. The width of a swath, the strip of an imaged scene in the range dimension, varies per acquisition mode from 30 km to 500 km [60].

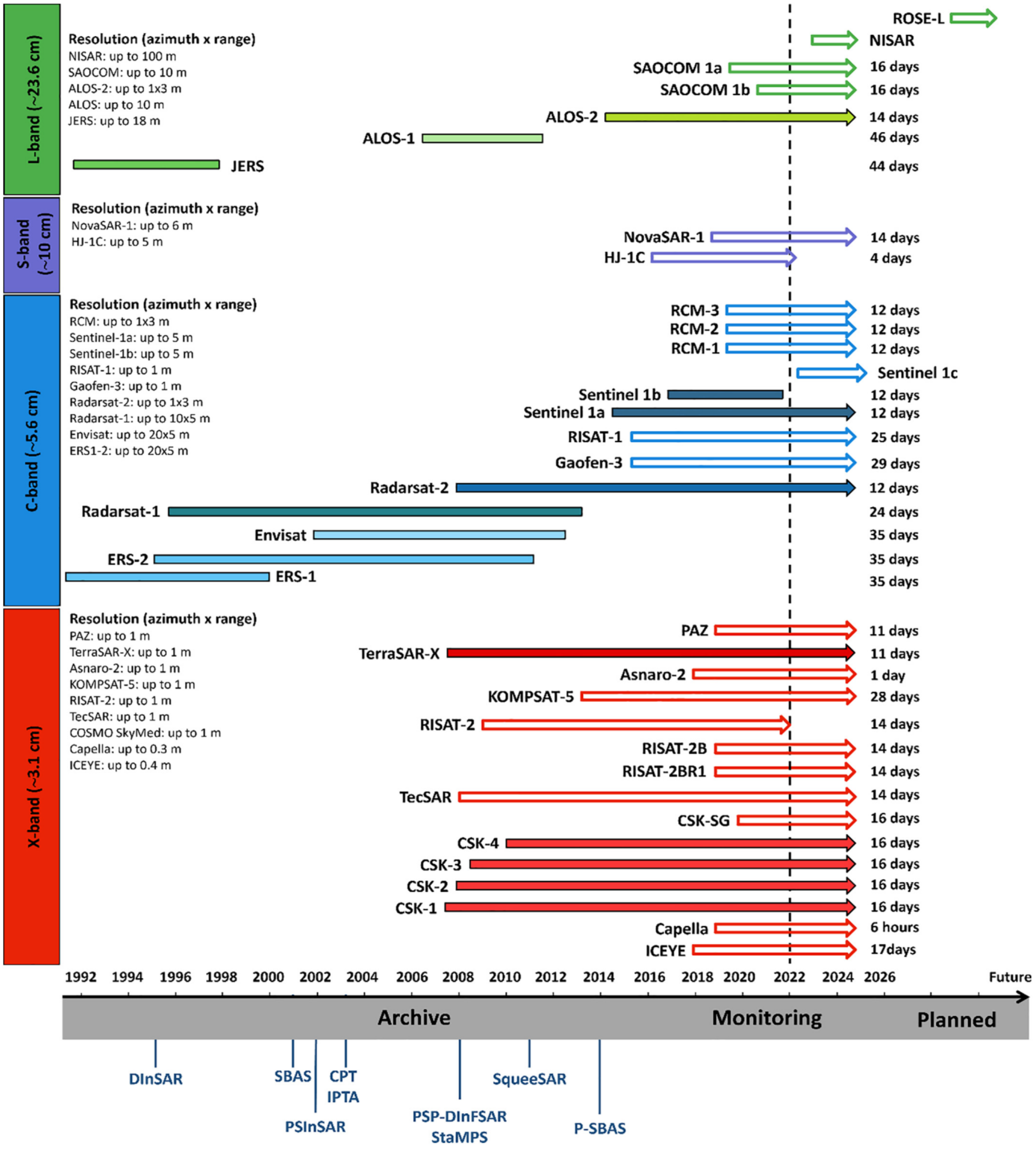

Figure 2.5: Past, present and future SAR missions since 1990 and their main features [41], [59], [61], [62]. The resolution corresponds to the maximum spatial resolution that the sensor can achieve in meters. The solid fill in the horizontal strips represents satellite platforms that have been adopted for subsidence analysis [61].

The spatial distance between two acquisition spots is termed as the interferometric baseline and the projection of this baseline along the direction perpendicular to the satellite LoS is called the perpendicular baseline. Besides, the minimum time interval required for a satellite to overpass the same area is known as temporal baseline (discussed in sections 2.2.1 & 2.3). Current SAR satellites missions have achieved a higher temporal baseline of up to a day (as in the case of the COSMO-SkyMed as a constellation of multiple satellites), 3 days (e.g. TerraSAR-X and PAZ) or 6 days (as in Sentinel-1A/B). Launched in 1978, SEASAT was the first Earth observation satellite to provide SAR data suitable for interferometry [58]. The importance of SEASAT's SAR data for topographic mapping was demonstrated 8 years later by [55], and for detection and mapping of small elevation changes [58], [63]. Some of the satellites, such as ERS and Envisat, are no longer operative but have provided valuable archives of data that are still used for studying past deformation phenomena. Recently launched satellites or those in the pipeline will play a substantial role in ensuring the sustainability of the techniques and in systematic monitoring of deformations of the Earth's surface.

2.2.4.1 Sentinel-1 constellation

Sentinel-1 mission, the focus of the thesis, operates in four exclusive imaging modes with different resolutions–down to 5 m and coverage–up to 400 km. It provides dual polarisation capability, very short revisits times and delivers products with a free data access policy. For each observation, precise measurements of spacecraft position and altitude are available [41]. Sentinel-1 missions cover all global landmasses, coastal zones, and shipping routes at high resolution (Figure 2.6). These benefits, along with the planned mission of Sentinel-1C/D— ensure the reliability of the service in providing long-term data archives for long-time series applications [41]. The Interferometric Wide (IW) swath mode, in particular, is the main acquisition mode that acquires data with a 250 km swath at 5 m by 20 m spatial resolution (single look). IW mode captures three sub-swaths using Terrain

Observation with Progressive Scans SAR (TOPSAR). With the TOPSAR technique, in addition to steering the beam in range, the beam is also electronically steered from backward to forward in the azimuth direction for each burst, resulting in homogeneous image quality throughout the swath [42].

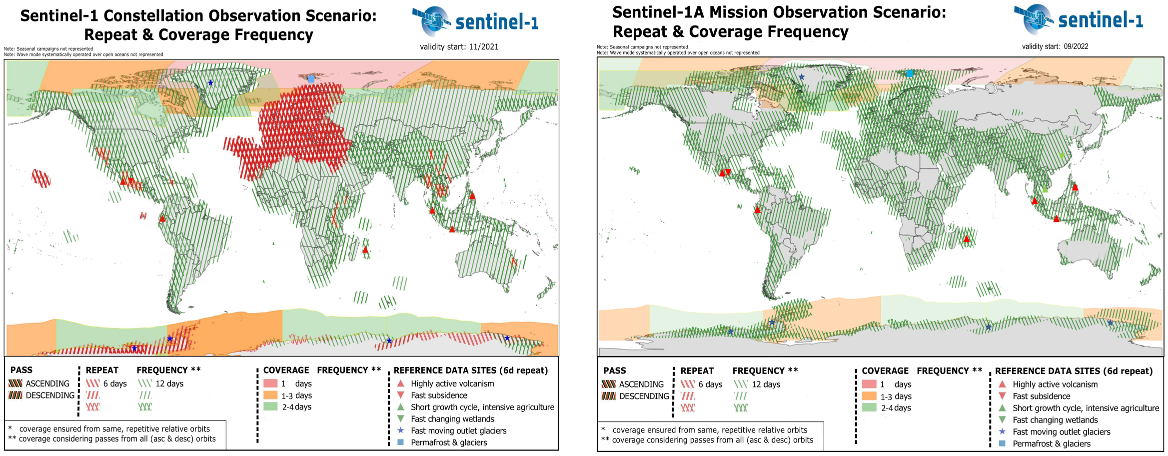

(a) (b)

Figure 2.6: Sentinel-1 constellation data acquisition mode and the global coverage: (a) coverage and observation scenarios of the two Sentinel-1A/B satellites before December 23, 2021 and (b) the coverage and observation scenario of only Sentinel-1A satellite after the termination Sentinel-1B mission on December 23, 2021 [41].

SLC products, whose product parameters are summarized in Table 2.1, contain one image per sub-swath and one per polarisation channel, for a total of three (single polarisation) or six (dual polarisation) images in an IW product. Each sub-swath image consists of a series of bursts—usually nine, where each burst has been processed as a separate SLC image. The individually focused complex burst images are included, in azimuth-time order, into a single sub-swath image with demarcation in between. There is sufficient overlap between adjacent bursts and between sub-swaths to ensure continuous coverage of the ground. The images for all bursts in all sub-swaths are resampled to a common pixel spacing grid in range and azimuth while preserving the phase information [41].

Table 2.1: Sentinel-1 Interferometric Wide Swath Mode, SLC image product parameters.

System parameter	Value
Sensor	C-band SAR
Pixel value	Complex
Orbit	Ascending/Descending
Antenna	Right looking
Wavelength	5.547 cm
Incidence angle range	29.1°-46.0°
Spatial resolution (rg x az)	5 m x 20 m
Pixel spacing (rg x az)	2.3 m x 14.1 m
Number of sub-swath	3
Azimuth steering angle	± 0.6°
Ground swath width	250 km
Min/max orbit height	698/726 km
Polarization options	Single (HH or VV) or Dual (HH+HV or VV+VH)

2.3 MT-InSAR data processing and analysis

The estimation of displacement time-series from a stack of interferograms is the main objective to be addressed. Different data-driven approaches customized depending upon the test land cover, size of the area being processed, topography and deformation type are among the considerations. Besides, MT-InSAR derived products can be affected by the quality of parameters retrieved from the satellite system (incidence angle, spatial resolution, system noise), orbit (baseline), signal (frequency, polarization, noise), topography (slope direction, surface characteristics), and atmosphere condition [45]. Thus, an interferometric phase in the direction of radar LOS, denoted by $\Delta\Phi^{t_{\alpha\beta}}$ for image acquisitions times between t_α and t_β, can be modeled as a linear combination of contributions of phase components the following way [1], [13]:

$$\Delta\Phi^{t_{\alpha\beta}} := \Delta\Phi_d^{t_{\alpha\beta}} + \Delta\Phi_t^{t_{\alpha\beta}} + \Delta\Phi_a^{t_{\alpha\beta}} + \Delta\Phi_n^{t_{\alpha\beta}} + 2k^{t_{\alpha\beta}}\pi \tag{2.16}$$

For a transmitted signal wavelength λ,

$\Delta\Phi_d^{t_{\alpha\beta}} \approx \frac{4\pi}{\lambda}\mathrm{D}_{los}$ stands for the LOS cumulative deformations from times t_α to t_β with respect to t_0—the reference time.

$\Delta\Phi_t \approx \frac{4\pi}{\lambda}\frac{B_{\perp k}}{R\sin\vartheta}\Delta \mathrm{h}_{t_{\alpha\beta}}$ refers the residual topography induced on phase, Δh is the difference in height between the DEM and effective target. $b_\perp$ is the interferometric perpendicular baseline, ϑ is the looking angle and R the slant-range distance from the sensor to target.,

$\Delta\Phi_a$ is the phase contribution due to the change in the atmosphere at times of image acquisition, and $\Delta\Phi_n$ is the noise component due to the change in the scattering behavior of the target and/or systems thermal noise and k is the phase ambiguity due to the wrapped nature of phase measurements. As extracting the deformation phase term is the objective of MT-InSAR techniques, other interferometric phase components of Equation 2.16 should be removed or compensated (refer to Figure 2.7 for a generic processing flow). Often, external DEM and precise orbital information are used to compensate for the deterministic $\Delta\Phi_t$ term. Note that the $\Delta\Phi_t$ term exists even after using a DEM. The noise component accounts for many factors, including temporal, geometric, and Doppler centroid decorrelations [1]. Changes in the scattering properties of the scatterers over time contribute to temporal decorrelation, and geometric decorrelations are attributed to differences in the incidence angle during acquisitions. The Doppler centroid decorrelation, on the other hand, is caused by differences in the Doppler centroid frequencies between acquisitions. The atmospheric artifacts $\Delta\Phi_a$ and the noise term $\Delta\Phi_n$ along with phase error contributions from the unwrapping procedures will be discussed in Sections 2.3.3 and 2.3.4.

2.3.1 Measurement point selection techniques

The reflected signal of a SAR pixel is the coherent sum of contributions from the scatterer(s) within the pixel footprint. Among millions of available points, the point selection step aims to identify those potential points with relatively reliable signals for displacement

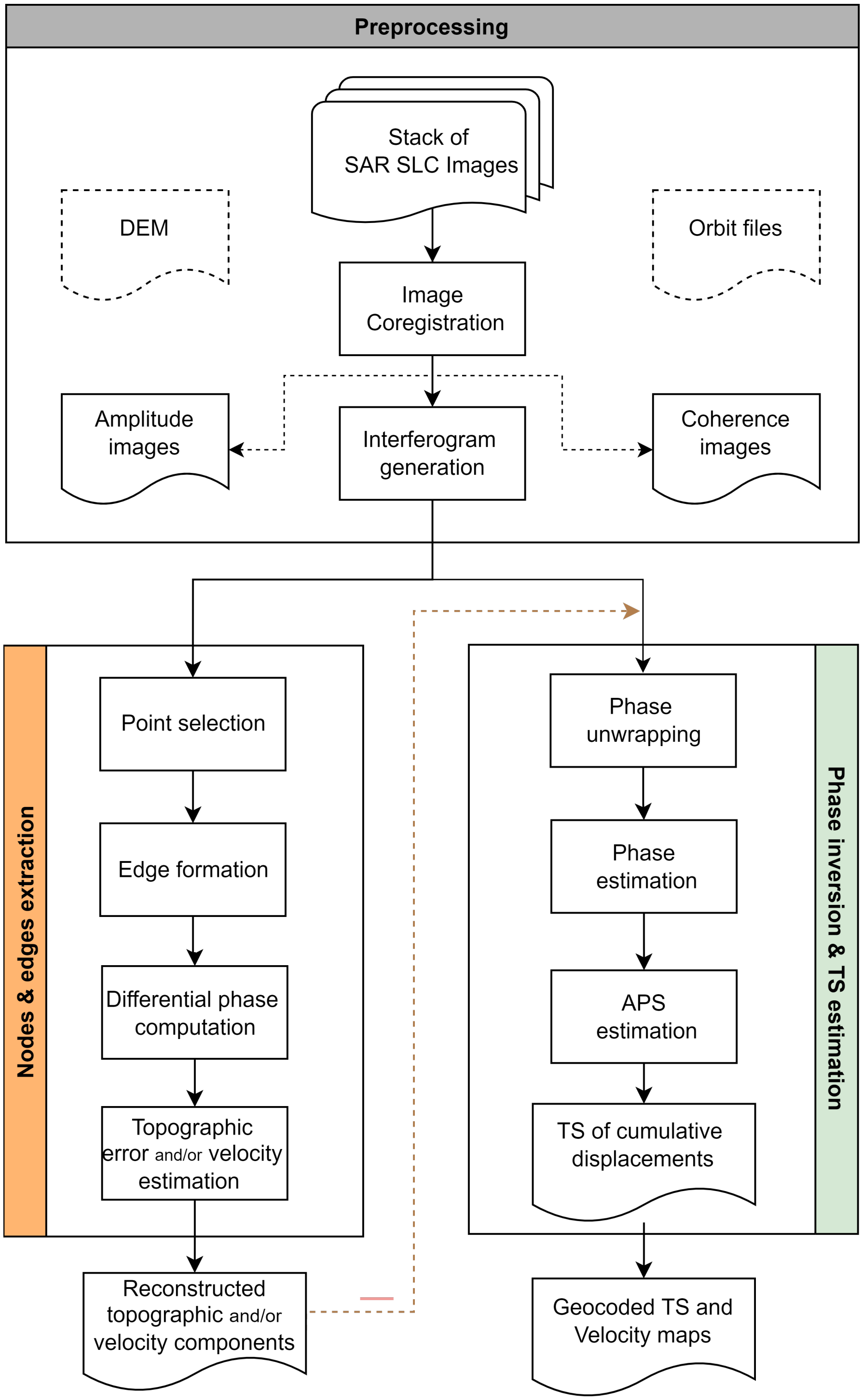

Figure 2.7: Generic MT-InSAR processing workflow, in this context, nodes and edges respectively refer the selected points and the corresponding edges connecting the points in the spatial domain. The DEM and orbit files used in the pre-processing are also required at the geocoding step.

analysis. At this step, often a trade-off between the quality and the spatial density of points is taken into consideration. There are, in general, two dominant categories of scatterers—one is the so-called deterministic scatterer or Permanent Scatterer (PS) which are class of time-invariant points in the full TS and the other category includes Distributed Scatterers (DS) that are partially decorrelated and show a relatively lower signal-to-noise ratio in the TS. The temporal coherence criterion [24], the maximum likelihood estimation [64], [65] and phase stability criteria [66] are also other worth mentioning criteria used to select target points. Below common pixel selection strategies for MT-InSAR data processing are briefly discussed.

2.3.1.1 Deterministic scatterers selection

A common selection criterion for such pixels is— using the degree of fit between the phase variation of pixels in time to a temporal model [12]. However, due to different phase contributions within the resolution cell, the observed wrapped interferometric phases cannot be used directly to identify these PSs. Rather, the temporal amplitude stability criteria is used as an indicator of phase stability and hence to select candidate PSs [23]. Putting it into context, the normalized amplitude dispersion index as an approximation of phase standard deviation, D_A [12] is given by Equation 2.17. This is done under the assumption the noise component of contributions of scatterers within a pixel follows circular complex Gaussian distribution. A threshold on DA is used to select candidate PSs with stable phase behavior.

$$D_A = \frac{\sigma_A}{m_A} \tag{2.17}$$

where σ_A and m_A refer to the standard deviation and mean of the temporal amplitude evolution, respectively. A linear relation between the D_A and the standard deviation of the phase noise has been indicated for small D_A values [58]. The D_A criterion preserves the full resolution of a SAR image and it has no theoretical limitation on the length of interferometric baselines, as the temporal and geometrical decorrelations are supposed to be minimal. Nevertheless, it has the disadvantage of low density of selected pixels, especially in non-urbanized areas where DSs account for the majority.

2.3.1.2 Distribute coherent scatterers selection

The complex spatial correlation coefficient of two SAR images is known as coherence. A high coherence implies a consistent phase relationship between the neighboring points. Phase stability is analyzed on the assumption that phase is spatially correlated, which leads to the averaging of the phases of neighboring potential PSs and selecting the point targets with the lowest residual noise. The complex coherence of a given interferogram is a statistical index that measures the degree of correlation between the pair of complex SAR images that constitute the interferogram. It is an estimate of spatial coherence used to select coherent DSs [67]. The complex coherence of two zero-mean complex signals ζ_1 and ζ_2 is defined as:

$$\gamma = \frac{\mathbb{E}[\zeta_1 \zeta_2^*]}{\sqrt{\mathbb{E}[|\zeta_1|^2] . \mathbb{E}[|\zeta_2^*|^2]}} \tag{2.18}$$

where $\mathbb{E}[.]$ and $*$ stand for the expectation and complex conjugate operators, respectively. However, the accuracy of phase observations of a locally homogeneous region is assumed to be stationary and under spatial ergodicity assumption, the expectation operator in Equation 2.18 is replaced by the spatial average, leading to the following maximum likelihood estimator:

$$\gamma(\mathrm{i},\mathrm{j}) = \frac{\left|\sum_{j=1}^{n}\sum_{i=1}^{m} \zeta_1(i,j)\zeta_2^*(i,j)\right|}{\sqrt{\sum_{j=1}^{n}\sum_{i=1}^{m} |\zeta_1(i,j)|^2 \sum_{j=1}^{n}\sum_{i=1}^{m} |\zeta_2^*(i,j)|^2}} \tag{2.19}$$

where (i,j) stands for the location of the pixels within the $m \times n$ window involved in the spatial averaging.

2.3.2 Interferograms network

An interferogram network refers to a set of interferograms that are formed by combining multiple SAR images acquired at different times with the ultimate goal of estimating the displacement of the ground surface over time. Depending on the specific application and the characteristics of the area being monitored, various alternatives are available to configure such a network, and typical of them, are briefly described below. For the purpose of convenience, ℓ interferograms generated from N SAR images that are acquired in an ordered time sequence $\{\mathrm{t_i}\}_{i=0}^{\mathrm{N}-1}$ and coregistered to the same geometry are considered. Besides, in Figure 2.8 to 2.10, green and red boxes refer to the parent images and associated interferograms forming the network.

One-to-all network: In this type of network, all the images will be connected to a single image called the master image. As a result of which it is also called a single-master interferogram network. The edge connecting the nth image $\mathfrak{C}_\mathrm{n}$ with the the fixed master image $\mathfrak{C}_0$ is denoted by ℓ_n and named the nth interferogram. Such network of interferograms can be formulated as:

$$\mathrm{G} = \{\mathrm{V}, \mathrm{E}\} \text{ where } \mathrm{V} = \{\mathfrak{C}_\mathrm{n} \text{ for } 0 \leq \mathrm{n} \leq \mathrm{N}-1\} \text{ and } \mathrm{E} = \{\ell_\mathrm{n} : \ell_\mathrm{n} = \overline{\mathfrak{C}_0\mathfrak{C}_\mathrm{n}} \quad \text{for} \quad 1 \leq \mathrm{n} \leq \mathrm{N}-1\} \tag{2.20}$$

The bar in $\overline{\mathfrak{C}_0\mathfrak{C}_\mathrm{n}}$ is to indicate the edge connecting $\mathfrak{C}_0$ and $\mathfrak{C}_\mathrm{n}$. Moreover, at each pixel position (x, y) the nth interferometric phase is computed as $\Phi_\mathrm{n}(x, y) = \arg(\mathrm{Z}_{\mathfrak{C}_0}\mathrm{Z}^*_{\mathfrak{C}_\mathrm{n}})$ — the same way as elaborated in Section 2.2.1.3. A sample pictorial representation of single master interferogram configurations is shown in Figure 2.8. Images, in this case, are nodes of interferograms, and the edges or interferograms indicated by ℓ_n's are a 2D array of phase values derived from the parent images. This also holds true for Equations 2.21 and 2.22.

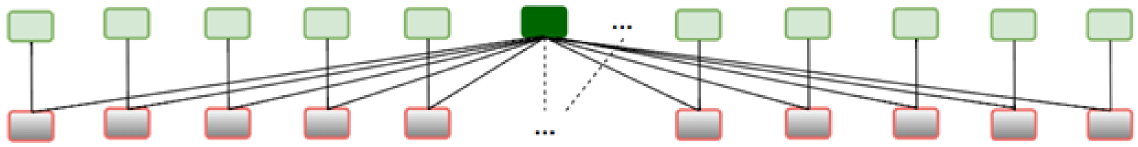

Figure 2.8: Sample single-master interferogram network configuration.

Redundant network: In this case, an edge/interferogram is formed between images whose temporal and spatial baselines are bounded with predefined thresholds. The resulting network is also widely known as a small baseline interferogram network. Unlike the single-master network configuration case, it leads to a multi-master configuration (Figure 2.9). In principle, it is possible to generate $\mathrm{N}(\mathrm{N}-1)/2$ interferograms from N available SAR images. However, due to the restriction of the spatiotemporal baselines, the number of interferograms would be less than or equal to the maximum number of interferograms. Denoting the edge ℓ_{mn} formed between the mth and nth images by $\overline{\mathfrak{C}_{\mathrm{m}}\mathfrak{C}_{\mathrm{n}}}$, the network can be described as:

$$\begin{aligned} &\mathrm{G} = \{\mathrm{V'}, \mathrm{E}\} \text{ where } \mathrm{V'} \subseteq \mathrm{V} = \{\mathfrak{C}_{\mathrm{m}} \text{ for } 0 \leq m \leq \mathrm{N}-1\} \text{ and} \\ &\mathrm{E} = \left\{\ell_{\mathrm{mn}} : \ell_{\mathrm{mn}} = \overline{\mathfrak{C}_{\mathrm{m}}\mathfrak{C}_{\mathrm{n}}} \text{ for } |\mathrm{t}_{\mathfrak{C}_{\mathrm{m}}} - \mathrm{t}_{\mathfrak{C}_{\mathrm{n}}}| \leq \mathrm{B}_{\mathrm{t}} \wedge |\mathrm{P}_{\mathfrak{C}_{\mathrm{mn}}}| \leq \mathrm{B}_{\perp}\right\} \end{aligned} \tag{2.21}$$

$\mathrm{P}_{\mathfrak{C}_{\mathrm{m}}}$ is the perpendicular baseline between node $\mathfrak{C}_{\mathrm{m}}$ and $\mathfrak{C}_{\mathrm{n}}$. B_{t} and $B_{\perp}$ respectively refer to the temporal and perpendicular/spatial baseline thresholds.

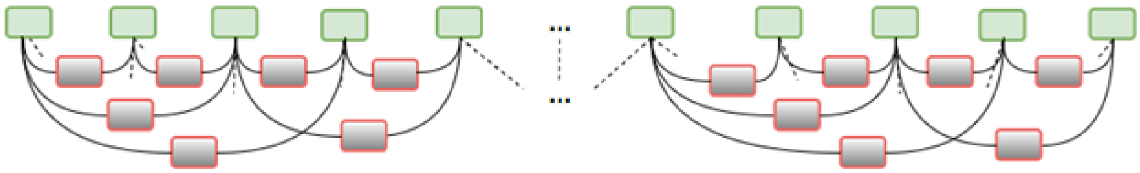

Figure 2.9: Redundant interferogram network configuration.

Sequential network: Such networks are formed between consecutive images as presented in Figure 2.10. It is a connected graph with $N - 1$ interferograms/edges formed from N SAR images as in the case of the single master case. The temporal baseline that defines this network is given by: $B_t = \max|\Delta b_m|$ where$\Delta b_m = t_{\mathfrak{C}_{m+1}} - t_{\mathfrak{C}_m}$ and $t_{\mathfrak{C}_m}$ is meant the acquisition date of node $\mathfrak{C}_m$ for $0 \leq m \leq N - 1$.

$$\begin{aligned} &G = \{V, E\} \text{ where } V = \{\mathfrak{C}_m \text{ for } 0 \leq m \leq N-1\} \text{ and} \\ &E = \left\{\ell_m : \ell_m = \left\{\overline{\mathfrak{C}_m \mathfrak{C}_{m+1}} \text{ for } |t_{\mathfrak{C}_{m+1}} - t_{\mathfrak{C}_m}| \leq B_t, 0 \leq m < N-1\right\}\right. \end{aligned} \tag{2.22}$$

$t_{\mathfrak{C}_m}$ is the date corresponding to node $\mathfrak{C}_m$. When we have identical temporal resolutions between consecutive images and when $B_t = |t_{\mathfrak{C}_{m+1}} - t_{\mathfrak{C}_m}|$ setting aside $B_\perp$, the multi-master configuration would be considered as a generalization of the direct integration technique. In such interferogram configuration, PhU errors can be propagated to the estimated time series [68]. This is an important drawback of using a simple network, which does not provide any redundant observation.

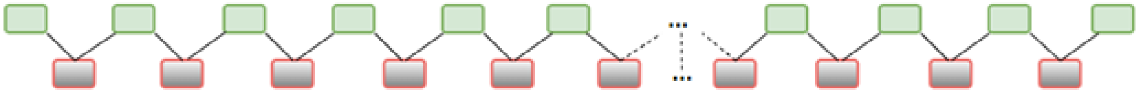

Figure 2.10: Sequential interferogram network configuration

Alternatively, full stacking of interferograms [19] or statistical homogeneity test [23] for pixel selection can also be employed to estimate MT-InSAR deformation time-series products. Overall, the choice of interferogram network or pixel selection strategies depends on the processing chain to work on, the case area, the quality to achieve, and also on the computational time and space available.

Generally, MT-InSAR processing techniques differ mainly in the rules used to choose the image pairs and the optimal phase estimation approaches followed. Based on which, three categories— PSI, SBAS, and PS-DS methods can be established. PSI [12] techniques use the phase information of multiple SAR images to identify and track coherent point-like targets, called persistent scatterers. These targets have high coherence over time, which allows for precise measurements of their deformation. The technique is useful for monitoring long-term and slow deformation and can provide very high spatial resolution measurements at individual point-like targets.

As the name indicates, the second category—SBAS [13] follows the redundant interferogram configuration strategies and only those image pairs fulfilling the baseline threshold criteria are involved in the TS phase estimation. This improves the capabilities of the technique to provide spatially dense deformation maps, which is a key feature of MT-InSAR interferometry [73].

In the case of the PS-DS method (such as: [19])— PS scatterers are identified in the interferograms, and their stable phase values are used as a reference to calibrate the phase values of the DS scatterers. The calibrated phase values of the DS scatterers are then used to generate high-resolution deformation maps. Implementation of this technique involves generating $N(N-1)/2$ interferograms from a set of N images by the multilook estimates of the coherence matrices. Next, all those interferograms would be exploited to pick N-1 of them with better phase estimates. Following which, similar steps as the PSI algorithms will be implemented to remove decorrelation signals and estimate parameters of interest. As the first SBAS [13] method is formulated for multilook images, it may fall short of studying local deformations. To address this limitation the method was later extended for full-resolution datasets [16]. Common MT-InSAR timeseries deformation approaches from the past two decades are summarized in Table 2.2.

2.3.3 Phase unwrapping in spatial domain

Due to the configuration of the satellite SAR system's signal transmitting and receiving models, it is possible to extract only the absolute phase modulo 2π called the wrapped

Table 2.2: Characteristics of the main InSAR time series approaches, [17], [20], [35]

Method	Interferogram network	Pixel selection criteria	Assumptions/Remarks	Reference
PSI	Single master	Amplitude Dispersion	Linear deformation in time	[12]
StaMPS	Single master	Amplitude dispersion	Spatial smoothness	[24]
STUN	Single master	Amplitude dispersion & SCR		[26]
DePSI	Single Master	Amplitude dispersion	Deformation model in time	[35]
	Small baseline	Amplitude dispersion & Cousin PS	Spatial smoothness	[44]
SBAS	Small baseline	Coherence	Spatial smoothness	[13]
	Small baseline	Coherence	linear deformation	[15]
	Small baselines	Coherence	Spatial & temporal smoothness	[69]
SBAS+	Small baseline	Mean spatial coherence	Spatial smoothness & full-resolution	[16]
			Stepwise linear function	[70]
			Spatial and temporal smoothness	[69]
SqeeSAR	Single master after phase triangulation	Statistically homogeneity	Linear deformation in time	[19]
StaMPS+	Single master & small baseline	Phase stability	Spatial smoothness & 3D phase unwrapping	[7]
PS-DS	Full stacking	Statistically homogeneity	Linear deformation, Phase linking & multiple scattering	[71]
	Small baseline	Statistically homogeneity	Linear deformation	[72]

phase [20]. For most MT-InSAR applications including deformation monitoring, principal phase values should be unwrapped by a phase unwrapping method. The method reconstructs the unknown absolute phases φ from wrapped phases Φ by removing the 2π multiple ambiguities and it is formulated as in Equation 2.23.

$$\varphi = \Phi + 2k\pi, \quad \text{for} \quad \Phi \in [-\pi, \pi) \quad \text{and} \quad k \in \mathbb{Z}. \tag{2.23}$$

The unwrapping problem is inherently undetermined and hence non-unique. As a consequence, it is impossible to solve the problem without any a-priori assumption about the signal of interest. Particularly, in the case of single baseline InSAR—the dominant assumption is the phase difference of adjacent samples is not more than half a wave cycle—Itoh's smoothness condition [34]. Under this criterion, the true phase gradient field is assumed to be a conservative potential field—in which case the curl of the gradient field is zero [58].

However, steep slopes that lead to high phase derivatives or low coherences may lead to the failure of Itoh's condition among many other factors [58]. Unless corrections at PhU steps are done, estimated deformation phases appear to incorporate PhU errors that also result in distortions in the heights of measurement points [49]. Accordingly, in the past couple of decades, different PhU approaches aimed at achieving a better phase estimation have been proposed in time and/or space domains [30], [32], [35], [37], [39], [74]–[79].

Common unwrapping approaches in MT-InSAR methodologies [12], [35] use assumptions on the relative deformation behavior of nearby pixels in time, defining the problem in the time domain. The advantage of using relative phases between two nearby pixels is that the contribution of atmospheric and orbital errors will then be minimal due to their high spatial correlation. In this method, phase time series per arc are unwrapped relative to pre-defined temporal models by simultaneously estimating model parameters and relative topographic phase. Temporally unwrapped phases are then integrated spatially per interferogram to obtain the final unwrapped time series. Alternatively, every interferogram is unwrapped spatially by the minimum cost flow approach [80] after unwrapping arc phases in time assuming no phase jump larger than π between two adjacent acquisitions is detected. The unwrapped phases are then used to assign, the parameters of the cost function required by MCF method. Under the simplest scenario, the absolute spatial phase gradient between neighboring pixels $\mathfrak{p}$ and $\mathfrak{q}$ is estimated as:

$$\Delta\varphi_{\mathfrak{p}\mathfrak{q}} = \begin{cases} \Phi(\mathfrak{p}) - \Phi(\mathfrak{q}) & \text{if} \quad -\pi \leq \Phi(\mathfrak{p}) - \Phi(\mathfrak{q}) < \pi \\ \Phi(\mathfrak{p}) - \Phi(\mathfrak{q}) - 2\pi & \text{if} \quad \Phi(\mathfrak{p}) - \Phi(\mathfrak{q}) \geq \pi \\ \Phi(\mathfrak{p}) - \Phi(\mathfrak{q}) + 2\pi & \text{if} \quad \Phi(\mathfrak{p}) - \Phi(\mathfrak{q}) < -\pi \end{cases} \tag{2.24}$$

Then, the absolute phase of each pixel is determined by a simple integration process from a known reference point. Figure 2.11 shows an example of TS of displacements in mm affected by phase unwrapping errors.

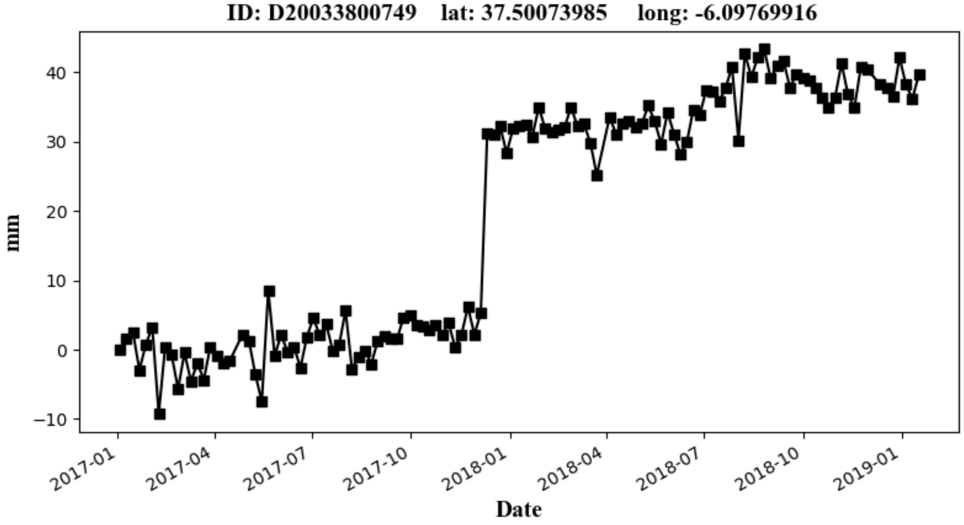

Figure 2.11: An example of displacement TS affected by an unwrapping error observed after processing 124 Sentinel-1 SLC images from a Copper mining area, Spain.

Some of the common approaches for phase unwrapping in the space domain are briefly discussed below.

2.3.3.1 Branch-cut method

The branch-cut PhU [74] is a technique used to abandon phase discontinuities or jumps in a signal, by selecting a branch cut in the complex plane and adding an integer multiple of 2π across the cut to make the phase function continuous. To reduce the effect of noise transmission, the method iteratively estimates the unwrapped phase values starting from a reference point but averting the integration path from crossing the branch cuts [81]. The objective function of the shortest path for the $m \times n$ interferogram can be formulated as [81]:

$$\min\left\{\sum_{i=0}^{m-2}\sum_{j=0}^{n-1}\aleph_1(i,j)+\sum_{i=0}^{m-1}\sum_{j=0}^{n-2}\aleph_2(i,j)\right\} \tag{2.25}$$

where the values of $\aleph_1$ and $\aleph_2$ are either 1 (if branch-cut exists) or 0 (otherwise). The main advantage of the algorithm includes— its relatively high processing speed. A wrong selection of branch cuts, however, may lead to wrong PhU results [82]. Moreover, areas that are confined by residue cuts are sometimes inaccessible to the algorithm, resulting in spatially incomplete solutions.

2.3.3.2 Least square estimation

The least-squares method seeks to minimize the sum of the squared differences between the observed phase values and the unwrapped phase values, subject to constraints such as smoothness and continuity. The method is computationally efficient when they make use of fast Fourier transform techniques [78], [83], [84]. However, the accuracy of the unwrapping result is sometimes impacted by the dispersion of the errors across multiple measurement points [80]. These errors will also propagate over the entire interferogram and potentially distort the reconstructed phase globally [78], [80], [85]. Defining discrete partial derivatives as $\Delta_x(i,j) = \Phi(i+1,j) - \Phi(i,j)$ and $\Delta_y(i,j) = \Phi(i,j+1) - \Phi(i,j)$, the LS- PhU algorithm tries to minimize the following expression.

$$\sum_{i=0}^{m-2}\sum_{j=0}^{n-1}[\varphi(i+1,j) - \varphi(i,j) - \Delta_x(i,j)]^2 + \sum_{i=0}^{m-1}\sum_{j=0}^{n-2}[\varphi(i,j+j) - \varphi(i,j) - \Delta_y(i,j)]^2 \tag{2.26}$$

The algorithm can be formulated in (un) weighted forms that can further be reduced to the discrete Poisson equation [83], [86], [87]. The Fast Fourier transform, the discrete cosine transform or the Picard iteration method are among the approaches used to address the problem. Unlike the Branch-cut method, by the LS method unwrapping can be done everywhere in the spatial domain and any value may be added to the measurements to ensure continuity in the solution. However, the solution is still found to underestimate the phase slope [88].

2.3.3.3 Minimum cost flow method

This section is devoted to a special case of ℓ_p norm minimization that received a great deal of attention—called the minimum cost flow (MCF) method. The MCF method treats the PhU problem as a graph optimization problem, where the nodes in the graph represent the phase values and the edges represent phase differences between adjacent pixels. The method seeks to find the flow of phase differences that minimizes the total cost of the edges, subject to constraints such as continuity and smoothness. Let $\mathbb{S}$ be $m \times n$ rectangular grid of points (i,j) such that $0 \leq i \leq n-1$ and $0 \leq j \leq m-1$. If $\varphi(i,j)$ is the unwrapped phase corresponding to the wrapped phase $\Phi(i,j)$, based on Equation 2.23 we get $\varphi(i,j) = \Phi(i,j) + 2\pi k(i,j)$ for $(i,j) \in \mathbb{S}$. Equivalently, it can also be restated as finding discrete derivative residuals in the azimuth ξ_x and range ξ_y direction [80]:

$$\begin{aligned} \xi_x(i,j) &= \frac{1}{2\pi}\left[\Delta_x\varphi(i,j) - \Delta_x\Phi(i,j)\right], \\ \xi_y(i,j) &= \frac{1}{2\pi}\left[\Delta_y\varphi(i,j) - \Delta_y\Phi(i,j)\right], \end{aligned} \tag{2.27}$$

The discrete partial derivatives can then be derived from the residuals and used to reconstruct unwrapped phases [80]. Residuals ξ_x and ξ_y are determined as solution of the following minimization problem [80]:

$$\underset{\xi_x,\xi_y}{\operatorname{argmin}} \left\{ \sum_{i=0}^{m-2} \sum_{j=0}^{n-1} \omega_x(i,j) \left| \xi_x(i,j) \right| + \sum_{i=0}^{m-1} \sum_{j=0}^{n-2} \omega_y(i,j) \left| \xi_y(i,j) \right| \right\} \tag{2.28}$$

subject to the constraints

$$\begin{aligned} \xi_x(i+1,j) - \xi_x(i,j) + \xi_y(i,j) - \xi_y(i,j+1) = \\ \frac{1}{2\pi}\left[\Phi_x(i,j) - \Phi_x(i+1,j) + \Phi_y(i,j+1) - \Phi_y(i,j)\right] \\ \xi_x(i,j) \in \mathbb{Z} \\ \xi_y(i,j) \in \mathbb{Z} \end{aligned} \tag{2.29}$$

where ω_x, ω_y stands for the weights and correspondingly indicates the reliability of estimated integers. The constraint in Equation 2.29 ensures that the difference between unwrapped phase and wrapped phase gradients is an integer number of cycles. This leads to formulating the phase unwrapping problem as a global minimization problem with integer variables: the weighted deviation between the estimated and the unknown discrete derivative of the unwrapped phase is minimized, subject to the constraint that the two functions must differ by integer multiples of 2π [80].

In the time domain, a model is used to describe the time evolution of the phases. Parameters of the model are usually values obtained from the solution space that minimizes a cost function defined based on the differences between modeled and observed phases [79]. The order of the PhU in space and time can be done either way with the pros and cons of each of the approaches. Extending from two dimensions to three, decreases the chance of disconnected regions and provides more information on positions of phase discontinuities as residues [30], which are isolated points in two dimensions, are closed loops in three dimensions [89]. As a consequence, the MCF algorithm is developed further to the spatiotemporal contexts for multi-look and/or full-resolution interferograms [30], [32], [76], [79], [90] in the framework of SBAS methodologies. The result of spatiotemporal unwrapping is the unwrapped time-series per selected pixel with respect to a reference point in space. As a consequence, the final results of MT-InSAR are always relative to the chosen reference. For absolute interpretation, the deformation time-series have to be connected to an external datum [91]. Generally, the MCF method has advantages over others as it is computationally efficient, and can handle large datasets. It is also robust to noise and outliers in the data.

2.3.4 Atmospheric component estimation

The spatial and temporal variations of atmospheric changes mainly cause tropospheric delays that considerably affect the accuracy of InSAR-derived surface displacements [92], [93]. Atmospheric artifacts in repeat-pass SAR interferograms are changes in the refractive index of the medium primarily caused by the atmospheric pressure, temperature and water vapor [94]. The tropospheric delay has the form [95]:

$$\Delta L = 10^{-6} \int_{z_0}^{\infty} N dz \approx 10^{-6} M_e \left[\frac{k_1 R_d}{g_m} p(z_0) + \int_{z_0}^{\infty} (k_2 \frac{e}{T} + k_3 \frac{e}{T^2})\, dz \right] \tag{2.30}$$

where ΔL is the tropospheric delay along the satellite-Earth path in meters,N is the refractive index, $P(z_0)$ is the surface pressure in pascals at altitude z_0, g_m is the gravitational acceleration averaged over the troposphere in m/s, e is the water vapor pressure in pascals, T is the temperature in kelvin, and M_e is the mapping function that projects the ZTD to slant total delays based on the satellite elevation angle. The remaining terms are constants: $R_d = 287.05\ J\ kg^{-1}\ K^{-1}$, $k_1 = 0.776KPa^{-1}$, $k_2 = 0.233KPa^{-1}$, and $k_3 = 3.75 \times 10^3 K^2 Pa^{-1}$. The interferometric phase change $\Delta\Phi$ of a repeat-pass SAR interferometry can be written as [96]:

$$\Delta\Phi = \Phi_1 - \Phi_2 = \frac{4\pi}{\lambda}\left[(r_1 - r_2) + (\Delta L_1 - \Delta L_2)\right] \tag{2.31}$$

where ΔL_1 and ΔL_2 are atmospheric propagation delays of radar signals in the LOS direction, λ is the wavelength of the signal, and r_1 and r_2 are the slant range vectors corresponding to the first and second acquisitions, respectively.

Generally, to estimate and filter out atmospheric artifacts also called atmospheric phase screen (APS), either a model-based or a data-driven approaches are employed. Datasets such as GPS/GNSS observations [92], [97], numerical weather models [98] and the Generic Atmospheric Correction Online Service (GACOS) [99]–[101] are among the external sources of information for mitigating atmospheric effects. Using such external data sources generally helps to reduce 20-40% of the atmospheric effects [94]. But, still— the high spatio-temporal dynamics of water vapor in the lower troposphere usually make it difficult to remove APS from InSAR measurements [102]. Besides, biases and stochastic components still make the atmospheric signal delay component difficult to be modeled. Issues of weather dependency and spatial density of measurements from external sources also brought the necessity of alternative techniques. One of which is estimating APS from InSAR measurements by utilizing the difference in temporal characteristics between APS and ground deformation. The former is assumed to have high variability, whereas the latter very often shows a strong temporal correlation [102]. As a result of which a low-pass filter is used to remove signals associated with APS. Apart from their degree of success, it is also worth noting that external atmospheric correction methods have their inherent limitations— and hence no single method can be applied at all times, and anywhere [100]. Overall, the choice of the appropriate mitigation strategy should be considered based on the number of available SAR scenes, the method used for the processing, the atmospheric conditions and the availability of external data [94]. Detail discussions on the various error sources and mitigation strategies are discussed in [92], [103].

2.4 Geocoding

As MT-InSAR outputs are in a coordinate system related to SAR geometry, presentation of final products in the universal cartographic grid is required to ease the interpretability of results. Geocoding is the procedure responsible for a coordinate transformation from a radar datum to an earth-fixed geodetic datum. A rigorous geocoding, furthermore, requires knowledge of the sensor model describing how the image and object spaces are connected [68]. Often, it is carried out by iterative solving the Doppler-Range-Ellipsoid equations [1], [49].

Let $\vec{\mathbf{T}}(X, Y, Z)$ be the position vector of the target point in the plane orthogonal to the sensor orbit- also called zero-doppler plane.

$$\dot{\vec{\mathbf{S}}}_i(t_i).(\vec{\mathbf{S}}_i(t_i) - \vec{\mathbf{T}}) = 0, \tag{2.32}$$

$$||\dot{\vec{\mathbf{S}}}_i(t_i) - \vec{\mathbf{T}})|| - r_i = 0, \tag{2.33}$$

where $\vec{\mathbf{S}}_i$ and $\dot{\vec{\mathbf{S}}}_i$ are the i^{th} master image antenna state vectors and its velocity vector, respectively. Their values can be tracked from the orbital data. r defines sensor to target slant range and obtained by multiplying the speed of light c with the signal travel time in the range t_{rg} as $\frac{c.t_{rg}}{2}$. Equation 2.32 states the target point lies in the zero-Doppler plane at time t and Equation 2.32 refers to the range equation of the image point. That means the geometric distance between $\vec{\mathbf{T}}$ and $\vec{\mathbf{S}}_i$ should be equal to t_{rg} multiplied by the speed of light in vacuum c divided by two. However, to determine the coordinates of a pixel (X, Y, Z), additional height profile information needs to be considered from the co-master antenna $\vec{\mathbf{S}}_j$. That is, Equation 2.32 and Equation 2.33 are re-evaluated for co-master antenna. The slant ranges of the antennas are then related the following way [49]:

$$r_j = r_i + \frac{\lambda\varphi}{4\pi} \tag{2.34}$$

Assuming the unwrapped interferometric phase φ has been already evaluated, at this stage, we obtain a system of four equations in the four unknowns X, Y, Z and t_j. This system of equations is usually solved by iteration, starting from the initial guessed values of the unknowns [49]. Finally, these coordinates are converted to the geographic coordinates (Φ, Λ, H) or to the UTM map projection (E, N, H) where Φ and Λ are the geographic latitude and longitude while E and N denote the UTM Easting and Northing and H representing the height above the reference ellipsoid. Details on geocoding are discussed in [35], [49].

2.5 Conclusions

This chapter has reviewed the basic principles of MT-InSAR processing and analysis fundamentals and the advancements made in recent years along with associated challenges. It has been witnessed that MT-InSAR is a powerful technique that revolutionized remote sensing data collection and analysis techniques— primarily in monitoring surface deformation induced by either natural or anthropogenic activities over large areas and long time periods. The technique involves processing large amounts of SAR data and generating interferograms, which are then used to estimate the ground deformation. Despite its numerous advantages, MT-InSAR has also been found to be error-prone like any other remote sensing technique. Commonly due to the complexity of the input data (affected by atmospheric effects arising from the uncontrolled medium of signal propagation, and from the changes in the scattering properties of the ground surface resulting from the land cover changes over time), instrument errors and data processing errors. The latter one, which includes phase unwrapping errors has the potential to significantly impact the accuracy, reliability, and interpretation of MT-InSAR products and thus has been the main emphasis of the chapter and put in place accordingly.

CHAPTER 3

MT-INSAR DATA PROCESSING CHAIN AND QUALITY METRICS

3.1 Introduction

As a well-established geodetic technique for Earth surface deformation monitoring, the accuracy of InSAR time-series products should be well quantified and the potential error sources must be addressed. Any uncertainty in the accuracy of the InSAR products compromises their reliability in sensitive applications [104]. The accuracy of the deformation estimates is governed by the quality and number of exploited images, associated interferograms and selected measurement points. Moreover, incomplete representations of factors affecting deformation measurements may lead to omission errors and hence an incorrect estimation and interpretation of deformation time series. In this regard, quality metrics quantifying involved parameters and their impact play a huge role in the detection and rejection of outliers leading to such problems [40]. Ensuring the quality of interferometric SAR data helps in assuring how well the data is suited to the specific purpose they are supposed to serve. This chapter devotes to exploring main interferometric phase error sources, a brief discussion on the PSIG chain addressing common InSAR errors, TS phase inversion, and temporal phase consistency issues followed by the formulation of new MT-InSAR data quality metrics. Different sources of noise that compromise InSAR analysis are also presented.

3.2 Phase bias sources in small baseline MT-InSAR data

Interferometric phase noise sources are mainly attributed to geometric, temporal and/or Doppler centroid decorrelation [1], [105]. Geometric decorrelation is caused by the different incidence angles of the two SAR acquisitions forming an interferogram. It generates a shift in the range spectra of the two SAR images that increases with the perpendicular baseline. Temporal decorrelation, on the other hand, occurs when the electrical characteristics of scatterers within a resolution cell change along time. Seasonal and anthropogenic changes overtime produce high variablity on physical properties of scatterers that in fact lead to a temporal decorrelation in interferograms with large temporal baselines. The Doppler centroid decorrelation is another factor caused by differences in the Doppler centroid frequencies between two acquisitions. Band-pass filter strategies are typically applied in order to reduce such impacts. Phase errors are also attributed to SAR images co-registration misfit that can introduce artificial phase ramps which will of course affect the reliability of final InSAR products [106]. Other sources of noise also include the thermal noise [107] of the system and errors associated with PhU. The latter one is of main concern and will be addressed in section 3.4.2.

3.2.1 Phase Inconsistency

The inverted phase time-series, discussed in Section 3.4.1, can be potentially biased by wrong integer numbers of cycles added to the interferometric phase during the two-dimensional phase unwrapping [39]. An interferometric phase is said to be inconsistent if the closure phase is nonzero. Unlike the case of deterministic radar targets, the property of phase consistency fails to hold for DSs [19]. In exploitation of DSs, the closure phase of the averaged interferometric phases during multilooking, often are nonzero [19] and are generally associated with phase inconsistencies [108], [109]. This is due to variations in the scattering and electrical properties of the ground surface [110]. This actually arose the demand to phase consistency check as potential tool in addressing unmodeled phase errors and in reducing their impacts on InSAR timeseries products in the area of deformation monitoring, for instance [110]. Unwrapping errors could break the consistency of interferometric phases in the time domain [111]. The closure phase on this regard is considered as the cyclic product of the unwrapped interferometric phases [39], [112]:

$$\bar{\psi}_{ijk} = \Delta\psi_{ij} + \Delta\psi_{jk} + \Delta\psi_{ki} \tag{3.1}$$

where $\Delta\psi_{ij}$, $\Delta\psi_{jk}$ and $\Delta\psi_{ki}$ are unwrapped interferometric phase triplets generated from the SAR acquisitions at t_i, t_j and t_k. The integer ambiguity of the closure phase is as well given by:

$$\bar{\upsilon}_{ijk} = \frac{1}{2\pi}(\bar{\psi}_{ijk} - \bar{\psi}_{ijk} \mod 2\pi) \tag{3.2}$$

For a redundant network of interferograms, the temporal consistency of the integer ambiguities of unwrapped interferometric phases can also be expressed as [39]:

$$\bar{\upsilon}\Upsilon + (\bar{\upsilon}\Delta\Phi - \bar{\upsilon}\Delta\Phi \mod 2\pi)/2\pi = 0 \tag{3.3}$$

where $\bar{\upsilon}$ is a $p \times q$ design matrix of all possible interferogram triplets, Υ is an $p \times 1$ vector of integer numbers of cycles required to meet the consistency of the interferometric phases. A further note on phase inconsistencies is available in [39], [104], [112].

3.3 Small baseline MT-InSAR data processing flow

The SB multitemporal interferometric method generally deals with the estimation of terrain displacement evolution. Other phase contributions that are not of interest are often mitigated with pre- or intermediate processing. The Persistent Scatterer Interferometry chain at the Remote Sensing Department of the Geomatics research unit of the CTTC—PSIG processing chain, is composed of flexible processing blocks that can be adapted based on the datasets, case area and purposes. This enhanced the technique to accommodate, for instance, various pixel selection strategies into the processing chain including those amplitude and coherence-based techniques. This section, in particular, details the Sentinel-1 data processing flow in the framework of PSIG procedure for small baseline interferograms. Basically, the processing chain involves the generation of interferograms from complex SLC SAR images, unwrapping phases of selected points of a network of interferograms, estimating APS components using spatio-temporal filters and removing from interferometric phases obtained from earlier steps and finally computing timeseries of displacements estimation followed by geocoding (Figure 3.1). Main processing steps are briefly outlined below.

1 **Coregistration**. At this step, the azimuth shift of each image with respect to a common master image is retrieved. For TOPS data, the nature of the burst-mode acquisition and the azimuth antenna steering are among the causes that have brought the need to employ azimuth coregistration. The procedure guarantees a pixel from different images to correspond to the same footprint on the ground. For its effective implementation, one approach is to choose one image as geometric reference for the co-registration of all other images. This is also accompanied by resampling of the images onto the grid of the reference one to ensure pixel-to-pixel alignment along the entire image stack. The precise coregistration leads to more accurate phase estimation, increases the coherence of the interferogram and improves the quality of the phase unwrapping [113]. A

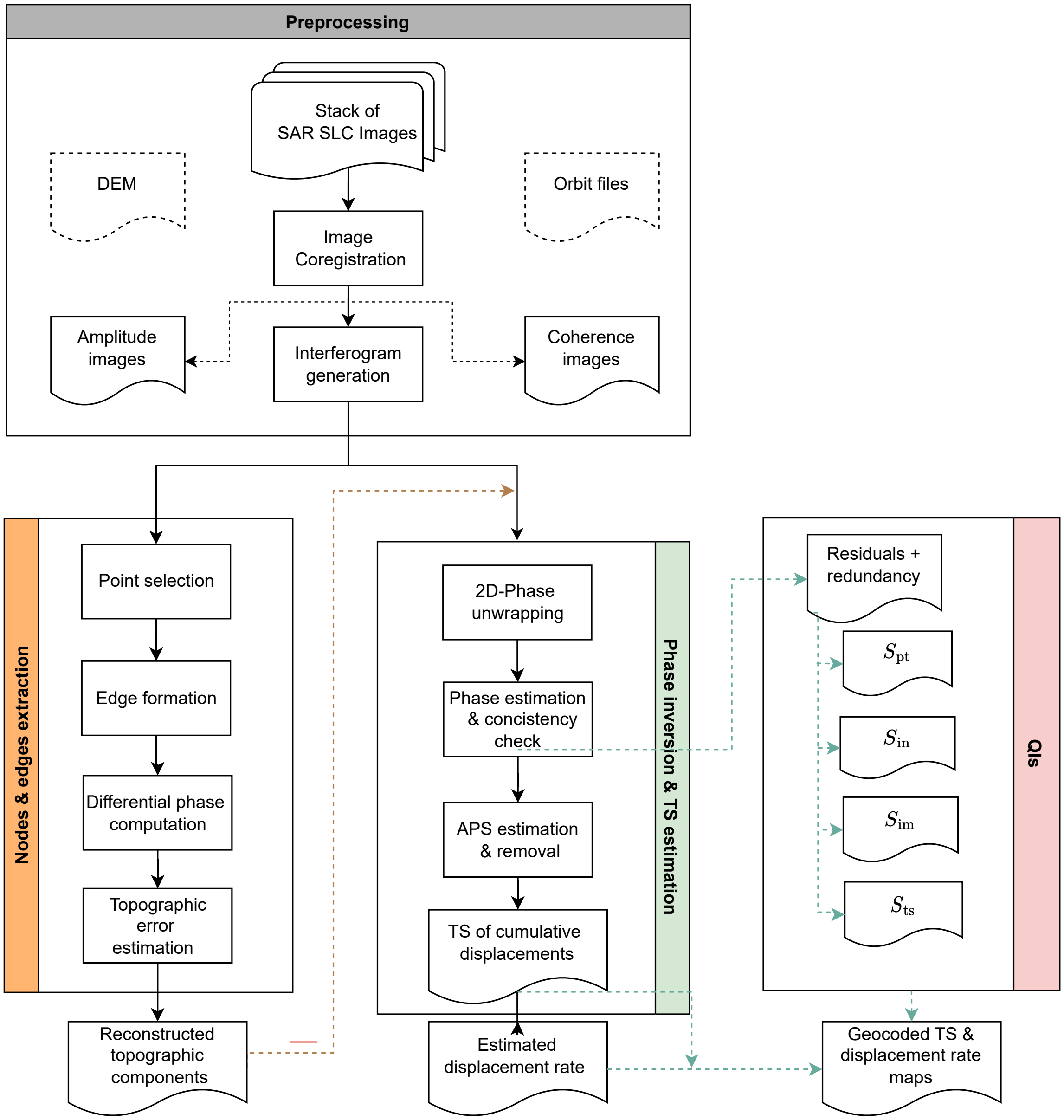

Figure 3.1: MT-InSAR processing workflow, in this context, nodes and edges respectively refer to the selected points and the corresponding edges connecting the points in the spatial domain. The DEM and orbit files used in the pre-processing are also required at the geocoding step. The QIs block incorporates newly introduced main tools from the existing PSIG chain. On the right side, inside the QIs block the notations $S_{\mathrm{pt}}, S_{\mathrm{in}}, S_{\mathrm{im}}$ and S_{ts} respectively denote the scores associated to the measurement points, the interferograms, images and the TS that are derived from residues and redundancy information.

better coregistration for Sentinel-1 data processing facilitates the merging of sub-swaths and/or bursts and minimizes associated effects if otherwise. Detail information on the coregistration of SAR images, in general, is available in [113]–[116].

2 **Interferogram generation**. As described in Section 2.2.1.3, interferograms represent sets of phase differences derived from a pair of coregistered SAR SLC images as per the Equation 2.6. These are interferometric data used as main sources of information in the study of TS of ground displacement evolution. The number of interferograms generated from the image stack depends on the objective to achieve and the type of processing approach to employ. The interferogram network could be generated using several image-pairs combinations as described in section 2.3.2. In this thesis, due to the necessity of redundancies in determining quality scores, SB-based redundant interferogram network configurations have been used. In addition to the small spatial and temporal baseline constraints, the interferogram selection method adopts spatial coherence criteria and minimum image redundancy criteria. From interferograms passing SB constraints, we further exclude those with average spatial coherence lower than a predefined threshold. In addition, interferograms can also be excluded due to the redundancy threshold set on images.

3 **Point extraction**. Following the interferogram selection, points with significant decorrelation effects would be discarded to keep (relatively) quality PSs in the upcoming process. The point extraction step is at the center of every interferometric data processing chain with significant power in influencing the qualities of final products. Techniques employed to extract such PSs are mostly threshold based — the criteria of dispersion of amplitude [12] and the spatial coherence criteria [67], as described in section 2.3.1, being the dominant one. The choice of thresholds involve finding a trade-off between measurement point density and the quality of associated phases. An empirical way to prove the goodness of the chosen threshold is analyzing the quality of phase unwrapping results as it often depends on both the pixel density and phase quality [68].

Pixel extraction based on phase amplitude—estimates the phase standard deviation of every pixel from the associated temporal amplitude stability. It preserves the spatial resolution of the images and allows the detection of isolated scatterers smaller than a resolution cell [15]. On the other hand, spatial coherence is used to obtain the maximum likelihood estimator of the coherence magnitude [1] and provides an estimation of the accuracy of the pixel's phase for each interferogram independent of the number of images used, unlike the case of the amplitude dispersion index. However, the required estimation window affects the spatial resolution and can cause the loss of scatterers that could be detected with the amplitude criteria. Min-coherence criteria [15] is also an option to select PSs of multilooked images. PSs with a mean coherence, as calculated from a stack of coherence maps, over a selection threshold value are accepted as candidates. Not only these, the index defined in Equation 3.4 [32], is also another criterion well integrated into the PSIG chain to select candidate PSs. Its effectiveness on phase noise reduction and better coverage of measurement PSs makes it an easier choice among PSs selection techniques considered in this thesis. It is implemented by first computing the spatial low-pass interferometric phase $\Delta\varphi_k^{LP}(p)$ using a boxcar averaging window. The resulting phase is then subtracted modulo 2π from the original interferometric phase $\Delta\varphi_k^{LP}(p)$, giving a high-pass estimate of the interferometric phase. For each pixel, the high-pass complex phase vectors are then averaged coherently to mitigate the effect of the phase noise—and the resulting metric is computed by taking the modulus of the resultant vector as:

$$\Omega\left(\mathfrak{p}\right) = \frac{1}{\ell}\left|\sum_{k=1}^{\ell} e^{j(\Delta\varphi_k(p)-\Delta\varphi_k^{LP}(p)}\right| \tag{3.4}$$

where ℓ is the number of interferograms, and k is the interferogram index. The values of Ω range between 0 and 1 inclusive. The higher the value of Ω the more coherent the measurement point would be. For the purpose of convenience, here after, terms: pixel, PSs and DSs are used interchangeably.

4 **APS estimation and removal**. The APS estimation and removal is one of the main steps—done over the PS network of unwrapped phases using a set of spatio-temporal filters often by assuming high spatial and low temporal correlations in the APS signal. However, a failure of such assumptions leads to erroneous results commonly due to unfiltered local atmospheric phenomena or loss of deformation signal of a target. The APS signal can also be a source of phase unwrapping errors, especially when its spatial behavior has a turbulent nature. To deal with these, the PSIG chain in particular, exploits the low-pass Butterworth filter (Equation 3.5) in the frequency domain to remove the atmospheric contribution of the phases. Subsequently, a high-pass temporal filter (Equation 3.6) is also implemented to separate APS signal from temporally correlated components— usually associated with terrain deformations.

(a) Low-pass spatial filter is a filter performed in the spatial frequency domain the following way.

$$H_{LP_s}(u,v) = \frac{1}{1 + \left[\frac{u^2+v^2}{d_c^2}\right]^n} \tag{3.5}$$

where dc is the spatial cutoff frequency and n is the filter order. Lower values of dc yield a more selective filter, rejecting a larger portion of the image spectrum. On the other hand, lower values of the filter order yield a smoother filtering function. The spatial low-pass filter is followed by a temporal high pass filter to separate these deformation phases from the APS. That is, the signal correlated in time is estimated and removed from the candidate APS with this filter.

(b) High-pass temporal filter. This filter is applied on the LP_s component. The APS estimate is obtained from the temporal high-pass component which is achieved by computing the residual of its temporal low-pass component. The frequency response of the one-dimension low-pass Butterworth filter is given by [117]:

$$H_{LP_t}(f) = 1/\sqrt{1 + \left(f * f_c^{-1}\right)^{2m}} \tag{3.6}$$

where f_c is the temporal cutoff frequency and m is the temporal filter order.

The cutoff frequency selection is a key step of the APS estimation— those frequencies that are lower than this value will be associated with the atmosphere. The estimated APS phase component is finally removed from the original differential interferograms to get APS free interferograms. Of course, discriminating between the part of the signal that is APS from that of the deformation signal is often not straightforward.

5 **Estimation of the residual topographic error**. As the DEM used to mitigate the topography is not always perfect, the phase component associated with the height error is estimated at this step. In addition to external DEMs, orbital information of the satellite at time of acquisition of images pair are used to extract topographic contributions. For this, differences in the wrapped phase difference are calculated for each edge, which is formed by connecting selected points pairwise from each interferogram spatially. Edges are made as short as possible to minimize the atmospheric effects. Besides, the number of edges connected to a node which in principle represents an image is also limited to a threshold value that influences the quality and processing time. The differential residual topographic errors are computed using the method of periodogram [118]. These differential values are then integrated over the whole set of edges using an iterative least-square procedure by considering the initial value from a predefined reference PS. Contributions of estimated residual topographic errors are then subtracted from the original interferometric phase to give a relatively clean interferometric phase to be used in the subsequent processing steps [119]. For a differential wrapped phase $\Delta\Phi_i^k$ at edge i in the k^{th} interferogram, the goal is to get the unknowns $\Delta\mathcal{H}_e$, that mini-

mize the residual phase component given by:

$$\Delta\varepsilon_i^k = \Delta\Phi_i^k - (\frac{4\pi}{\lambda}\frac{B_\perp^k}{R^k \sin\theta^k}\Delta h_e^i) \mod 2\pi \tag{3.7}$$

where Δh_e^i is the residual topographic error at edge i, ${B^k}_\perp$ is the perpendicular baseline of interferogram k. R^k and θ^k are mean slant range and mean slant angle of interferogram k and λ is the radar wavelength. The best estimate of residuals in Equation 3.7 is achieved by maximizing the following function at edge i, given by Γ_i.

$$\Gamma_i = \frac{1}{\ell}\sum_{k=1}^{\ell} e^{j(\Delta\varepsilon_i^k)} \tag{3.8}$$

where ℓ stands for the number of processed interferograms. The function Γ in Equation 3.8 takes values between 0 and 1, reaching its maximum when the residual errors are zero. The estimation process is repeated over selected edges satisfying the maximum distance criterion. PSs that are redundantly connected with a Γ value above a threshold, adjusted depending on the area of interest, are then selected. Among many other benefits, this operation is required in order to ensure correct unwrapping over the dense network of points [118]. Equation 3.7 is a special case of the models described in [107], [119] with no prior assumptions on the linearity of deformation parameters. It is beneficial to analyze deformation phenomena that are non-linear in time such as the displacements associated with mining activities [118]. It is also worth mentioning that the extended version of the model with three parameters involving velocity and thermal components is elaborated in [107].

6 **Space-time phase retrieval** This section presents one of the fundamental phase estimation steps used in the PSIG processing chain. The 2D PhU technique which is error-prone mainly due to isolated pixels and the influence of high phase gradients, atmospheric artifacts, and noise will be discussed. Following which, a 1D temporal phase

estimation technique aiming at the detection and correction of the errors generated in the 2D PhU stage is presented. For such purposes, an iterative LS procedure [120], [121], that fully exploits the integer nature of the unwrapping errors was used.

A spatial 2D phase unwrapping is performed on each interferogram using the MCF method [37], [80] as elaborated in Section 2.3.3.3. The technique is considered as the weighted ℓ_1-norm minimization problem of the deviation between the estimated and unknown phase gradients. Sample maps are shown in Figure 3.2 to provide visual information on wrapped and unwrapped phases. Technically, the interferometric phase $\Delta\Phi_{x_j}^{t_{\alpha\beta}}$ of two SAR images at times t_α and t_β at pixel x_j is measured modulo 2π. However, if the surface displacement is greater than a quarter of the radar wavelength (≈ 1.4 cm as Sentinel-1 satellites datasets are used in this dissertation) or due to the influence of other effects, like topographic errors, atmosphere, or noise interferograms— it might not be uniquely inverted. Moreover, considering the revisit time and wavelength of Sentinel-1 satellites, the maximum measurable differential deformation rate is 42.6 cm/yr [17]. In fact, the actual capability to estimate the displacement relies on the noise level of the data and the effectiveness of the PhU technique to resolve phase ambiguities [35].

Generally, the unwrapped phase is obtained by adding an integer multiple $k_{x_j}^{t_{\alpha\beta}}$ of 2π to the wrapped phase associated with each element of the set of selected pixels χ of each interferogram.

$$\Delta\varphi_{x_j}^{t_{\alpha\beta}} = \Delta\Phi_{x_j}^{t_{\alpha\beta}} + 2\pi k^{t_{\alpha\beta}} \quad \forall x_j \in \chi \tag{3.9}$$

The procedure starts with the measured wrapped phases and considers the unwrapped phase as a continuous curve and thus as an integral of the phase gradients [122]. The formulation in Equation 3.9, prevents errors and their effect from spreading in the network [123]. The wrapped measured phase gradients between two adjacent pixels x_k and x_l result in:

$$\Delta\Phi_{x_{kl}}^{t_{\alpha\beta}} = (\Phi_{x_k}^{t_{\alpha\beta}} - \Phi_{x_l}^{t_{\alpha\beta}}) \mod 2\pi \quad \forall x_{kl} \in \chi \tag{3.10}$$

For sufficiently sampled measurements, assuming the change in the unwrapped phase between adjacent pixels is less than half a cycle, the unwrapped phase $\varphi_{x_{kl}}^{t_{\alpha\beta}}$ at pixel x_j can be easily reconstructed up to an additive constant by integrating the wrapped phase gradients along any set of phase gradients that connects a reference point x_0 and the pixel x_j [124].

$$\Delta\varphi_{x_j}^{t_{\alpha\beta}} = \sum_{\forall x_{kl} \in \mathcal{N}_{x_j}} \Phi_{x_{kl}}^{t_{\alpha\beta}} + \varphi_{x_0}^{t_{\alpha\beta}} \tag{3.11}$$

In practice, the oriented sum of phase gradients in a loop is sometimes non-zero—referred to as a residue. Such inconsistencies mainly arise because of phase noise, and atmospheric or topographic effects that should be corrected/avoided a priori [124]. In processing MT-InSAR stack, as several interferograms are considered — assessing their temporal relationship might enhance the accuracy and interpretation of the final solution [30].

In the temporal domain—the main goal of the phase estimation is detecting and, if possible, correcting the errors generated in the 2D phase unwrapping stage. This operation, which makes use of an iterative procedure based on the SVD least squares method [16, 17], fully exploits the integer nature of the unwrapping errors as well. In the case that the errors can not be corrected, they are rejected from the original set of observations [125]. Temporal phase estimators allow the retrieval of a time series of consistent interferograms from all possible inconsistent interferograms within a SAR time series. In doing so, they effectively reduce the stochastic phase noise. Exploiting the temporal data redundancy, is expected to be less susceptible to systematic inconsistencies as well [112].

7 **Geocoding**. Up till now, interferometric measurement points are in the radar geometry. Each pixel in the range of a SAR system carries the time tag corresponding to the two-way time delay of the transmitted and reflected pulses. However, ionospheric and tropospheric variations of the refraction index of SAR signals lead to time delays of

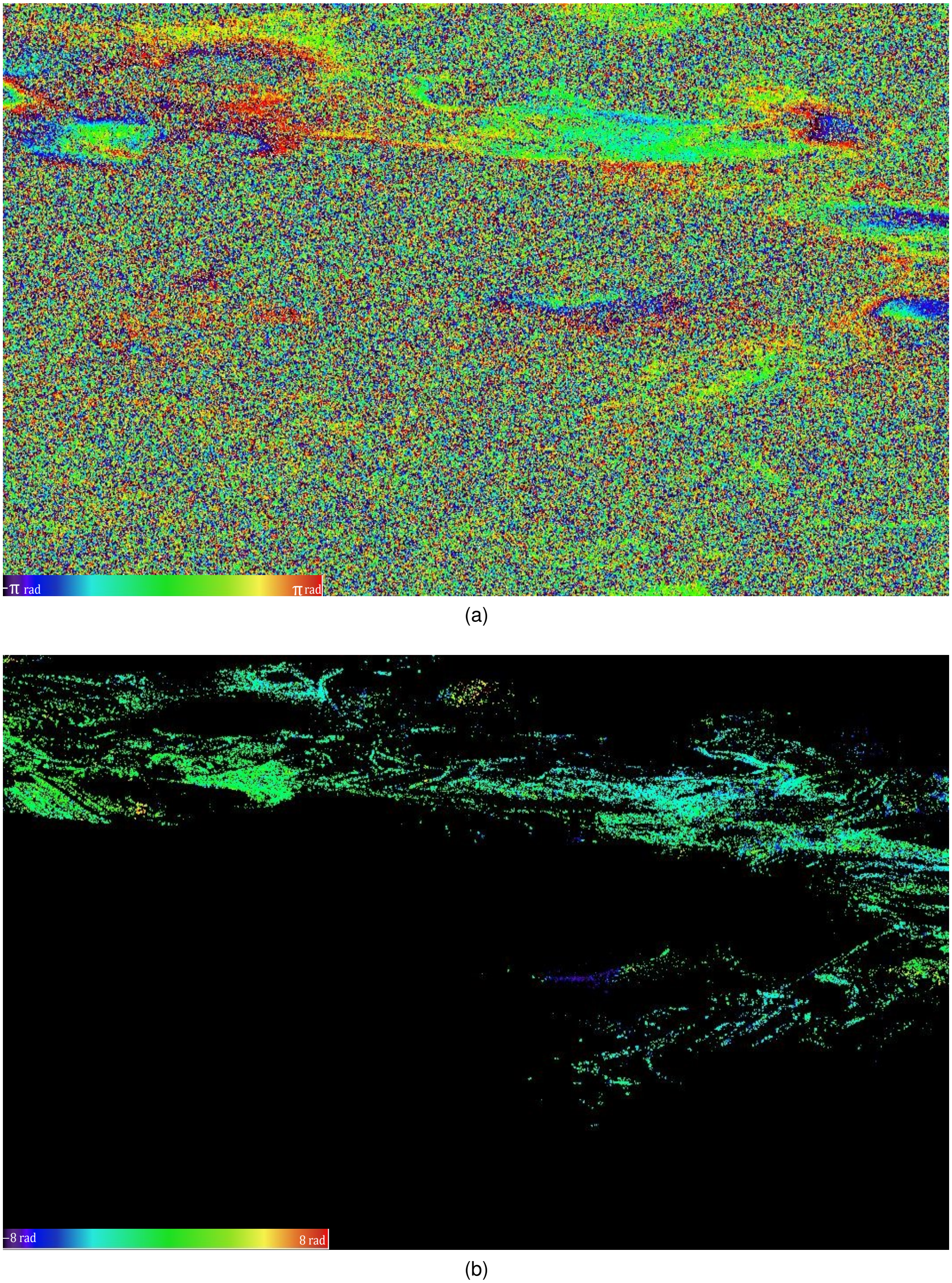

(a)

(b)

Figure 3.2: Example of spatial phase unwrapping of an interferogram from the Brumadinho mining area, Brazil. Map of wrapped phases in (a) and corresponding map of unwrapped phases of selected points in (b).

return signals [57] and sometimes results in errors in azimuth and range time estimates that also impacts PS measurement height [126]. Furthermore, the height of a PS is estimated with respect to a reference point— whose final height is taken as the DEM height. In a broader sense, the geocoding procedure allows estimating the geographical or cartographic coordinates of target points making use of the associated DEM information, azimuth and range coordinates of the PS, orbits of the reference image, and the residual topographic error. This is a key step to enable the interpretation and exploitation of interferometric products. Section 2.4 elaborates on a brief description of the geocoding principles implemented in this dissertation.

As a complex and sensitive technique that involves a series of processing steps, many factors can still affect the quality of the final results of MT-InSAR. In this regard, the PhU error appears in the forefront leading to erroneous results. Section 3.4 highlighted how the problem is approached and lays the foundations for the formulation of QIs discussed in Section 3.5.

3.4 Phase reconstruction and measurement reliability

Phase reconstruction in InSAR involves recovering the phase differences between two or more radar signals acquired at different times. Inaccuracies in the measurement of the phase difference can lead to errors in the estimated surface deformation. Phase reconstruction and measurement reliability are both critical concepts in InSAR. Accurate phase reconstruction is necessary to estimate surface deformation, while measurement reliability is necessary to ensure the accuracy of these estimates. The emphasis of this section is to discuss the deformation signal retrieval procedures and to highlight steps followed to check the consistency of recovered phases. The two important parameters used in section 3.5: the residue and redundancy parameters are also the focus of the discussion.

3.4.1 Deformation signal retrieval

In MT-InSAR time series algorithms, the deformation phase represents the primary signal of interest and is modeled by incorporating SAR phase contributions from the source to the target as elaborated in Equation 2.16. The main idea is to separate interferometric signals contributed by ground deformation from stacked interferograms by taking advantage of spatial and temporal characteristics of phase components [127]. Fundamentally, for each pixel— the phase value of each SAR image is exploited from the stack of unwrapped differential interferometric phases. The phase of a pixel, $p(x,y)$ in the azimuth and range coordinates (x,y) of the k^{th} interferogram derived from SAR images acquisitions from time t_α to t_β, is given by:

$$\begin{gathered}\varphi_{k_p}^{t_{\alpha\beta}}(x,y) = \Phi_{k_p}(x,y,t_\beta) - \Phi_{k_p}(x,y,t_\alpha) \\ \forall k = 1,\dots,\ell \quad \text{and} \quad \forall p \in \chi\end{gathered} \tag{3.12}$$

where χ and ℓ respectively denote the set of selected points and the number of interferograms. Equation 3.12 implicitly incorporates the integer phase ambiguity due to the wrapped nature of phase measurements and the decorrelation effects resulting from other noise sources, such as the change in the scattering properties of the target pixel. Note also that the inversion is carried out on a pixel-by-pixel basis on all selected coherent pixels χ. Below, a commonly implemented procedure to retrieve unknown parameters from a given stack of observations is briefly addressed.

Suppose ℓ interferograms are generated from N SAR images acquired in an ordered time sequence $\{t_i\}_{i=0}^{n-1}$ based on the multi-master SB principle. Let $\hat{\varphi}$ be the vector of ℓ known unwrapped phases computed from the chronologically ordered master and co-master images. If $\hat{\Phi}$ stands for the vector of N unknown phase parameters with respect to time t_0, its values can be estimated from the system of equations [13]:

$$\boldsymbol{H\hat{\Phi}} = \boldsymbol{\hat{\varphi}} \tag{3.13}$$

where $\mathbf{H}$ stands for the incidence matrix. Assuming $u^T = [u_1, u_2, \ldots, u_\ell]$ and $v^T = [v_1, v_2, \ldots, v_\ell]$ are acquisition time-index vectors respectively associated with the master and co-master image pairs used in the interferogram generation, the j^{th} unwrapped interferogram could be described as:

$$\varphi_j = \Phi\left(t_{v_j}\right) - \Phi\left(t_{u_j}\right), \forall j \in [1, \ell] \tag{3.14}$$

For instance, if the first differential interferogram is formed by the first master and the third co-master images, the associated differential interferogram would be $\varphi_1 = \Phi(t_2) - \Phi(t_0)$ and similarly if $\varphi_2 = \Phi(t_3) - \Phi(t_1)$, the first two rows of the incidence matrix is formulated as in $\mathbf{H}$ in the system below:

$$\underbrace{\begin{bmatrix} 0 & 1 & 0 & 0 & \ldots & 0 & 0 \\ -1 & 0 & 1 & 0 & \ldots & 0 & 0 \\ \vdots & \vdots & \vdots & \vdots & \vdots & \vdots & \vdots \\ . & . & . & . & . & . & 1 \end{bmatrix}_{\ell\times(N-1)}}_{\mathbf{H}} \times \underbrace{\begin{bmatrix} \hat{\Phi}_1 \\ \hat{\Phi}_2 \\ \vdots \\ \hat{\Phi}_{N-1} \end{bmatrix}_{(N-1)\times 1}}_{\hat{\Phi}} = \underbrace{\begin{bmatrix} \hat{\varphi}_1 \\ \hat{\varphi}_2 \\ \vdots \\ \hat{\varphi}_\ell \end{bmatrix}_{\ell\times 1}}_{\hat{\varphi}} \tag{3.15}$$

In the construction of Equation 3.15, $\hat{\Phi}_i$ for $1 \leq i \leq N-1$, denotes the phases at different SAR acquisition dates t_i. Besides, the deformation at the first acquisition date, $\hat{\Phi}_0$ is considered negligible and hence constrained to be zero. It is also worth nothing to remind that entries and order of the coefficient incidence matrix $\mathbf{H}$ depends on the number and ways the SB interferograms generated from available images. When all the acquisitions belong to a single small baseline subset (SBAS) block, the incidence matrix $\mathbf{H}$ of Equation 3.13 becomes a column rank-full matrix. In which case, the deformation phases are estimated by using the LS approach. If $\mathcal{W}$ is the associated weight matrix, the deformation vector $\hat{\varphi}$ can be retrieved by solving Equation 3.16:

$$\hat{\mathbf{\Phi}} = \left(\mathbf{H^T}\mathscr{W}\mathbf{H}\right)^{\mathbf{-1}}\mathbf{H}^T\mathscr{W}\hat{\varphi} \tag{3.16}$$

If otherwise, differential interferograms belong to different blocks, $\mathbf{H}$ becomes rank deficient. This time, the SVD solution derived from the pseudo inverse of matrix $\mathbf{H}$ is used to estimate $\hat{\varphi}$ from Equation 3.17:

$$\hat{\mathbf{\Phi}} = \mathbf{V}S^{+}\mathbf{U^T}\hat{\varphi} \tag{3.17}$$

where $\mathbf{H}^{+} = \mathbf{VS^{+}U^{T}}$ is the pseudo inverse of matrix $\mathbf{H}$. U is an orthogonal $\ell \times \ell$ matrix whose first N columns are the eigenvectors of $\mathbf{HH}^T$; $\mathbf{V}$ is an orthogonal NxN matrix of columns that are the eigenvectors of $\mathbf{H}^T\mathbf{H}$, and $\mathbf{S}$ is ℓ matrix containing the non-zero singular values of $\mathbf{H}$. For σ_i, singular values of eigen values of $\mathbf{HH^T}$,

$$\mathbf{S}^{+} = \text{diag } \left(1/\sigma_1, 1/\sigma_2, ..., 1/\sigma_{m-n+1}, 0, ..., 0\right) \tag{3.18}$$

Accordingly, we get:

$$\hat{\Phi} = \sum_{i=1}^{m-n+1} \frac{\varphi^T u_i}{\sigma_i} v_i \tag{3.19}$$

where u_i and v_i are the column vectors of U and V, respectively. The solution of the system would be the one that minimizes the ℓ_2 norm of both residuals of the system in Equation 3.13 and that of the estimated phase vector $\hat{\varphi}$. However, such solutions may sometimes lead to large discontinuities [13]. Hence, to get a sound solution— mean phase velocity parameter between time-adjacent acquisitions are used to redefine the unknown cumulative phase values of Equation 3.13 [13], [28] as follows:

$$v^T = \left[v_1, v_2, ..., v_N\right] = \left[\frac{\hat{\Phi}_1}{t_1 - t_0}, \frac{\hat{\Phi}_2 - \hat{\Phi}_1}{t_2 - t_1}, ..., \frac{\hat{\Phi}_N - \hat{\Phi}_{N-1}}{t_N - t_{N-1}}\right] \tag{3.20}$$

The design matrix is also modified accordingly to represent the cumulative time between each interferogram pair. The values of $\hat{\Phi}$ are finally recovered by a simple integration [28].

More information on this and the SVD decomposition in general is available in [13], [128].

In fact, in this thesis— unique fully connected block of interferograms with redundant observations were used. The decision has been drawn from the fact that, disconnected network of interferograms with multiple subsets biases the time-series estimation [16] unlike the case of a fully connected network allowing unbiased phase inversion [39]. Improved orbital tube and a short revisit time of the Sentinel-1 dataset, have also simplified the task to get fully connected interferograms. The temporal coherence factor computed after the small baseline inversion of the stack of unwrapped phases defines the consistency between the original interferograms and those reconstructed from the displacement time-series [3].

3.4.2 Phase unwrapping consistency check

Often PhU errors can occur when the phase changes due to topographic error are large or when there are strong deformation gradients. Furthermore, a common source of unwrapping errors is given by phase variations due to the atmospheric component, particularly when the PS density is low, as in the case of isolated areas [44]. Besides, noise can result in unwrapping inconsistencies. The phase unwrapping errors have to be detected in order to avoid errors in the estimated phases, and, consequently, in the deformation estimates. A phase unwrapping consistency check is performed to determine if the unwrapping has been correctly performed over the selected candidate PSs. It is based on a temporal LS estimation and the analysis of the consistency between redundant observations. The PSs that satisfy this check constitutes the final network of PSs. As already mentioned, the check is based on a pixel-wise LS estimation and an analysis of the residues. The observation equation is given by:

$$\boldsymbol{\varphi}_{MS} = \boldsymbol{\varphi}_S - \boldsymbol{\varphi}_M \tag{3.21}$$

where φ_{MS} is the unwrapped interferometric phase (the observation), S and M are the comaster and master images and φ_S and φ_M are the corresponding unknown phases.

The LS solution of Equation 3.13 yields:

$$\hat{\boldsymbol{\Phi}} = (\boldsymbol{H}^T \mathcal{W} \boldsymbol{H})^{-1} \boldsymbol{H}^T \mathcal{W} \hat{\boldsymbol{\varphi}} \tag{3.22}$$

This also implies:

$$\hat{\boldsymbol{\xi}} = \boldsymbol{\varphi} - \hat{\boldsymbol{\varphi}} = \boldsymbol{H\Phi} - \boldsymbol{H}\hat{\boldsymbol{\Phi}} \tag{3.23}$$

where $\hat{\boldsymbol{\Phi}}$ is the vector of estimated unknowns, $\boldsymbol{\varphi}$ is the vector of the a posteriori estimated observations and $\hat{\boldsymbol{\xi}}$ is the vector of residuals. The phase estimation algorithm is accompanied by outlier correction/rejection criterion involving the following steps [44], [118]:

(i) LS estimation, computing the residuals.

(ii) Identification of all residuals above a fixed threshold and selection of the bigger one in absolute value (outlier candidate). The observation is considered as an outlier candidate when the corresponding residual is greater than the residual threshold.

(iii) Temporally removing the highest outlier candidate from the network and performing a new LS estimation.

(iv) Checking the residual of the outlier candidate: if it is a multiple of 2π (within a given tolerance), the observation is corrected and reaccepted. For unwrapping tolerance, $\mathcal{U}_0$ if an error lies within $2\mathcal{K}\pi \pm \mathcal{U}_0,\ \mathcal{K} \in \mathbb{Z}$ then it is considered as unwrapping error and will be corrected.

(v) Otherwise, the decision of re-entering or rejecting the outlier candidate is based on the comparison of its old and new residuals.

The procedure is executed iteratively for each observation. A temporal iterative LS is performed after the 2D phase unwrapping. The iterative LS method takes advantage of unwrapping error magnitude that is known a priori to identify unwrapping errors and correcting corresponding observations (see Figure 3.3). The interesting part is— it is also possible to visualize the distribution of residuals spatially to easily associate erroneous points with the case areas for better decision-making.

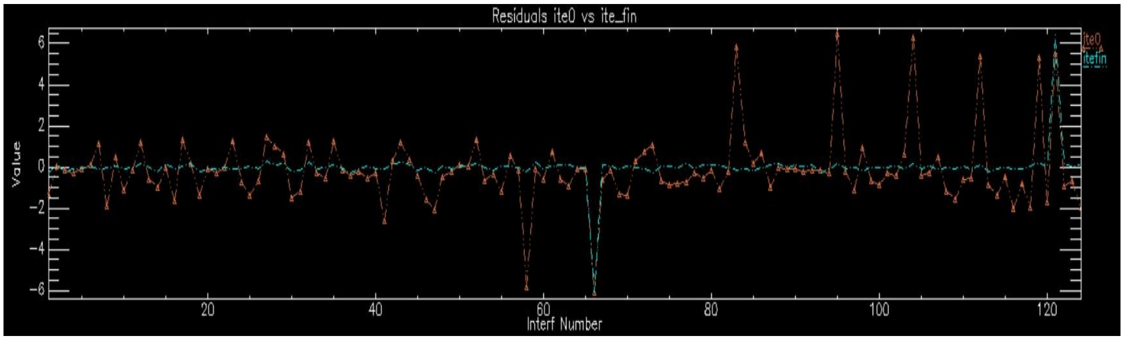

Figure 3.3: Plot of residuals at the first and final iterations of the phases TS estimation. The orange curve refers to the signal information at the first iteration and the cyan one is the signal at the final iteration for the same point. The phase values (in rad) are indicated on the vertical axis and the horizontal axis represents the indexes of images involved in the phase estimation. The improvements from the first to the final iteration are clearly visible apart from a few numbers of cases. The TS at the 66^{th} images, for instance, is the one where the outlier correction fails and justifies the importance of QIs.

Figure 3.4 shows the improvement of standard deviations of residuals from the first to the final iteration. Like the residue parameter, redundancy is a critical parameter that directly influences the correction, rejection or re-acceptance of outlier candidates in MT-InSAR data analysis.

3.4.2.1 Network redundancy parameters

The redundancy parameters refer to the number and distribution of overlapping SAR images used in generating a network of InSAR interferograms. A higher number of images and a more distributed network is assumed to improve the accuracy and reliability of deformation measurements by quantifying the number of overlapping measurements and the degree of agreement between them. Increasing the redundancy in a network of interferograms has been proven to improve the identification of reliable pixels— with five connections being a good balance among precision, reliability and spatial coverage [39].

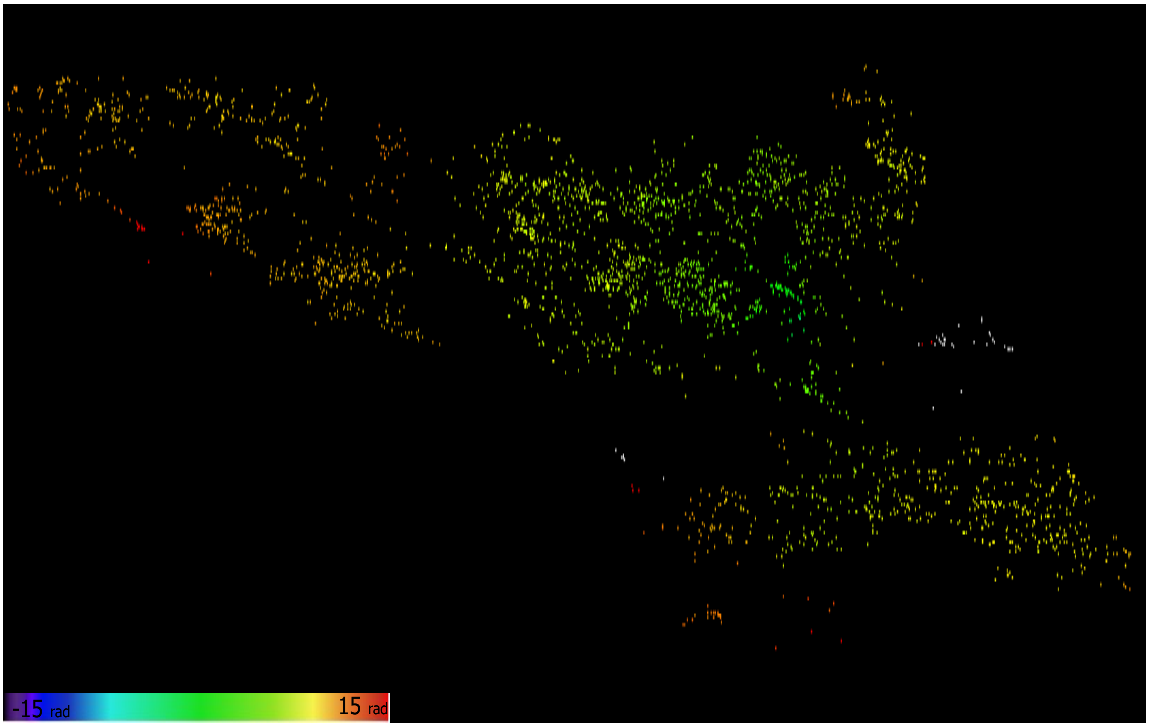

(a) Spatial distributions of standard deviations of residuals at the first iteration of the phase TS estimation.

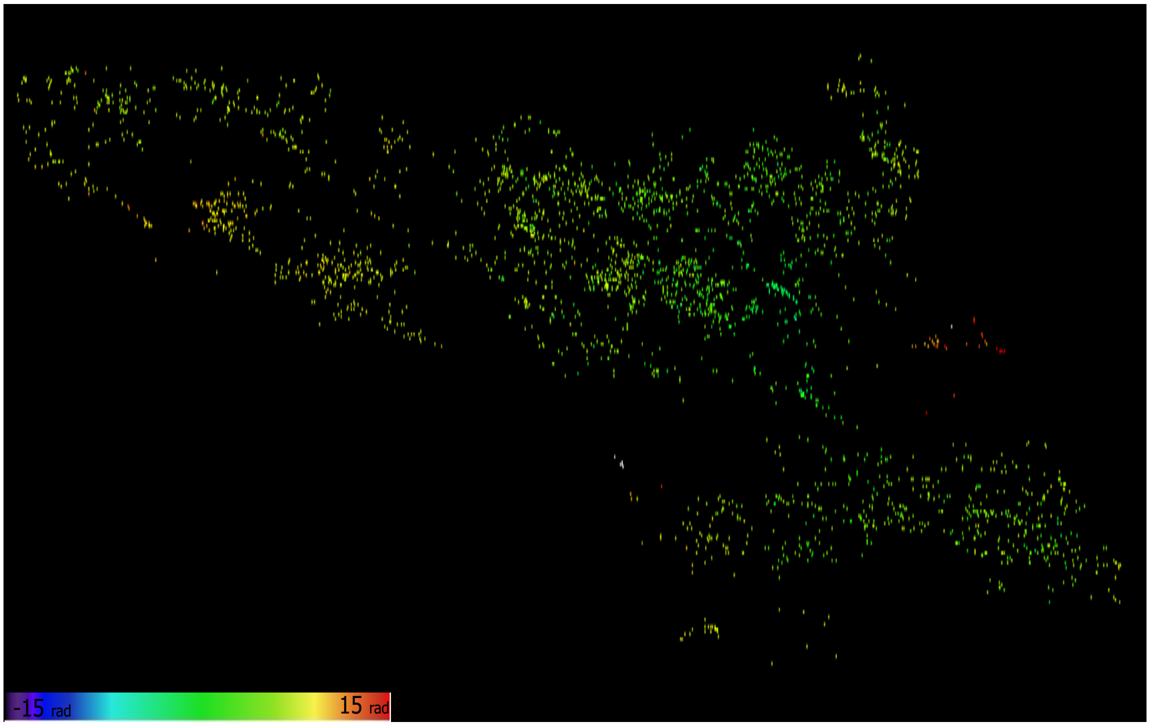

(b) Spatial distributions of standard deviations of residuals at the first iteration of the phase TS estimation.

Figure 3.4: Spatial distributions of standard deviations of residuals at the first iteration (a) and at the final iteration (b) of the phase TS estimation. Though the improvement from the first to the final iteration is notable, the map in (b) shows interventions are still required to further filter out affected points.

A redundant network ensures that any errors or discrepancies in the individual interferograms can be identified and corrected. With opportunities to check on gross errors in measurements, redundancy information can also provide a more precise and accurate estimation of the unknown parameters [40]. For this, a redundancy matrix, $\mathcal{R}$ constructed by considering the redundancy number of an observation is used to measure the reliability of observations. Observations vectors and estimated residual vectors are then related by the redundancy vector as in Equation 3.24 [129], [130] to optimize the quality of observation.

$$\hat{\xi} = \varphi - H\hat{\varphi} = (I - H(H^T WH)^{-1}H^T W)\Phi = \mathcal{R}\Phi \tag{3.24}$$

and it represents the distribution of errors from the LS estimates. The redundancy values are used as indicators of the reliability of observations [37]. This matrix is used to correct the LS residuals using the redundancy of the corresponding observations:

$$\xi_i = \frac{\hat{\xi}_i}{\mathrm{r_{ii}}} \tag{3.25}$$

where ξ_i is the corrected $\mathrm{i^{th}}$ residual, and $\mathrm{r_{ii}}$ is the $\mathrm{i^{th}}$ diagonal element of $\mathcal{R}$. The values range between 0 and 1 inclusive and as the value gets closer to 1 the easier the gross error to be detected. The ideal situation from a reliability point of view is when $\mathcal{R}$ equals the identity matrix I, which means that the residual of an observation is not affected by the error of other observations [129]. In an extreme case, when they are zeros, no gross errors, regardless of how large they are, can be detected. While on the other extreme, when they are ones, all gross errors, regardless of how small they are, can be detected [129].

It should also be noted that eliminating an observation characterized by a low redundancy could result in a weaker network. To avoid such a scenario and its possible impact, at each iteration— the algorithm implemented checks the available network of images and interferograms. If insufficient redundancy appears to be the case, the residual criteria is loosed and associated points with a residual value above the given threshold will not be incorporated in the set of outlier candidates [125]. Bearing their importance in mind, residual and redundancy parameters are used to derive QIs for PSs, interferograms, images, and images in a TS. These QIs are discussed in Section 3.5 and are supposed to show the reliability of measurements that also highlight the robustness of a technique to unmodeled PhU errors and outliers of observations [68].

3.5 Formulations of quality metrics

The advantages of MT-InSAR for monitoring small changes on the Earth's surface with high accuracy, large coverage, and remote sensing capabilities make it an ideal choice for a wide range of applications. The success of MT-InSAR, however, depends on several factors, including the quality of the data, the suitability of the terrain, and the availability of appropriate processing algorithms. Quality metrics are generally essential to ensure the accuracy, reliability, and interpretability of the interferometric products and those phase unwrapping errors. This section is dedicated to elaborating QIs derived from the residuals and redundancy information to characterize the reliability of interferometric data mainly in response to the PhU errors.

In practice, mainly in complex environments— unwrapping errors appear to be unavoidable causes of concern that requires an intervention for a better phase estimation. Identifying and removing affected input interferograms or pixels, that could also involve network modification, are among the approaches to suppress unwrapping error effects. QIs, on this regard, are essential tools to assess the reliability of MT-InSAR measurements and to identify and quantify features with uncertainty both spatially and temporally. Accordingly, in this thesis scores have been presented as viable QIs[††] of measurement points as well as for TS, images and interferograms.

[††] These QIs are published in Y. Wassie, S. M. Mirmazloumi, M. Crosetto, R. Palamà, O. Monserrat, and B. Crippa, "Spatio-temporal quality indicators for differential interferometric synthetic aperture radar data," Remote Sensing, vol. 14, no. 3, p. 798, 2022.

For m, ℓ and n, respectively, referring to the number of images, the number of interferograms and the number of points processed, formulation of the QIs involves the construction of multidimensional arrays in the following way.

1. Computing residuals from the first LS estimation Equation 3.13. The residual of the i^{th} measurement point in the j^{th} interferogram denoted by ξ_{ij} is computed by taking the difference of the unwrapped interferometric phase φ_{ij} and LS estimated phases of the associated master $\hat{\varphi}_{M_{ij}}$ and co-master $\hat{\varphi}_{S_{ij}}$ images.

   $$\xi_{ij} = \varphi_{ij} - \left(\hat{\varphi}_{S_{ij}} - \hat{\varphi}_{M_{ij}}\right) \tag{3.26}$$

   Considering each measurement point of the interferograms one obtains a 2D matrix of residuals with dimension $n \times \ell$.

2. The matrix in (1) is then modified to a binary matrix $\mathcal{M} = [\alpha_{ij}]_{1\leq i\leq n, 1\leq j\leq \ell}$ whose values are determined based on the piecewise function α_{ij}:

   $$\alpha_{ij} = \begin{cases} 1 & \text{if } |\xi_{ij}| \geq \xi_0 \\ 0 & \text{otherwise} \end{cases} \tag{3.27}$$

   while ξ_{ij} stands for the residual of i^{th} point at the j^{th} interferogram, ξ_0 denotes the residual threshold.

3. Compute a matrix of order $\mathrm{n} \times m$ whose entries are obtained from $\mathrm{k_{ir}}$ as:

   $$\mathrm{k_{ir}} = \sum_{j=1}^{q_r} \alpha_{ij} \tag{3.28}$$

   where $\mathrm{q_r}$ represents the number of interferograms connected to image r in the network. Note that $m < \ell$ as the number of images is much less than the number of interferograms in the case of MT-InSAR.

4. Entries of the matrix derived from Equation 3.28 are then multiplied by the corresponding weights assigned per image— i.e. multiplicative inverses of the number of interferograms in the network associated with each image.

$$\mathcal{B} = \begin{bmatrix} k_{11} & \dots & k_{1m} \\ \vdots & \ddots & \vdots \\ k_{n1} & \dots & k_{nm} \end{bmatrix}_{n\times m} \times \begin{bmatrix} w_1^{-1} \\ \vdots \\ w_m^{-1} \end{bmatrix}_{m\times 1} \tag{3.29}$$

$\min_i w_j > 4$ for $1 \leq j \leq m$ holds true.

The resulting weighted matrix $\mathcal{B}$, Equation 3.29, is finally analyzed to get scores for PSs and images that correspond to the three classes denoted by C_1, C_2 and C_3. The elements of a class resemble to each other in their reliability. Assuming much weight for the PhU error contribution in the phase estimation errors, elements of the first class are taken to be more reliable than the second and the third. The focus of this thesis is on assigning and analyzing scores for PSs, interferograms, images and TS products. The approaches followed in deciding these scores for the datasets are briefly presented below.

3.5.1 Interferogram score

Quality interferograms are essential for reliable SAR data analysis. Such interferograms enable more precise measurements of ground deformation, improved detection of small deformations, and better identification of phase unwrapping errors. These factors all contribute to more reliable conclusions and more valuable applications of SAR data. Poor quality interferograms, on the other hand, can make it difficult to identify phase unwrapping errors. These errors can result in incorrect measurements and unreliable conclusions. In line with this, a measure of the relaiblity of an interferogram called interferogram score denoted by S_{in} – is introduced. Typically, it is determined by analyzing the accumulated residuals obtained from the TS phase inversion. Vectors of residuals of measurement points per interferogram are considered to determine elements of S_{in}. Each interferogram is assigned to the classes based on Equation 3.30. The unions of the classes form the set $S_{\mathrm{in}} = \left\{ S_{\mathrm{in}}^{\mathrm{j}}, 1 \leq \mathrm{j} \leq \ell \right\}$. From the available ℓ interferograms, $S_{\mathrm{in}}^{\mathrm{j}}$ refers to the score of the j^{th} interferogram and its membership is determined the following way.

$$S_{\mathrm{in}}^{\mathrm{j}} \in \begin{cases} \mathrm{C}_3 & \text{if } \sum_{i=1}^{\mathrm{n}} [\![\alpha_{ij} = 1]\!] > \varepsilon_1 \\ \mathrm{C}_2 & \text{if } \sum_{i=1}^{\mathrm{n}} [\![\alpha_{ij} = 1]\!] > \varepsilon_0 \\ \mathrm{C}_1 & \text{otherwise} \end{cases} \tag{3.30}$$

where $[\![.]\!]$ represents the Iverson bracket[§]. The α_{ij} are the values as defined in Equation 3.27 and $\varepsilon_{s\in\{0,1\}}$ are thresholds to be determined by the operator. Generally, the scores are supposed to provide a global picture of the effect of PhU errors per interferogram. S_{in} helps to automatically detect less reliable interferograms from hundreds or thousands of interferograms. Note also that such a task is subjective, laborious, time-consuming and error-prone had it be done manually. The procedure may sometimes be accompanied by the exclusion of erroneous interferograms from the network. And this action commonly requires updating the network of interferograms and recomputing the phase estimation for improved results.

3.5.2 Image score

The inclusion of erroneous interferograms in an InSAR processing is sometimes attributed to the parent SAR image(s) forming the interferogram. In fact, SAR images can be affected by various factors including atmospheric conditions, terrain features and surface roughness with a potential to degrade their quality. These factors can introduce errors and noise in the InSAR processing, which can affect the accuracy and precision of the deformation measurements. To mitigate these effects, SAR image scores can be used

---

[§] The same notation is used for the bracket in Equations 3.31, 3.32 and 3.33 as well.

as potential QIs in ensuring the incorporation of reliable images in the InSAR processing. Especially, in the MT-InSAR setting the role of such a score is immense as it can help to automatically detect and identify issues among, probably, hundreds of images involved in the processing. An image score denoted by S_{im} – is a score assigned to images based on residuals obtained from the network of observations associated with an image. Like the case of interferograms, S_{im} shows spatially global effects. The score can ensure the reliability of images involved in the processing and that any errors or artifacts are identified and corrected. This is particularly important as the accuracy of processed images can have a significant impact on the conclusions drawn from the data. This score could also lead to the removal of one or more images, adjusting the network and recomputing the estimation. Images are assigned to different classes of reliability as per Equation 3.31.

$$S_{\mathrm{im}}^{\mathrm{j}} \in \begin{cases} C_3 & \text{if } \sum_{i=1}^{\mathrm{n}} [\![\frac{k_{ij}}{w_j} > \beta_0]\!] > \beta_2 \\ C_2 & \text{if } \sum_{i=1}^{\mathrm{n}} [\![\frac{k_{ij}}{w_j} > \beta_1]\!] > \beta_3 \\ C_1 & \text{otherwise} \end{cases} \tag{3.31}$$

The image score is thus the set $S_{\mathrm{im}} = \left\{ S_{\mathrm{im}}^{\mathrm{j}}, 1 \leq \mathrm{j} \leq m \right\}$. As the membership of images to the classes is influenced by the threshods, $\beta_{s\in\{0,1,2,3\}}$ used, careful and expert decision is required in picking the appropriete parameters. Overall, formulating image scores is essential for ensuring that the data is accurately and meaningfully interpreted and that any errors or artifacts are identified and corrected.

3.5.3 Point score

A good quality interferometric point scatterer has a stable phase behavior over time, and is unlikely to be affected by environmental factors, and has a low noise level. In contrast, a poor-quality point scatterer can be affected by atmospheric noise, seasonal changes, or other environmental factors, which can result in erroneous measurements due to phase unwrapping errors. The quality of a PS is important because it affects the accuracy and precision of the InSAR measurements. Inaccurate measurements can lead to incorrect conclusions about the magnitude and direction of ground deformation. For example, a poorly chosen PS may result in an underestimation or overestimation of the deformation signal, leading to incorrect conclusions about the geophysical processes causing the deformation. High-quality PSs, on the other hand, result in more accurate and precise measurements of ground deformation which can lead to more reliable conclusions. It is where the so-called Point score denoted by S_{pt} comes to an effect. The accumulated residuals generated in the observation period are used to compute the score per point. It is assigned to each measurement point and predominantly defines the spatially local and temporally global effects of PhU error. The score is used to further refine the number of measurement points to be used in the final phase of TS estimation. The score also provides supplementary information in the interpretation of TS results by separating reliable points from unreliable ones.

$$S^{\text{i}}_{\text{pt}} \in \begin{cases} C_3 & \text{if } \sum\limits_{j=1}^{m} [\![\frac{k_{ij}}{w_j} > \gamma_0]\!] > \gamma_2 \\ C_2 & \text{if } \sum\limits_{j=1}^{m} [\![\frac{k_{ij}}{w_j} > \gamma_1]\!] > \gamma_3 \\ C_1 & \text{otherwise} \end{cases} \tag{3.32}$$

For each i, and $1 \leq j \leq m$; the i^{th} measurement point p_i is assigned to either of the classes based on Equation 3.32 with threshold parameters $\gamma_{s \in \{0,1,2,3\}}$. The set of scores of measurement points S^{i}_{pt} is the same as the union of the C_i 's and is given by $S_{\text{pt}} = \left\{ S^{\text{i}}_{\text{pt}}, 1 \leq i \leq n \right\} = \bigcup_{i=1}^{3} C_i$ which is equivalent to the set of processed points. A brief pictorial illustration of the point score technique is presented in Figure 3.5.

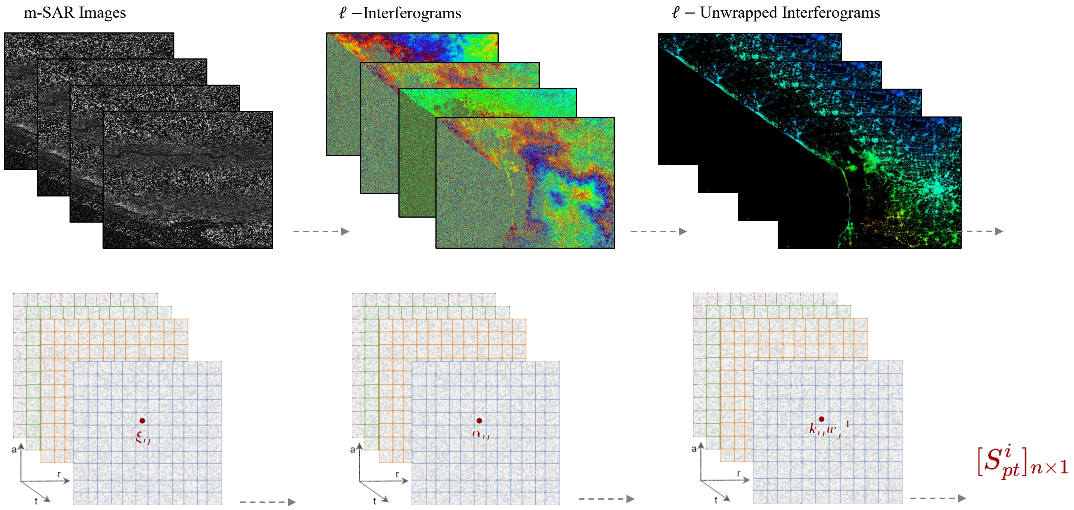

Figure 3.5: Illustration of the point score formulation. For ℓ interferograms obtained after setting proper space-time baseline constraints, residuals per point per interferogram are estimated from the phase TS estimation. The count of candidate outliers per point per image is then computed. This is followed by modifying the resulting stack of images by making use of the redundancy information. S_{pt} is then determined by analyzing the information per point along the images. The final result is an $n\times1$ column matrix of scores corresponding to the n measurement points.

3.5.4 Time series scores

As in the aforementioned cases, the use of TS scores as a quality index for a MT-InSAR data can help to identify and select reliable displacement TS for further geophysical analysis. The TS scores (S_{ts}) – is the tool responsible to associating a reliability flag to the estimated phase data at each time stamp of the time series. That is, a single measurement point will have as many scores as the length of the TS. These scores are based on the residual and redundancy information of the TS of estimated phases and are used to identify erroneous images as the dates of the time series also correspond to the processed images. Such a tool is important in the data analysis process, as it helps to identify periods of reliable and accurate data for further analysis and interpretation. The S_{ts} justify temporally local as well as spatially local effects of PhU error influences. The score corresponding to the TS of i$^{\text{th}}$ measurement point at the j$^{\text{th}}$ image/time is denoted by $S_{\text{ts}}^{\text{ij}}$ and is defined as:

$$S_{\text{ts}}^{\text{ij}} \in \begin{cases} C_3 & \text{if } \frac{k_{ij}}{w_j} > \delta_0 \\ C_2 & \text{if } \frac{k_{ij}}{w_j} > \delta_1 \\ C_1 & \text{otherwise} \end{cases} \tag{3.33}$$

where $\delta_{s \in \{0,1\}}$ represent the thresholds used. While S_{pt} defines whether a point is reliable or not, the S_{ts} indicates the exact date(s) of concern if any. The procedure to associate these scores is implemented in a similar way as illustrated in Figure 3.5, but for each image of every point this time.

Overall, the contribution of the tools is relevant, especially in automatically detecting and identifying erroneous interferometric measurements from big datasets. Extensive data analysis and expert judgment need to be followed in setting the proper thresholds which is a decisive factor in assigning the features of interest to different classes automatically. In all of the above cases, class C_1 is meant to contain the most reliable elements, and the elements in C_3 are the least reliable ones while elements of C_2 are at the margin. Those elements of C_3 could also be excluded from subsequent processing steps if most of the PSs are not in the area of interest or if the criteria set in Figure 4.11 is fulfilled. Such action can be considered as part of the PSs selection strategy as well and would have an advantage due to its data reduction effect.

On the other hand, detailed investigation–including analysis of possible effects of modifying the network and the resulting temporal baseline on the PhU should be done before taking similar measures for an image and interferogram assigned in C_3. Scores of PSs can be geocoded and visualized in a GIS environment to ease understanding and interpretation of the spatial distribution of reliable measurement points. In all cases, extensive data analysis and expert judgment will be a plus in tuning thresholds for better classification. Experience and being familiar with the case area are also important aspects for better judgment and analysis of the results. Experiments and results obtained by implementing the tools for different case areas are discussed in Chapter 4.

3.6 Conclusions

MT-InSAR is a powerful technique that allows for the measurement of ground surface deformation with high accuracy and temporal resolution. However, the quality of the resulting data is heavily influenced by various factors, including the characteristics of the data acquisition system, the processing algorithms used, and the environmental conditions during the measurements. To ensure the reliability of MT-InSAR data, it is essential to assess their quality using various metrics, including coherence, and temporal and spatial decorrelation. In this chapter, such metrics integrated into a version of the PSIG processing chain for the small baseline interferometric data have been briefly presented. The main contribution of the chapter has been extended to QI tools for interferometric products derived from a multi-master redundant network of interferograms. Key features of the proposed technique include four scores used to quantify the reliabilities of measurement points, dates in a TS, images and interferograms. The techniques are applied pixel by pixel in space and time to associate reliability scores highlighting the influence of PhU errors in particular. Moreover, the tools are valuable in quantifying spatially and temporally global and local effects of phase estimation errors from redundant MT-InSAR data. The proposed scores aimed at identifying and mitigating potential errors in the data, ultimately improving the quality and usefulness of MT-InSAR measurements. These also contribute to leveraging the power of MT-InSAR for a wide range of applications, including geohazard monitoring, land subsidence analysis, and infrastructure monitoring.

CHAPTER 4

APPLICATIONS OF QUALITY METRICS IN THE ANALYSIS OF SENTINEL-1 MT-INSAR DATASETS

4.1 Introduction

Detecting unreliable interferometric data is crucial to ensure accurate and reliable results in applications such as land deformation monitoring. As with any interferometric data, Sentinel-1 MT-InSAR data can be subject to various sources of noise and errors, which can affect the reliability and accuracy of the measurements. Quality descriptions play a substantial role in evaluating the impact on deformation estimates [131]— reliability tests, in this regard, allow for the detection and rejection of outliers due to phase unwrapping errors [40]. In the particular scenario—the global and local QIs, discussed in Section 3.5, respectively contribute to detecting and locating outliers within the dataset. Considering MT-InSAR, false positive measurement points and unwrapping errors impair the deformation estimates and consequently affect interpretations of products. The QIs introduced in Chapter 3 are supposed to play their part in this regard and are tested and validated in this chapter. Illustrations were performed on a set of real Sentinel-1 SAR SLC datasets acquired for case areas incorporating major, if not all, land cover types (including those with anthropogenic activities)—making them representative in providing important information in the validation of the tools. Details on the number, orientation, characteristics and parameters used in processing the images with the results and implications are discussed in the respective sections discussed below. It is also worth noting that some of the results discussed in this chapter are published in [*] [†] [§].

4.2 Detection of unreliable interferometric data

MT-InSAR is often applied to perform TS analysis and to estimate ground displacement over a given region from a stack of interferograms [29]. However, as with any interferometric data, Sentinel-1 data can be subject to various sources of noise and errors, which can affect the reliability and accuracy of the measurements. Unreliable InSAR data refers to data that is inaccurate, imprecise, or inconsistent with the expected measurements or the purpose they are intended for. Poor-quality SAR images or noise and unreliable interferograms (resulting from images of incoherent signals) or PhU errors particularly in areas with complex topography or rapid changes in surface deformation are among the many causes that are worth mentioning. Such datasets can result in incorrect or misleading interpretations of ground deformation, which can have serious consequences for planning,

---

[*] Y. Wassie, S. M. Mirmazloumi, M. Crosetto, R. Palamà, O. Monserrat, and B. Crippa, “Spatio-temporal quality indicators for differential interferometric synthetic aperture radar data,” Remote Sensing, vol. 14, no. 3, p. 798, 2022.

[†] Y. Wassie, S. M. Mirmazloumi, O. Monserrat, et al., “Interferometric SAR deformation timeseries: A quality index,” in Microwave Remote Sensing: Data Processing and Applications, SPIE, vol. 11861, 2021, pp. 19–27.

[§] Y. Wassie, Q. Gao, O. Monserrat, A. Barra, B. Crippa, and M. Crosetto, “Differential SAR interferometry for the monitoring of land subsidence along railway infrastructures,” The International Archives of Photogrammetry, Remote Sensing and Spatial Information Sciences, vol. 43,pp. 361–366, 2022.

monitoring or decision-making purposes. The reliability of the estimated outputs is highly influenced by the input data (does the spatial and temporal resolution fit for the purpose?), the processing approach (does the algorithms and/or model capture the required information and estimate parameters correctly?). Obviously, as no single data source or algorithm fit all different case areas due to the complex topography and land cover types, strategies to detect and identify errors need to be set for better estimation and interpretation of results. This is the objective of QIs of Section 3.5—to identify, locate and alleviate effects of PhU errors for a better TS or displacement estimation and is justified in the following sections for SAR dataset used in this thesis.

4.2.1 Erroneous image and interferogram detection

Identifying and also removing, if necessary, erroneous images and interferograms is an important step in InSAR data processing, as these can significantly affect the accuracy and reliability of the resulting displacement measurements. This section illustrates the results achieved in the implementation of the QIs discussed in the previous chapter for the purpose of detecting and/or removing images and interferograms. For this, Sentinel-1 SLC SAR images were acquired in the IW swath mode from the Venice lagoon, Italy. The area constitutes a densely urbanized environment, a tourist coastland, and rural areas. The availability of the datasets and richness in land cover types are also among the motivations behind the choice of the case area. For the study, 1795 multi-looked $(2_{\text{az}} \times 10_{\text{rg}})$ interferograms were generated by constraining the maximum temporal baseline to 84 days and 250m as the perpendicular baseline from 263 Sentinel-1A/B SLC images. The images cover the spatial extent shown in Figure 4.1 from a time span of more than five years. More information on these images is also available in Table 4.1. The proposed tools are beneficial as performing a visual inspection on such a large number of interferograms manually can be error-prone, time-consuming and/or labor-intensive which also leads to inaccuracies in the analysis.

Table 4.1: Sentinel-1 IW, SLC image product parameters—Venice, Italy

Feature	Descriptions
Pass	Descending
Sensor of the Super Master	S1A
Relative orbit	95
Frame range	438-443
Polarization	VV
Swath/Burst	02/{02,03,04}
No of images	263
Interferometric stack type	Baseline threshold
No of interferograms	1795
Image acquisition period	October 12, 2014— May 19, 2020

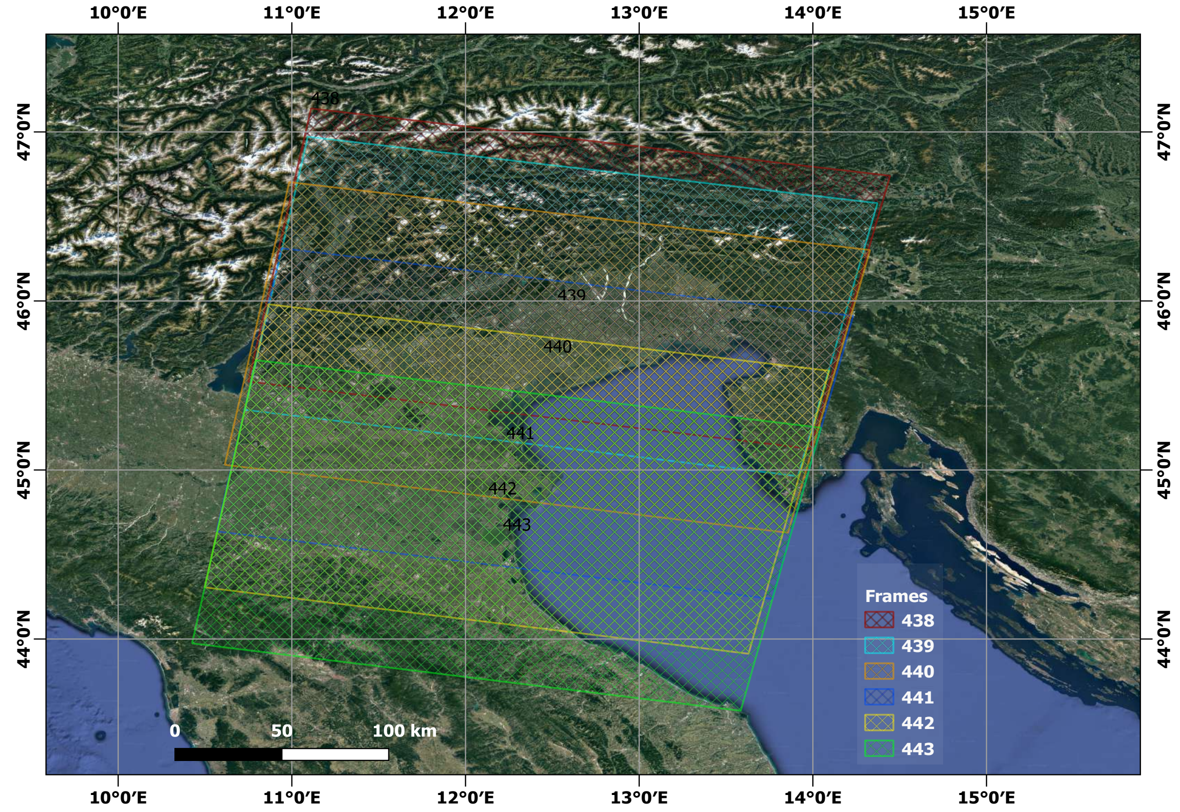

Figure 4.1: Spatial extent of frames of the processed SAR images of the Venice case area, Italy.

Moreover, Figure 4.2 illustrates the temporal and spatial baselines of interferograms used in the small baseline processing— edges correspond to interferograms and nodes to the images. As can be seen easily, the network gets denser after the launch of Sentinel-1B with an overall redundancy ranging from 5 to 16 interferograms. In order to detect and/or identify erroneous interferograms and images, the S_{in} (Subsection 3.5.1) and the S_{im} (Subsection 3.5.2) tools were implemented. Generally, the result has indicated that the interferograms considered in this experiment look acceptable and by tightening the threshold value less than 8% of them found in the less reliable classes C_2 & C_3.

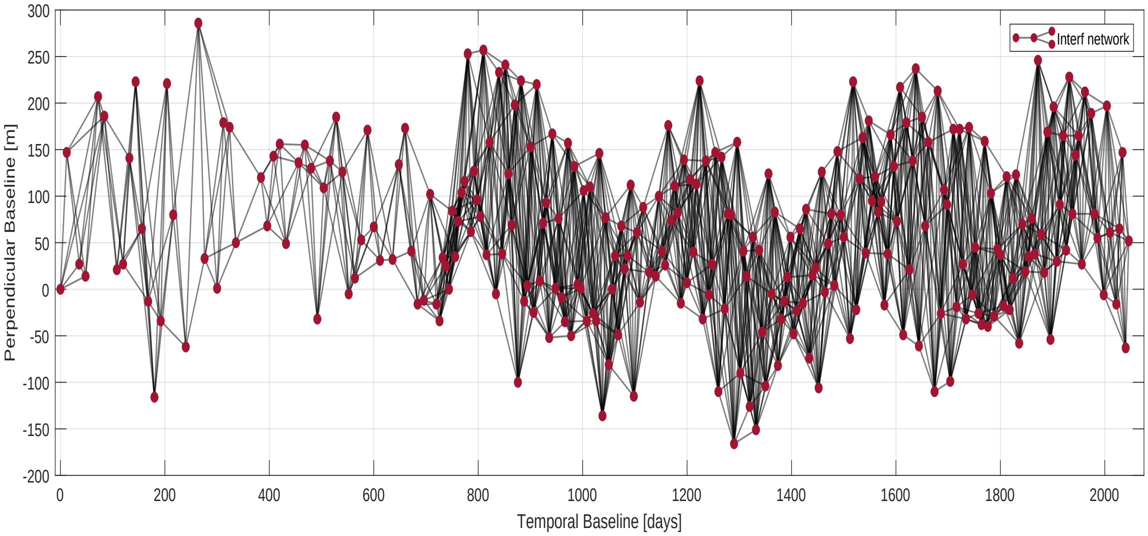

Figure 4.2: The network of interferograms used in the MT-InSAR processing for the case of the Venice case area, Italy. The red dots are the nodes representing the images and the associated edges referred to the interferograms generated from the images at the corresponding end nodes. In this case, a total of 1795 interferograms were generated from 263 SLC images covering the period from October 2014 to May 2020. Among these 1786 of the interferograms are with a maximum temporal baseline of 48 days, and 9 of them are with a temporal baseline of 60, 72 and 84 days. Images considered in this processing cover the period from October 2014 to May 2020 and temporal and perpendicular baselines were computed with respect to the first image. Details on these processed images including the redundancy information are presented in Appendix A4.

Figure 4.3 (a) is among the interferograms grouped in the less reliable class C_3. By S_{im} tool, two of the total 263 images have been classified in the unreliable class. This QI, has also justified that unreliable images are those associated with affected interferograms. For instance, assessing the interferogram scores of image 44, one of the two images classified in the unreliable class, it is found that five of the seven interferograms associated with it are classified in C_3 (Figure 4.3).

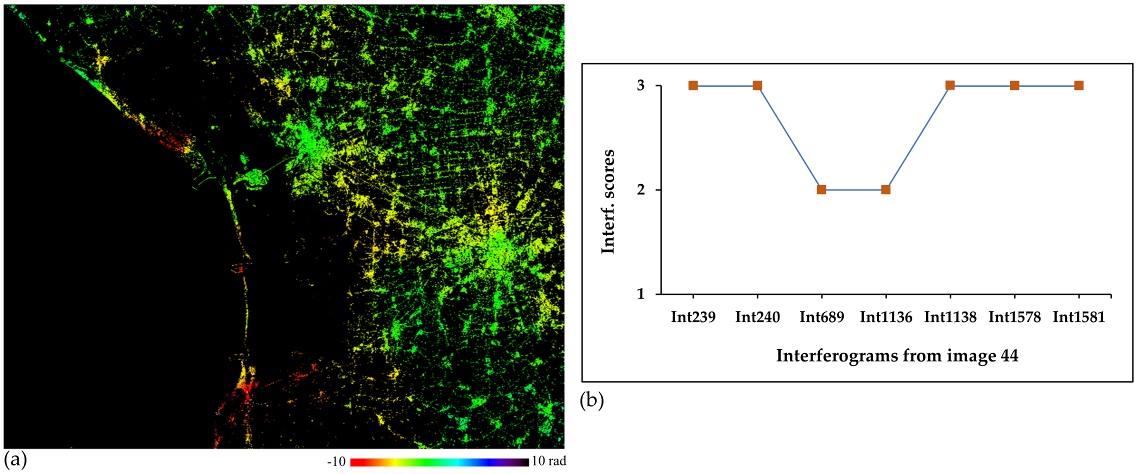

(a) (b)

Figure 4.3: Example of unwrapped interferogram classified in C3 shown in (a) and plot of scores of interferograms associated with image 44— which is the image classified in C3 and used to generate the interferogram in (a).

Many of the erroneous measurement points are located in the tourist coastland Sottomarina area— bottom part of the scene in Figure 4.4 (b). Though the temporal gap between images 43 and 44 is 12 days, phase discontinuities are seen from the 43rd to the 44th cumulative phase (Figure 4.4(c)). Considering the nature of the area and based on the phase information, the problem could be attributed to phase unwrapping errors. In line with this, the phase history of the PSs in the affected area was explored and clear phase unwrapping errors were found in image 44. Just to mention one— a phase jump of around 6.21 rad has been recorded from 2016-07-09 to 2016-07-21. This particular result has illustrated the contribution of the S_{im} score. After excluding the two unreliable images and

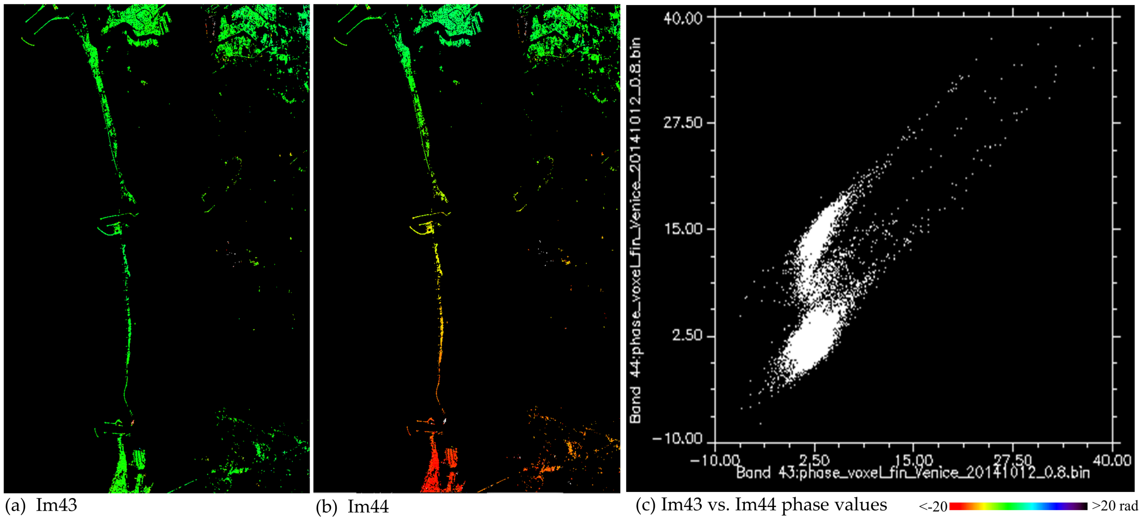

(a) Im43 (b) Im44 (c) Im43 vs. Im44 phase values

Figure 4.4: Subsets of processed images of cumulative phases with different scores (in radar geometry): image 43 classified in C1 (a) and image 44 classified in C3 (b). The scatter plot in (c) is obtained from phase information of image 43 (horizontal axis) and image 44 (vertical axis). The abrupt changes and clusters of phases that are distant from the main distribution of phase values are potential results of the phase unwrapping errors. The result has indicated that the data need to be reassessed.

the thirteen associated interferograms, the datasets were reprocessed resulting in better TS information as can be seen in Figure 4.5, for instance. The example in this Figure clearly justified the role of the scores in the detection of PhU errors automatically that are not correctly identified by the phase estimation approach.

4.2.2 Unreliable point detection and classification

This section aimed at detecting and identifying less reliable measurement points among the available points identified at the point selection step. Though it depends on the type and size of the case area, often millions of points are extracted for processing. Of course, these points are not free from PhU errors and hence require further extraction criteria for a better displacement estimation. And, that is where the point scores tool comes to effect—more importantly, to address PhU errors and their effects. In this thesis, the point score,

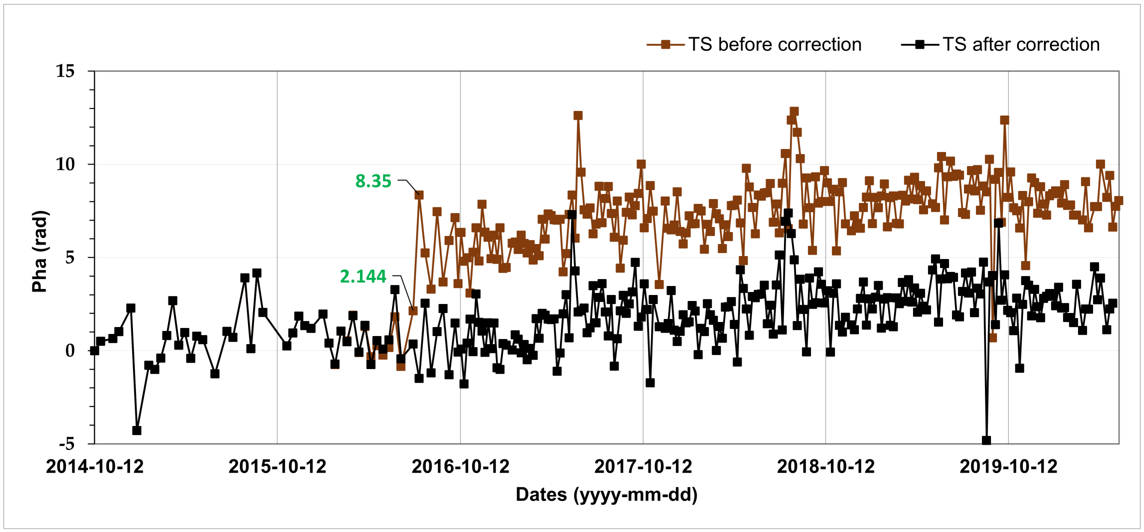

Figure 4.5: Effect of an erroneous image on the phase TS estimation. These are TSs of the same point from the Venice lagoon. The TS in black is obtained after excluding the erroneous image 44 which resulted in a PhU error in the brown TS before the correction.

S_{pt} tool was examined for 432,311 coherent measurement points ($\Gamma_0 = 0.4$) that were derived from the Venice lagoon case area for the parameters described on Table 4.1. The classification was done for three classes as in the case of images and interferograms— and found that 95.81%, 3.80% and 0.39% of the points were respectively classified in C_1,C_2 and C_3 classes. This indicates that less than a percent of the processed points is unreliable. The advantage of the tools lies in the fact that inspecting unreliable points from such a huge number of measurement points is often unfeasible as it would be subjective or time-consuming. The spatial distribution of all scores and those classified in C_1, C_2 and C_3 are depicted in Figures 4.6 and 4.7.

Identifying the cause of PhU errors associated with such points is also as important as detecting the points. As one might expect, this is not always an easy step. But, if one manages to sort it out, we may consider the following scenarios. In the presence of sufficient points in the target area— excluding the unreliable points of C_3 from further processing would be an immediate solution to follow and has been the case for the 1695 points in this experiment too. Doing so can improve the processing load and time on upcoming phase estimation steps by reducing the data. On the other hand, in the case that affected points lie in a part of the target area, which is mostly the case, a similar decision is going to affect critical target points and hence the analysis, adjusting the path of integration or changing the reference point could be an option. This is recommended in sparsely populated points and in the presence of, for instance, water bodies between measurement points.

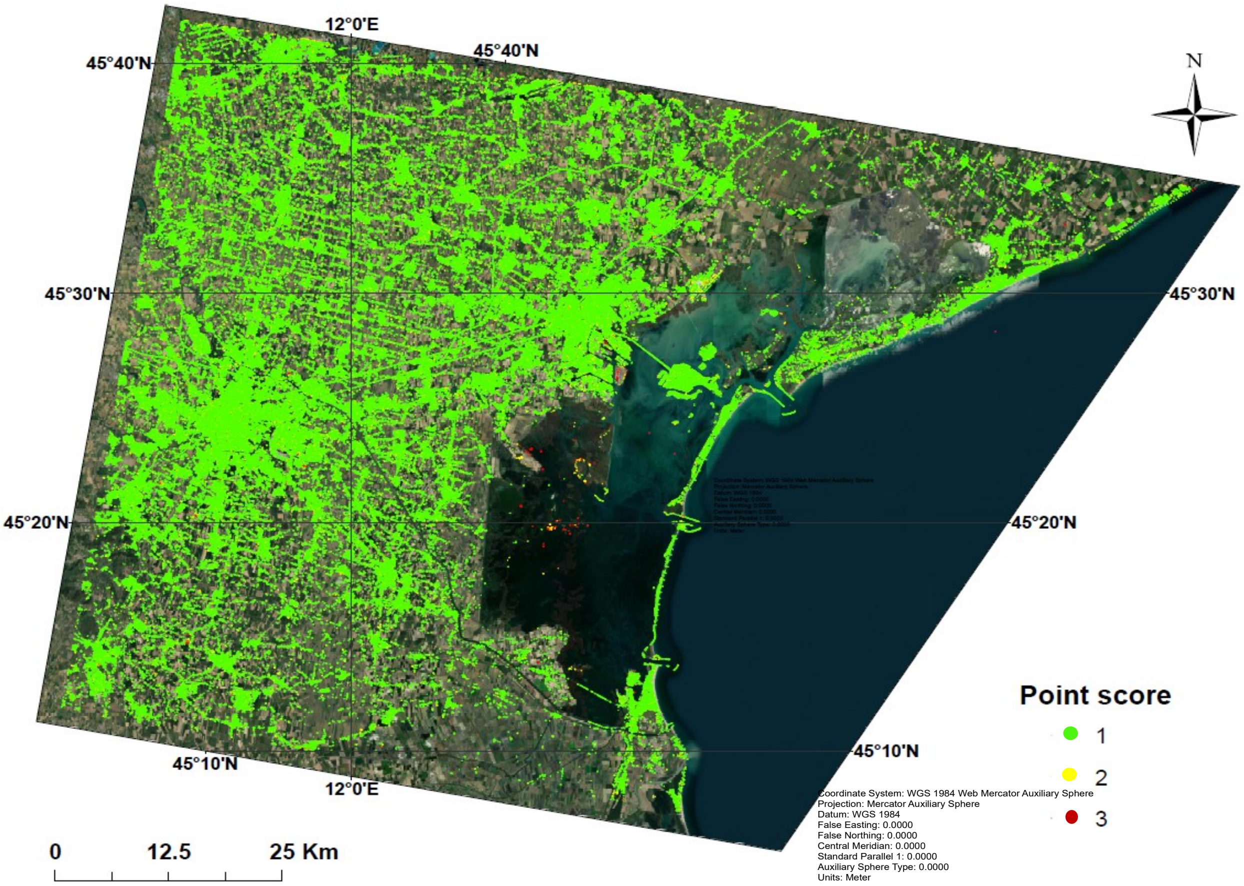

Figure 4.6: Map of classified measurement points to the three classes of reliability— the green points indicate reliable points with score 1 and belonging to C_1. Those yellow and dark red points respectively refer to the marginal and unreliable points taken from the Venice lagoon, Italy.

Masking the most affected/suspected area, of course, is an option too to exclude such erroneous points.

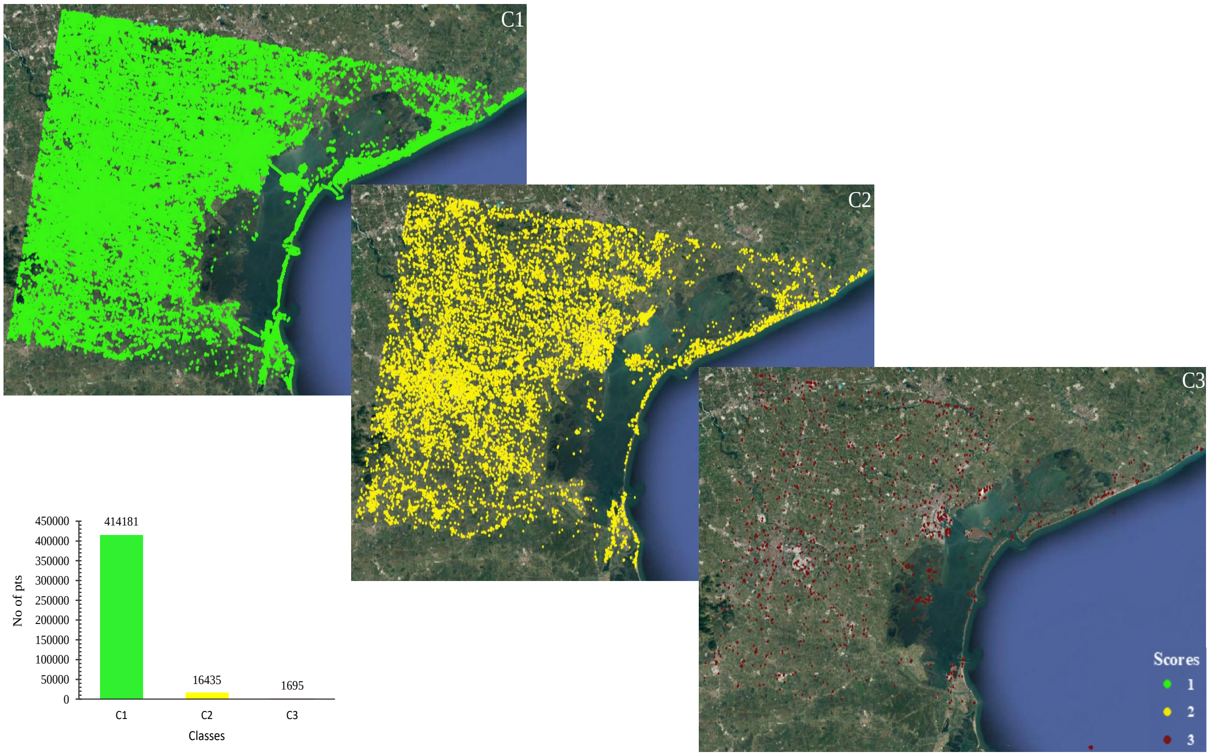

Figure 4.7: Quality scores mapped per class for the PSs taken from the sub-area of Venice lagoon, Italy. As per the classification of this particular scenario, the map on the top left represents the map of the 414181 reliable points that belong to C1 and the dark red points on the bottom right represent the map of 1695 unreliable points that are elements of C3. The map in the middle, representing PSs in yellow, is for the marginal less reliable 16435 points belonging to C2.

The spatial distribution of the cumulative phases was also assessed along with the distribution of associated point scores. The result has indicated that most of the points classified in C_3 are the points that are also found in and around the Venice lagoon as seen in Figure 4.8. The terrain in the lagoon which is mainly characterized by a complex network of canals, islands, and sediment deposits can affect the coherence of the radar signal—and hence leading to errors in the measurements. The concentration of unreliable points in this area is also attributed to the properties of the soil, and the effect of human activities such as dredging, construction, and pumping.

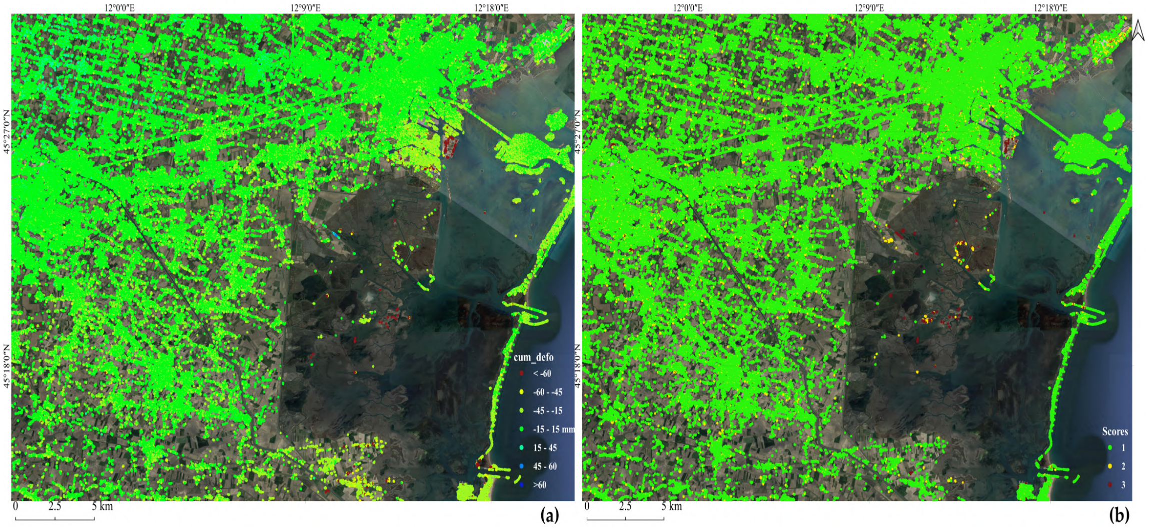

Figure 4.8: A closer view of comparison of geocoded cumulative phase information at the final image (a) with the quality scores (b) for the PSs taken from the sub-area of Venice lagoon, Italy.

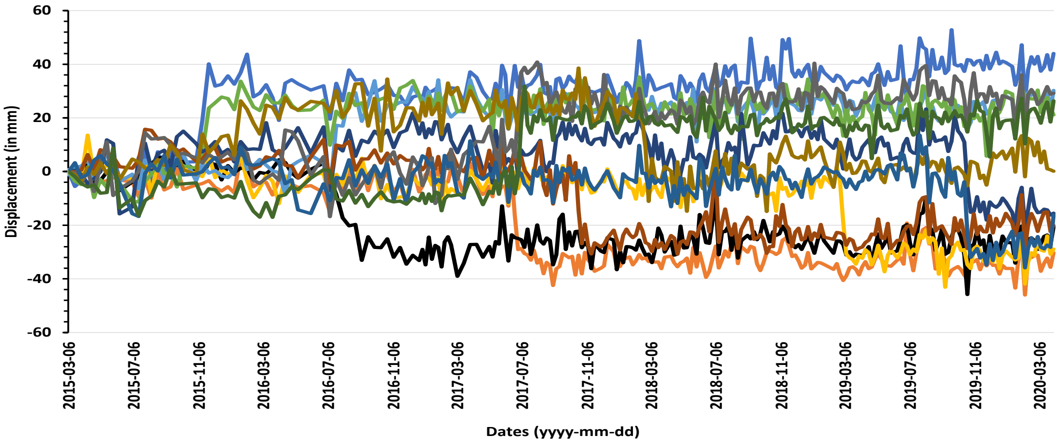

Figure 4.9: TS of sample points belonging to class C3 taken from Barcelona case area, Spain. The different colored TS corresponds to different PSs. In each of the cases, a PhU jump was detected at different instances in the temporal period.

Among the elements of C_3, points with PhU errors are evident and their TS plots are depicted in Figure 4.9. The spatial extent of the case area and the associated parameters are respectively presented in Appendix A5.4 and in Table 4.2. One of the interesting facts about this result is that such points are classified in the unreliable class by using the residual information and not directly using the post-processed phase information.

4.2.3 Labeling displacement TS

This step mainly involves identifying erroneous measurements of a TS and tagging a quality score for a point at each image in the observation period. For each measurement point, a TS of scores S_{ts}— with each score corresponding to an acquisition date of the SAR image were also generated. Such an approach is useful for improving the interpretation and analysis of data and can provide valuable insights into the underlying deformation processes occurring within the study area. Below, the TS scores for four of the processed PSs are demonstrated. These scores as well indicated the reliability of a measurement point at a particular date/image.

The scores of the point in Figure 4.10(a) for instance are all one in the whole period of observations, justifying the corresponding TS is reliable throughout the period and hence conclusions are drawn from it as well. Most of the jumps in Figure 4.10(b-d) are also captured in the TS score. It is worth mentioning that a particular date of the TS belongs to the set C_3 doesn't always mean a phase jump will be detected at that instance but rather how reliable that measurement is— this is particularly evident in a few occasions of plots (b) to (d) of Figure 4.10.

4.3 Quality indices as point selection tool

One of the key challenges in InSAR data processing is point selection, where the goal is to extract points that exhibit a consistent signal with minimal noise over time. Typical techniques of point selection are threshold-based (refer to section 3.3 for more on this).

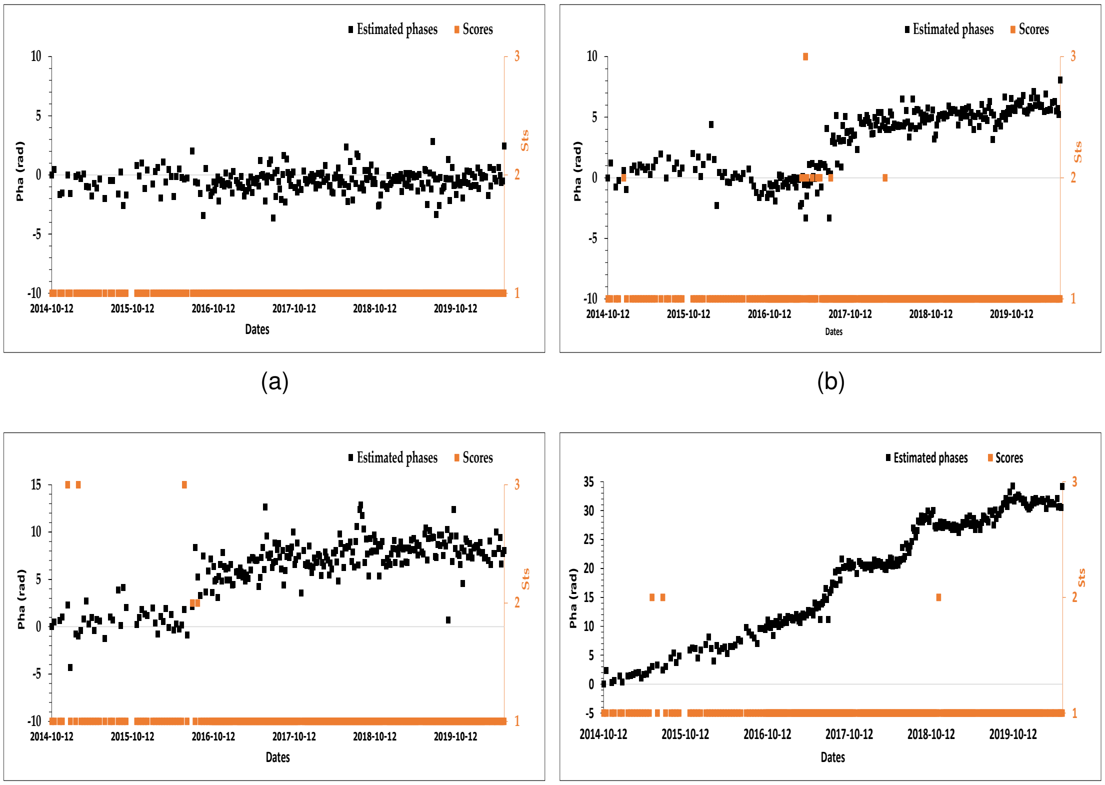

(a)

(b)

(c)

(d)

Figure 4.10: Plots of TS of estimated phases (shown in black color) and the associated scores (shown in orange color) of the TS at each measurement time stamp.

Picking the optimal threshold of the point selection is, however, not always straightforward and depends on various factors such as the nature of the data, the level of noise, and the desired level of precision. This section highlights how we could utilize the point score, S_{pt} tool to set a threshold parameter for measurement point selection in MT-InSAR processing. The technique helps to improve the accuracy and reliability of the InSAR deformation measurements by identifying and selecting measurement points that are of the highest quality and reliability. In addition, the point scores can be used to prioritize and select interferometric points that are most suitable for specific applications or analyses, such as those that require high precision or accuracy. It is also noteworthy that the use of InSAR point scores as a point selection tool should be used in combination with other point selection techniques to optimize the quality of the InSAR data.

To demonstrate this, two case areas were considered— the subset of the Venice lagoon and the Barcelona railway network. In either of the cases, the set of coherent measurement points was selected based on the metric shown in Equation 3.4 [32]. The procedure is implemented based on the hypothesis that no existing phase unwrapping algorithm is immune from PhU errors. And, thus it is tried to reinforce existing methods toward a reliable set of pixels based on a quantitative metric defined in Equation 4.1— hereafter called labeling performance criteria. It is defined based on the classes identified in S_{pt}. The labeling performance indicates the percentage of points clustered in the more reliable group. Saying another way— from a possible domain of thresholds the criteria help to pick the one that probably leads to a better phase estimation. The higher the value of $\mathfrak{q}$ the better the set of points involved in the processing would be. It is given by:

$$\mathfrak{q} := \left(1 - \frac{1}{\mathsf{W}_1\aleph_1}\sum_i \mathsf{W}_i\aleph_i\right) \times 100\% \tag{4.1}$$

where $\aleph_i$ and W_i for $i \in \{2,3\}$ denote the number of points in the corresponding class $C_{\mathrm{i}\in\{1,2,3\}}$ (as per the definition in Section 3.5) and associated weights respectively. The experiment was conducted by setting the weights $\mathsf{W}_{\mathrm{i}\in\{1,2,3\}} := 1$ and $\mathfrak{q} \geq 95\%$ as an acceptable range. Apparently, the weights might be considered from the average of the standard deviations of phase residuals or from the amplitude timeseries of the points from each class.

The approach has the potential to save unnecessary processing time and energy as it indicates distributions of erroneous pixels ahead of the final step. In case the value of $\mathfrak{q}$ of Equation 4.1 is smaller— meaning lots of points are found in the unreliable class, it is advised to reprocess the data preferably from the point selection step. Changing the reference point, and masking areas likely affected by PhU error are also to be considered.

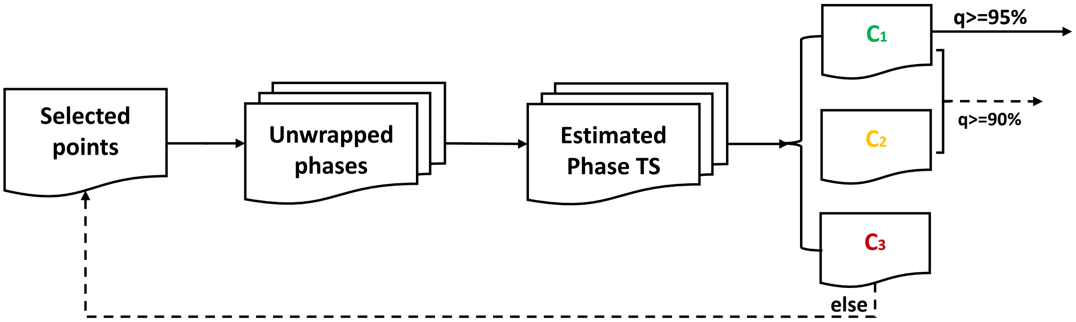

Figure 4.11: Brief implementation steps to use S_{pt} to filter-out less reliable points.

On the other hand, if the value of q is found in the range of acceptable values, it is a green light to proceed to the next step of the processing. This, of course, doesn't mean the data is clean rather effects of erroneous points within the data are minimal and tolerable. The labeling performance criterion and the procedure highlighted in Figure 4.11 could be taken as an extended points selection technique that can be used along with other pixel selection criteria. Augmenting commonly used pixel selection criteria with such quality indices is like certifying the points for further processing. The relevance of the procedure has been tested on the Venus lagoon, Italy and on a part of the railway segment in Barcelona, Spain and results are briefly summarised below.

4.3.1 Venice Lagoon, Italy

For this experiment, a subset from the Venice lagoon case area was considered by setting the point selection thresholds to 0.6, 0.7, 0.8 and 0.9. Choosing the right threshold parameter leading to an optimal result is, however, one of the challenging aspects in point selection techniques of MT-InSAR data processing. Achieving a trade-off between quality and the density of measurement points is one aspect many operators trying to achieve. The results of this experiment showed how one can achieve such goals by blending both qualitative and quantitative information. As can be seen from plots (a) to (d) of Figure 4.12, the number of processed points per class (or per threshold) and the threshold values are inversely proportional. This has been also summarized in plot (e). The effect of the threshold on the total number of points per threshold is presented in plot (f) as well. Seemingly, results from thresholds 0.8 and 0.9 were found in the solution space, and the former was taken as a convenient choice due to the density of measurement points (Figure 4.12). Working with threshold 0.9 is also possible, but doing so will cost around 37.6 % points from the reliable class— C_1.

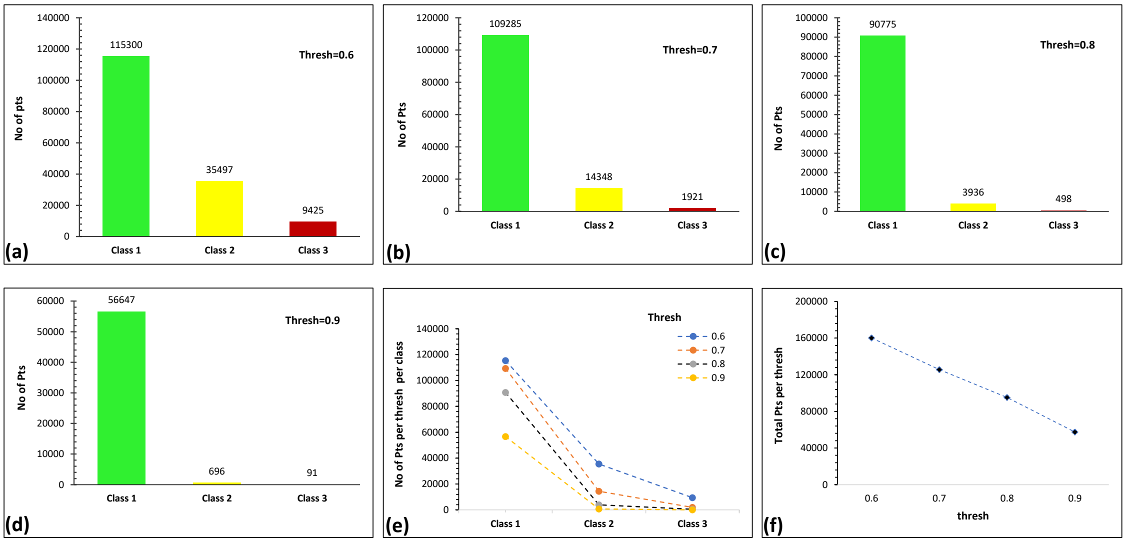

Figure 4.12: Comparison of threshold and density of measurement points. The number of processed points (total number and numbers per class) gets decreasing as the value of the threshold goes from 0.6 to 0.9— refer to plots (a) to (d). This result has been also summarized in the plot (e). The effect of the threshold on the total number of points per threshold is also presented in the plot (f).

The spatial distribution of clustered measurement points per class per threshold is presented in Figure 4.13. It is helpful to visually inspect affected areas by identifying the distribution of less reliable points from the main target areas. As a result of which, such maps do also play a crucial role by providing qualitative information to operators toward informed decision-making.

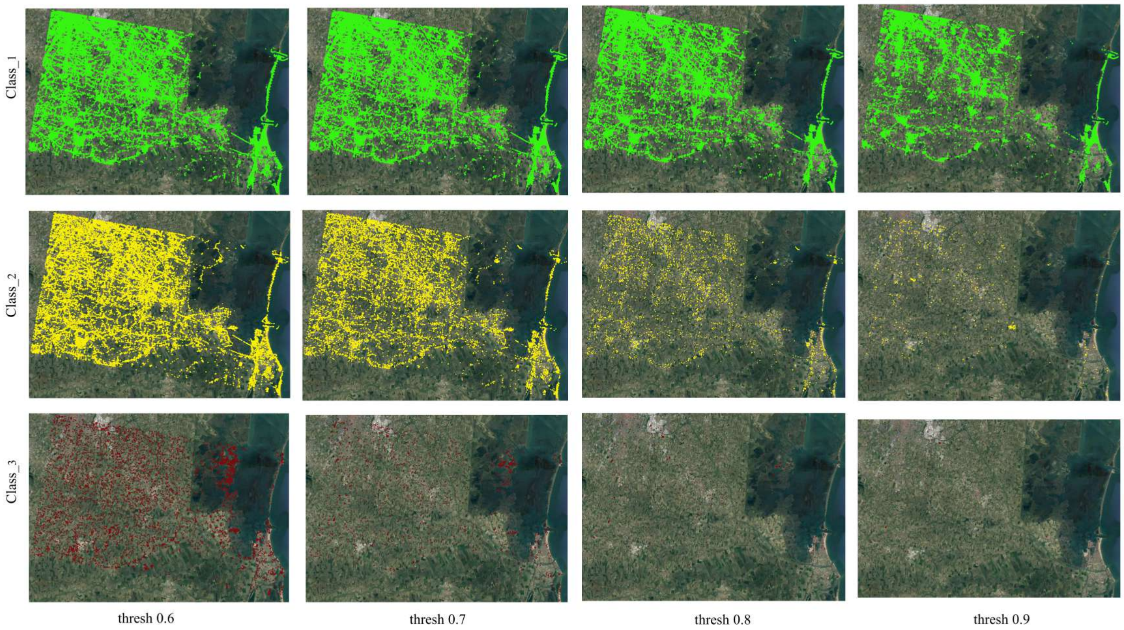

Figure 4.13: Spatial distribution of classified measurement points per class per threshold. Maps on each row correspond to maps from each class (C_1 in green, C_2 in yellow, and C_3 in maroon color) and the columns correspond to the threshold parameters.

4.4 Rail transit infrastructure monitoring, Barcelona, Spain

This section is dedicated to further elaborating the S_{pt} and S_{ts} tools as per the procedures discussed in Section 4.3.1, but in more specific context— in monitoring subsidence along rail transit infrastructure in Barcelona, Spain. The experiment has been done on 14,180 points extracted from 270 Sentinel-1 SLC images covering around 60 km of the rail transit network in Barcelona following the steps presented in Figure 3.1. The points were selected as per the criterion indicated in Equation 3.4. Some of the parameters used for the processed images are shown in Table 4.2. As in the case of the Venice lagoon area, spatial and temporal baseline constraints were set to reduce possible decorrelation effects. At times the unwrapping error correction results in an omission error— TSs with a $2\pi \pm \epsilon_0$ phase jump, for some error ϵ_0, would be incorporated in sets C_2 and C_3. But, it is also

Table 4.2: Sentinel-1 IW, SLC image product parameters—Barcelona, Spain

Feature	Descriptions
Pass	Descending
Sensor of the Super Master	S1A
Relative orbit	110
Frame range	454-456
Polarization	VV
Swath/Burst	{01}/{04,05}
No of images	270
Interferometric stack type	Baseline threshold
No of interferograms	1283
Image acquisition period	Jan 24, 2016— November 29, 2021

good to note that a point belonging to either of the sets doesn't necessarily mean there is a phase jump in the TS of the point. Figure 4.14 (a) indicated that, in the year 2017, the deformation value of the point dropped from -16.294 mm to -45.275 mm. Similarly, for the point in Figure 4.14 (b), a jump approximately equal to 2π rad was detected in 2021.

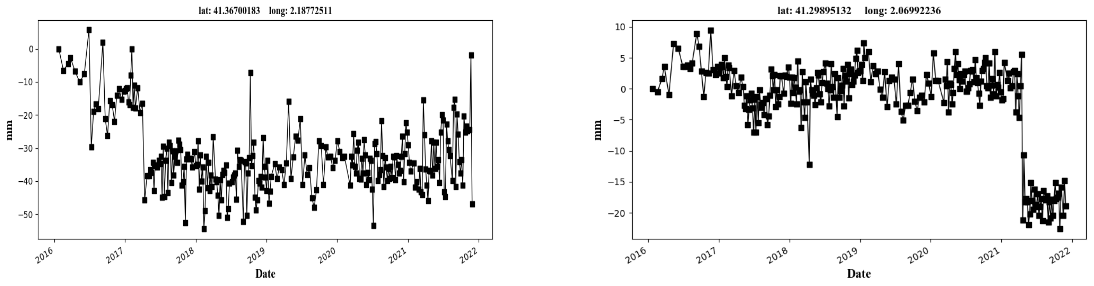

(a) (b)

Figure 4.14: Examples of displacement TS affected by an unwrapping error. Jumps due to unwrapping errors were observed in 2017(a) and in 2021(b) from Sentinel-1 SLC images taken from Barcelona, Spain.

Each TS of a point was also associated with TS of scores— with each score referring to the reliability of the measurement taken at a particular image acquisition date. Of course, it indicates the quality of an estimated phase for a point on the target image. For instance, the TS of scores in Figure 4.15 (orange diamonds) corresponds to the TS evolution of measurements at each sampling date and all have got a score of one. Interestingly, the deformation TS of the same point (black squares in Figure 4.15 (a) has also justified the stability of the point. The standard deviation for the TS measurements of the point in Figure 4.15 (a) is 0.72mm and the deviation is 3.47 mm for the point in Figure 4.15 (b).

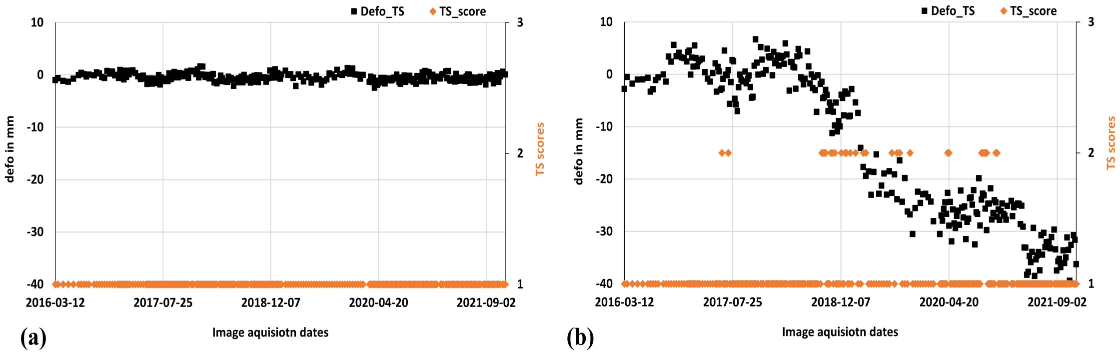

Figure 4.15: Labels of a TS—Deformation TS measurements (black squares) and the associated TS scores (orange diamonds): for a reliable point (a) and for a less reliable point (b). In (a) all TS scores have got one and spread on the horizontal axis, unlike the case in (b).

The final cumulative deformation map and the spatial distribution of the associated quality scores are, respectively, presented in Figure 4.16 (a) and (b). From the classification point of view, the result has indicated that more than 98% of the points were assigned to C_1 and less than 2% of them to C_2 and C_3. On a larger scale, the technique can be used to reduce datasets and minimize the risks of misinterpreting TS products. By the way, the experiment has also shown that MT-InSAR techniques are real deals in monitoring subsidence along above-ground railway infrastructures. They can be considered powerful tools that can help improve safety and reduce the risk of infrastructure failures along railway tracks. On the other hand, for underground subways along agricultural fields, it was noticed that the density of measurement points is lower. This may lead to the incorporation of unreliable points that make subsidence monitoring more challenging.

(a) Railway cumulative deformation

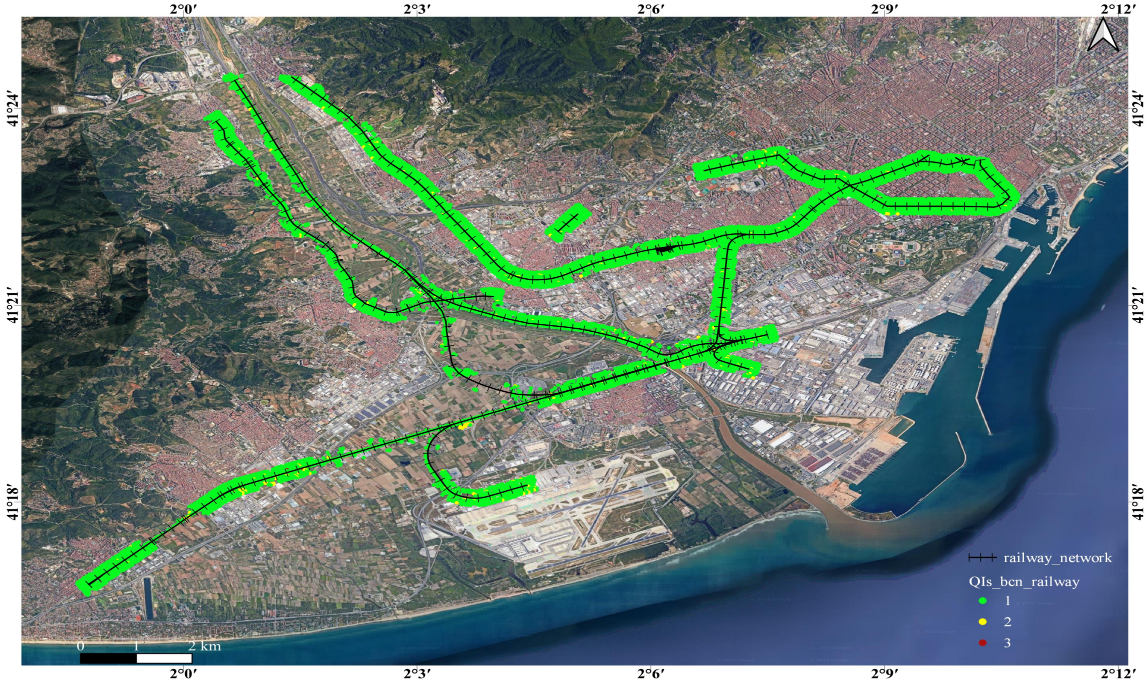

(b) Associated quality indicators to the point

Figure 4.16: Map of displacement cumulative phase TS for (a) the Railways segment from Sentinel-1 SLC images taken from Barcelona, Spain. (b) and associated QIs to the points in (a). Results from both (a) and (b) are geocoded to the same reference system.

4.5 Conclusions

In this chapter, the role of quality metrics in the analysis of Sentinel-1 MT-InSAR datasets were illustrated. The QIs proposed in Chapter 3 were used to identify and mitigate errors, particularly for measurements derived from big Sentinel-1 datasets acquired at different case areas— and sample results from Venice, Italy and Barcelona, Spain were discussed. In particular, validations of the four scores for a measurement point, images, interferograms and dates in a TS were validated for complex SLC SAR real datasets. The result has justified the importance of model-independent quality-checking mechanisms. The capabilities of the tools in detecting and pinpointing incorrect measurement points within a large dataset containing hundredths of thousands of points have been justified. Additionally, these tools were able to automatically detect and isolate images and interferograms mainly affected by PhU errors respectively from a pool of hundreds of images and thousands of interferograms. Furthermore, the tools were also able to identify the specific image or acquisition date where a TS of a point is affected by errors was identified. By including the QIs in the MT-InSAR processing chain, it is managed to capture PhU errors overlooked by the existing approaches and with a potential risk for misinterpretation had they not been identified. The use of one of the QIs— S_{pt} as an integral part of the PS selection strategy is also worth mentioning as a viable contribution to the chapter. It is a metric to easily decide a proper point selection threshold. Overall, the contribution of QIs for big MT-InSAR data analysis and interpretation has been proved.

CHAPTER 5

CONCLUSIONS AND OUTLOOK

The increasing availability of radar images collected by constellations of satellites for the monitoring of Earth's surface and its changes over time prompts the development of several interferometric SAR algorithms and methodologies. As a well-established geodetic technique for Earth surface deformation monitoring, the reliability of MT-InSAR time-series products and their potential error sources should be addressed. The reliability of the deformation estimates is rooted in the quality and number of exploited images, associated interferograms and selected measurement points. Moreover, incomplete representations of factors affecting deformation measurements may lead to omission errors and hence an incorrect estimation and interpretation of deformation time series. In this regard, quality metrics quantifying involved parameters and their impact play a huge role in the detection and rejection of outliers leading to such problems. Accordingly, this thesis was aimed at retrieving reliable MT-InSAR products by detecting and resolving measurements affected by PhU errors. Complementing MT-InSAR processing chains with such tools will ease interpretations of products and is supposed to help build the trust and confidence of end users to integrate MT-InSAR products in their decision-making activities. The main conclusions of the thesis, limitations and future work plans are briefly discussed in the following sections.

5.1 Conclusions

From its very nature, SAR interferometry is complex and susceptible to uncertainties accounting for the uncontrolled medium of signal transmission and back-scattering targets or due to the difficulty (or limited knowledge) of fully representing model parameters. The widely known MT-InSAR techniques, generally, aim at extracting the temporal evolution of deformations of targets with coherent scattering behavior from a stack of SAR acquisitions of the same area relative to temporal and spatial references. On the other hand, due to the complex nature of SAR images (acquisitions), addressing all possible model parameters in a comprehensive manner is still challenging and a source of error in MT-InSAR data processing. In particular, the PhU step is yet a challenging problem that leads to the incorrect estimation of the deformation time-series. At times the unwrapping error correction results in an omission error— TSs with an integer multiple of $2\pi \pm \epsilon_0$ phase jump, for some error ϵ_0, would be incorporated in the analysis. If not properly corrected, PhU errors may degrade the quality of the estimated ground displacement and appear to be one of the major causes for misinterpretation of final products as well. Techniques to detect and identify errors, if possible, and otherwise attaching scores highlighting the level of reliability of the estimated measurements need to be set for a better interpretation of final results. Accordingly, in this thesis detecting, identifying, and classifying PSs and images impacted by PhU errors were accomplished with the objective to lessen their influence on the interpretation of final displacement TS.

The tools make use of post-PhU estimated phase residuals derived from a redundant network of interferograms to formulate quality indices used as indicators of the reliability of the measurements. The key features incorporate four scores associated with the reliability of measurement points, images in a TS, images, and interferograms. In all cases, measurements were classified into three classes based on the reliability of measurements. Knowledge of the case area and expertise were among the crucial factors in setting thresholds for assigning the features of interest to different classes automatically. In the particular scenario— points affected by PhU errors that were detected in the Venice lagoon, Italy, for instance, were successfully classified in the less reliable classes. The techniques were applied pixel by pixel in space and time to associate reliability scores highlighting the influence of global and local PhU errors in the course of the phase estimation. As far as the redundancy parameter is kept above the threshold, experiments had justified that excluding less reliable images/interferograms from the network had improved the TS estimation. Careful investigation of the effects of such measures and hence the updated network on the phase re-estimation should be kept in mind. Assessing and cross-validating the number of affected pixels in the target area is a smart move as well.

Another important aspect of the thesis is the use of the point score tool as a candidate pixel filtering technique. The methodology contributes by providing quantitative information on the percentage of reliable pixels after the phase unwrapping step. The experiments on this regard justified that the tool adds extra dimensions responsible for PhU errors to existing pixel selection techniques. Using it in conjunction with existing point selection techniques will further guarantee the inclusion of reliable points in the process. That is, candidate PSs that have been impacted by intermediate processing stages can either be leftover or have a reliability score flag added to them to ease the interpretation. Furthermore, the approach has the potential to save unnecessary processing time and energy by accessing the information on the distribution of erroneous pixels ahead of the final step. The procedure had been evaluated using Sentinel-1 SLC datasets for different case areas, the Venus lagoon, Italy being one— and a remarkable result has been achieved.

In summary, some contributions of this thesis include:

- The formulation of QIs for SAR interferometric data. The QIs addressed a broader spectrum of datasets encompassing— measurement points, interferograms, images and images in a TS derived from the Sentinel-1 SLC dataset. QIs that are ”global” (for images and interferograms) and QIs that are very ”local”, i.e. very detailed: point by point and date by date within a time series were formulated based on residual information.

- By using the point score tool, quality of each measurement point is evaluated independently of the other points. By doing so, it was possible to identify reliable measurements from unreliable ones. This approach is useful in cases where the deformation signal is highly variable. The point score tool is also important to further exclude measurement points affected by PhU errors. While the point score defines whether a point is reliable or not, the TS score is responsible to indicate the exact date(s) of concern. To the knowledge of the author, the QIs are usually defined for ”points”: it is for the first time they are defined for each date of the PS time series.

- Processing framework to implement the QIs was proposed and validated. This particularly highlighted the contexts to incorporate QIs in small baseline methodologies and in the PSIG processing chain in particular.

- Tools to detect and identify erroneous measurements automatically from big interferometric SAR datasets were developed. InSAR data is often large and complex, and it can be challenging to identify errors and outliers manually as it is time-consuming and error-prone. Automated tools can help to quickly identify and correct erroneous measurements and remove them, if necessary, from the data— improving the reliability of the final results. With the increasing volume of such data, automated tools can boost processing and analyzing the data faster and more efficiently saving processing time and resources.

- An extended point selection strategy from QIs was proposed and validated. Once candidate measurement points were selected, further threshold-based filtering that makes use of the PhU errors was considered. This is important as it adds extra constraint on the reliability of selected points. The technique is also used to pick a reliable threshold for common point selection approaches. Augmenting commonly used pixel selection criteria with such quality indices is like certifying the points for further processing.

- Effect of PhU errors in displacement TS has been illustrated. PhU errors can cause inaccuracies in the calculated deformation values, leading to misinterpretation of results due to the resulting incorrect estimates of the amount and direction of surface deformation. This can be particularly problematic for areas with high deformation rates or complex deformation patterns. The influence of PhU errors on the displacement time series depends on the magnitude of the errors and the temporal and spatial correlation of the errors. Large PhU errors can lead to significant errors in displacement measurements. The QIs have played a role in alleviating PhU errors over-sighted by other mitigation strategies.
- The role of QIs in processing and analysis of MT-InSAR SLC Sentinel-1 data was justified. Attaching QIs to Sentinel-1 MT-InSAR products can help to communicate the level of confidence in the results to end-users and stakeholders. This can enable better decision-making in applications such as hazard mitigation and infrastructure monitoring.
- Publications of major findings were communicated in international conferences and indexed journals.

All the proposed approaches were illustrated using the Sentinel-1 SAR SLC dataset acquired from case areas with various land cover characteristics in the small baseline setting. Basically, the techniques implemented in the course of this dissertation also work for related data sources regardless of the resolution and frequency band the SAR sensor operates as far as sufficient network redundancy is guaranteed. Generally, the results suggested that proposed quality indicators could be used to augment existing point selection techniques by identifying reliable measurements from less reliable ones. The role has also immense advantages for data reduction and to build trust and assist in the interpretation of final products. Despite all the significant advancements in MT-InSAR methodologies, there are still critical challenges that need to be addressed in order to improve the accuracy and reliability of deformation measurements.

5.2 Future perspectives

In the course of this thesis development, the importance of a well-consolidated quality control framework for the space-borne MT-InSAR dataset, in general, is understood. On the other hand, the unprecedented recent and future SAR missions are imposing not only opportunities but also challenges to excel in processing, analysis and defining quality control strategies for big MT-InSAR data. Devising innovative quality control strategies that make use of opportunities to overcome existing limitations and challenges is also instrumental. Potential avenues for further research and investigation that have emerged from the current study include:

- Interferometric measurement point location uncertainty quantification. Experiments done thus far have witnessed that the location uncertainties of PSs as well as their values need to be quantified for a better interpretation of final results. The relative nature of the ”stable” reference point and the effect of the uncertain DEM errors are among the driving factors that require detailed analysis.
- Merging measurements from different but complementary data sources would also enrich measurements for better estimation of ground displacement InSAR products. Due to their potential contribution to limiting the opportunistic nature of interferometric measurement points, the focus on such topics might be rewarding. Preliminary

work on integrating MT-InSAR and GNSS products has been presented in Appendix A3. The goal has been to define a framework for a better TS estimation better than each of the techniques.

- A mechanism to determine an optimal threshold tuning strategy has been envisioned. This is particularly relevant to set context-driven and efficient thresholds for identifying unreliable measurements from big datasets.
- As the QIs proposed in this thesis are convenient only for datasets with redundant interferograms, the breadth, and depth of the tools need to be exploited further with uncertainty qualifications mechanisms included.

Overall, the thesis has demonstrated the use of QIs in identifying reliable measurements from big MT-InSAR datasets automatically. A particular emphasis has lied in limiting PhU errors and their impacts on the TS estimation. While this study has some limitations, such as the reliance on empirical thresholds for determining the classes of the quality scores and the need to widen the scope of the study to other MT-InSAR methods, it opens up new avenues for future research on the quality control and assurance of MT-InSAR data. The findings will have practical implications for geoscientists, engineers, and stakeholders who rely on reliable deformation measurements for geohazard assessment, infrastructure monitoring, and resource management.

REFERENCES

[1] R. F. Hanssen, *Radar interferometry: data interpretation and error analysis*. Springer Science & Business Media, 2001.

[2] A. C. Frery, A. Correa, C. D. Rennó, *et al.*, "Models for synthetic aperture radar image analysis," *Resenhas do Instituto de Matemática e Estatıstica da Universidade de São Paulo*, vol. 4, no. 1, pp. 45–77, 1999.

[3] A. Pepe, "Multi-temporal small baseline interferometric sar algorithms: Error budget and theoretical performance," *Remote Sensing*, vol. 13, no. 4, p. 557, 2021.

[4] A. Pepe and F. Calò, "A review of interferometric synthetic aperture radar (insar) multi-track approaches for the retrieval of earth's surface displacements," *Applied Sciences*, vol. 7, no. 12, p. 1264, 2017.

[5] W. Duan, H. Zhang, C. Wang, and Y. Tang, "Multi-temporal insar parallel processing for sentinel-1 large-scale surface deformation mapping," *Remote Sensing*, vol. 12, no. 22, p. 3749, 2020.

[6] A. L. Parker, *InSAR Observations of Ground Deformation: Application to the Cascades Volcanic Arc*. Springer, 2016.

[7] A. Hooper, “A multi-temporal insar method incorporating both persistent scatterer and small baseline approaches,” *Geophysical Research Letters*, vol. 35, no. 16, 2008.

[8] B. Zhang, R. Wang, Y. Deng, P. Ma, H. Lin, and J. Wang, “Mapping the yellow river delta land subsidence with multitemporal sar interferometry by exploiting both persistent and distributed scatterers,” *ISPRS Journal of Photogrammetry and Remote Sensing*, vol. 148, pp. 157–173, 2019.

[9] B. Ranjgar, S. V. Razavi-Termeh, F. Foroughnia, A. Sadeghi-Niaraki, and D. Perissin, “Land subsidence susceptibility mapping using persistent scatterer sar interferometry technique and optimized hybrid machine learning algorithms,” *Remote Sensing*, vol. 13, no. 7, p. 1326, 2021.

[10] D. Di Martire, R. Iglesias, D. Monells, *et al.*, “Comparison between differential sar interferometry and ground measurements data in the displacement monitoring of the earth-dam of conza della campania (italy),” *Remote sensing of environment*, vol. 148, pp. 58–69, 2014.

[11] Z. Yang, Z. Li, J. Zhu, Y. Wang, and L. Wu, “Use of sar/insar in mining deformation monitoring, parameter inversion, and forward predictions: A review,” *IEEE Geoscience and Remote Sensing Magazine*, vol. 8, no. 1, pp. 71–90, 2020.

[12] A. Ferretti, C. Prati, and F. Rocca, “Permanent scatterers in SAR interferometry,” *IEEE Transactions on geoscience and remote sensing*, vol. 39, no. 1, pp. 8–20, 2001.

[13] P. Berardino, G. Fornaro, R. Lanari, and E. Sansosti, “A new algorithm for surface deformation monitoring based on small baseline differential sar interferograms,” *IEEE Transactions on geoscience and remote sensing*, vol. 40, no. 11, pp. 2375–2383, 2002.

[14] N. Cao, H. Lee, and H. C. Jung, “Mathematical framework for phase-triangulation algorithms in distributed-scatterer interferometry,” *IEEE Geoscience and Remote Sensing Letters*, vol. 12, no. 9, pp. 1838–1842, 2015.

[15] O. Mora, J. J. Mallorqui, and A. Broquetas, “Linear and nonlinear terrain deformation maps from a reduced set of interferometric sar images,” *IEEE Transactions on Geoscience and Remote Sensing*, vol. 41, no. 10, pp. 2243–2253, 2003.

[16] R. Lanari, O. Mora, M. Manunta, J. J. Mallorquı, P. Berardino, and E. Sansosti, “A small-baseline approach for investigating deformations on full-resolution differential sar interferograms,” *IEEE transactions on geoscience and remote sensing*, vol. 42, no. 7, pp. 1377–1386, 2004.

[17] M. Crosetto, O. Monserrat, M. Cuevas-González, N. Devanthéry, and B. Crippa, “Persistent scatterer interferometry: A review,” *ISPRS Journal of Photogrammetry and Remote Sensing*, vol. 115, pp. 78–89, 2016.

[18] S. Li, S. Zhang, T. Li, Y. Gao, Q. Chen, and X. Zhang, “An adaptive phase optimization algorithm for distributed scatterer phase history retrieval,” *IEEE Journal of Selected Topics in Applied Earth Observations and Remote Sensing*, vol. 14, pp. 3914–3926, 2021.

[19] A. Ferretti, A. Fumagalli, F. Novali, C. Prati, F. Rocca, and A. Rucci, “A new algorithm for processing interferometric data-stacks: Squeesar,” *IEEE transactions on geoscience and remote sensing*, vol. 49, no. 9, pp. 3460–3470, 2011.

[20] D. HO TONG MINH, R. Hanssen, and F. Rocca, “Radar interferometry: 20 years of development in time series techniques and future perspectives,” *Remote Sensing*, vol. 12, no. 9, p. 1364, 2020.

[21] H. Ansari, F. De Zan, and R. Bamler, “Sequential estimator: Toward efficient insar time series analysis,” *IEEE Transactions on Geoscience and Remote Sensing*, vol. 55, no. 10, pp. 5637–5652, 2017.

[22] B. Wang, C. Zhao, Q. Zhang, Z. Lu, Z. Li, and Y. Liu, “Sequential estimation of dynamic deformation parameters for sbas-insar,” *IEEE Geoscience and Remote Sensing Letters*, vol. 17, no. 6, pp. 1017–1021, 2019.

[23] S. Samiei-Esfahany, J. E. Martins, F. Van Leijen, and R. F. Hanssen, “Phase estimation for distributed scatterers in insar stacks using integer least squares estimation,” *IEEE Transactions on Geoscience and Remote Sensing*, vol. 54, no. 10, pp. 5671–5687, 2016.

[24] A. Hooper, H. Zebker, P. Segall, and B. Kampes, “A new method for measuring deformation on volcanoes and other natural terrains using insar persistent scatterers,” *Geophysical research letters*, vol. 31, no. 23, 2004.

[25] B. M. Kampes and R. F. Hanssen, “Ambiguity resolution for permanent scatterer interferometry,” *IEEE Transactions on Geoscience and Remote Sensing*, vol. 42, no. 11, pp. 2446–2453, 2004.

[26] B. M. Kampes, *Radar interferometry*. Springer, 2006, vol. 12.

[27] F. van Leijen, “Persistent scatterer interferometry based on geodetic estimation theory,” Ph.D. dissertation, Delft University of Technology, 2014. DOI: `10.4233/uuid:5dba48d7-ee26-4449-b674-caa8df93e71e`.

[28] T. R. Lauknes, H. A. Zebker, and Y. Larsen, “Insar deformation time series using an $L\_\{1\}$-norm small-baseline approach,” *IEEE transactions on geoscience and remote sensing*, vol. 49, no. 1, pp. 536–546, 2010.

[29] A. Benoit, B. Pinel-Puysségur, R. Jolivet, and C. Lasserre, “Corphu: An algorithm based on phase closure for the correction of unwrapping errors in sar interferometry,” *Geophysical Journal International*, vol. 221, no. 3, pp. 1959–1970, 2020.

[30] A. Hooper and H. A. Zebker, “Phase unwrapping in three dimensions with application to insar time series,” *JOSA A*, vol. 24, no. 9, pp. 2737–2747, 2007.

[31] M. Costantini, F. Malvarosa, F. Minati, L. Pietranera, and G. Milillo, “A three-dimensional phase unwrapping algorithm for processing of multitemporal sar interferometric measurements,” in *IEEE International Geoscience and Remote Sensing Symposium*, IEEE, vol. 3, 2002, pp. 1741–1743.

[32] A. Pepe and R. Lanari, “On the extension of the minimum cost flow algorithm for phase unwrapping of multitemporal differential sar interferograms,” *IEEE Transactions on Geoscience and remote sensing*, vol. 44, no. 9, pp. 2374–2383, 2006.

[33] G. Fornaro, A. Pauciullo, and D. Reale, “A null-space method for the phase unwrapping of multitemporal sar interferometric stacks,” *IEEE transactions on geoscience and remote sensing*, vol. 49, no. 6, pp. 2323–2334, 2011.

[34] K. Itoh, “Analysis of the phase unwrapping algorithm,” *Applied optics*, vol. 21, no. 14, pp. 2470–2470, 1982.

[35] F. J. Van Leijen, “Persistent scatterer interferometry based on geodetic estimation theory,” 2014.

[36] R. Hanssen, F. Van Leijen, G. Van Zwieten, C. Bremmer, S. Dortland, and M. Kleuskens, “Validation of existing processing chains in terrafirma stage 2, Product validation: Validation in the amsterdam and alkmaar area. terrafirma project report.,” Delft University of Technology: Delft, The Netherlands, Tech. Rep., 2008.

[37] M. Costantini, A. Farina, and F. Zirilli, “A fast phase unwrapping algorithm for sar interferometry,” *IEEE Transactions on Geoscience and Remote Sensing*, vol. 37, no. 1, pp. 452–460, 1999.

[38] S. Marano, F. Palmieri, and G. Franceschetti, “Discrete green’s methods and their application to two-dimensional phase unwrapping,” *JOSA A*, vol. 19, no. 7, pp. 1319–1333, 2002.

[39] Z. Yunjun, H. Fattahi, and F. Amelung, “Small baseline insar time series analysis: Unwrapping error correction and noise reduction,” *Computers & Geosciences*, vol. 133, p. 104 331, 2019.

[40] J. O. Ogundare, *Understanding least squares estimation and geomatics data analysis*. John Wiley & Sons, 2019.

[41] ESA–European Space Agency, *eoPortal directory - satellite missions database*, Last accessed on 13 August 2022, 2022. [Online]. Available: `https://directory.eoportal.org/web/eoportal/satellite-missions`.

[42] F. De Zan and A. M. Guarnieri, “Topsar: Terrain observation by progressive scans,” *IEEE Transactions on Geoscience and Remote Sensing*, vol. 44, no. 9, pp. 2352–2360, 2006.

[43] M. Manunta, C. De Luca, I. Zinno, *et al.*, “The parallel sbas approach for sentinel-1 interferometric wide swath deformation time-series generation: Algorithm description and products quality assessment,” *IEEE Transactions on Geoscience and Remote Sensing*, vol. 57, no. 9, pp. 6259–6281, 2019.

[44] N. Devanthéry, M. Crosetto, O. Monserrat, M. Cuevas-González, and B. Crippa, “An approach to persistent scatterer interferometry,” *Remote sensing*, vol. 6, no. 7, pp. 6662–6679, 2014.

[45] R. Gens and J. L. Van Genderen, “Review article sar interferometry—issues, techniques, applications,” *International journal of remote sensing*, vol. 17, no. 10, pp. 1803–1835, 1996.

[46] M. A. Richards, J. Scheer, W. A. Holm, and W. L. Melvin, *Principles of modern radar*. Citeseer, 2010, vol. 1.

[47] H. Maıtre, *Processing of synthetic aperture radar (SAR) images*. John Wiley & Sons, 2013.

[48] Y. K. Chan and V. Koo, “An introduction to synthetic aperture radar (sar),” *Progress In Electromagnetics Research B*, vol. 2, pp. 27–60, 2008.

[49] G. Franceschetti and R. Lanari, *Synthetic aperture radar processing*. CRC press, 1999.

[50] H. Cruz, M. Véstias, J. Monteiro, H. Neto, and R. P. Duarte, “A review of synthetic-aperture radar image formation algorithms and implementations: A computational perspective,” *Remote Sensing*, vol. 14, no. 5, p. 1258, 2022.

[51] F. Berizzi, M. Martorella, and E. Giusti, *Radar imaging for maritime observation*. CRC Press, 2018.

[52] J. C. Curlander and R. N. McDonough, *Synthetic aperture radar*. Wiley, New York, 1991, vol. 11.

[53] S. Samiei Esfahany, “Exploitation of distributed scatterers in synthetic aperture radar interferometry,” Ph.D. dissertation, Delft University of Technology, 2017.

[54] R. Bamler, “Principles of synthetic aperture radar,” *Surveys in Geophysics*, vol. 21, no. 2, pp. 147–157, 2000.

[55] H. A. Zebker and R. M. Goldstein, “Topographic mapping from interferometric synthetic aperture radar observations,” *Journal of Geophysical Research: Solid Earth*, vol. 91, no. B5, pp. 4993–4999, 1986.

[56] P. A. Rosen, S. Hensley, H. A. Zebker, F. H. Webb, and E. J. Fielding, “Surface deformation and coherence measurements of kilauea volcano, hawaii, from sir-c radar interferometry,” *Journal of Geophysical Research: Planets*, vol. 101, no. E10, pp. 23 109–23 125, 1996.

[57] M. Eineder, C. Minet, P. Steigenberger, X. Cong, and T. Fritz, “Imaging geodesy—toward centimeter-level ranging accuracy with terrasar-x,” *IEEE Transactions on Geoscience and Remote Sensing*, vol. 49, no. 2, pp. 661–671, 2010.

[58] R. Bamler and P. Hartl, “Synthetic aperture radar interferometry,” *Inverse problems*, vol. 14, no. 4, R1, 1998.

[59] V. Macchiarulo, P. Milillo, C. Blenkinsopp, C. Reale, and G. Giardina, “Multi-temporal insar for transport infrastructure monitoring: Recent trends and challenges,” in *Proceedings of the Institution of Civil Engineers-Bridge Engineering*, Thomas Telford Ltd, 2022, pp. 1–26.

[60] A. Moreira, P. Prats-Iraola, M. Younis, G. Krieger, I. Hajnsek, and K. P. Papathanassiou, “A tutorial on synthetic aperture radar,” *IEEE Geoscience and remote sensing magazine*, vol. 1, no. 1, pp. 6–43, 2013.

[61] F. Raspini, F. Caleca, M. Del Soldato, D. Festa, P. Confuorto, and S. Bianchini, “Review of satellite radar interferometry for subsidence analysis,” *Earth-Science Reviews*, p. 104 239, 2022.

[62] A. I. Flores-Anderson, K. E. Herndon, R. B. Thapa, and E. Cherrington, “The sar handbook: Comprehensive methodologies for forest monitoring and biomass estimation,” Tech. Rep., 2019.

[63] A. K. Gabriel, R. M. Goldstein, and H. A. Zebker, “Mapping small elevation changes over large areas: Differential radar interferometry,” *Journal of Geophysical Research: Solid Earth*, vol. 94, no. B7, pp. 9183–9191, 1989.

[64] P. Shanker and H. Zebker, “Persistent scatterer selection using maximum likelihood estimation,” *Geophysical Research Letters*, vol. 34, no. 22, 2007.

[65] C. Zhao, Z. Li, P. Zhang, B. Tian, and S. Gao, “Improved maximum likelihood estimation for optimal phase history retrieval of distributed scatterers in insar stacks,” *IEEE Access*, vol. 7, pp. 186 319–186 327, 2019.

[66] A. Hooper, P. Segall, and H. Zebker, “Persistent scatterer interferometric synthetic aperture radar for crustal deformation analysis, with application to volcán alcedo, galápagos,” *Journal of Geophysical Research: Solid Earth*, vol. 112, no. B7, 2007.

[67] R. Touzi, A. Lopes, J. Bruniquel, and P. W. Vachon, “Coherence estimation for sar imagery,” *IEEE transactions on geoscience and remote sensing*, vol. 37, no. 1, pp. 135–149, 1999.

[68] O. Monserrat, “Deformation measurement and monitoring with GB-SAR,” Ph.D. dissertation, Polytechnic University of Catalonia Barcelona, Spain, 2012.

[69] D. A. Schmidt and R. Bürgmann, “Time-dependent land uplift and subsidence in the santa clara valley, california, from a large interferometric synthetic aperture radar data set,” *Journal of Geophysical Research: Solid Earth*, vol. 108, no. B9, 2003.

[70] M. Crosetto, B. Crippa, and E. Biescas, “Early detection and in-depth analysis of deformation phenomena by radar interferometry,” *Engineering Geology*, vol. 79, no. 1-2, pp. 81–91, 2005.

[71] N. Cao, H. Lee, and H. C. Jung, “A phase-decomposition-based psinsar processing method,” *IEEE Transactions on Geoscience and Remote Sensing*, vol. 54, no. 2, pp. 1074–1090, 2015.

[72] K. Goel and N. Adam, “A distributed scatterer interferometry approach for precision monitoring of known surface deformation phenomena,” *IEEE Transactions on Geoscience and Remote Sensing*, vol. 52, no. 9, pp. 5454–5468, 2013.

[73] R. Lanari, F. Casu, M. Manzo, *et al.*, “An overview of the small baseline subset algorithm: A dinsar technique for surface deformation analysis,” *Deformation and Gravity Change: Indicators of Isostasy, Tectonics, Volcanism, and Climate Change*, pp. 637–661, 2007.

[74] R. M. Goldstein, H. A. Zebker, and C. L. Werner, “Satellite radar interferometry: Two-dimensional phase unwrapping,” *Radio science*, vol. 23, no. 4, pp. 713–720, 1988.

[75] A. González and L. Jacques, “Robust phase unwrapping by convex optimization,” in *2014 IEEE International Conference on Image Processing (ICIP)*, IEEE, 2014, pp. 1713–1717.

[76] A. Pepe, L. D. Euillades, M. Manunta, and R. Lanari, “New advances of the extended minimum cost flow phase unwrapping algorithm for sbas-dinsar analysis at full spatial resolution,” *IEEE transactions on geoscience and remote sensing*, vol. 49, no. 10, pp. 4062–4079, 2011.

[77] D. C. Ghiglia and M. D. Pritt, “Two-dimensional phase unwrapping: Theory, algorithms, and software,” *Wiely-Interscience, first ed.(April 1998)*, 1998.

[78] R. Bamler, N. Adam, G. W. Davidson, and D. Just, “Noise-induced slope distortion in 2-d phase unwrapping by linear estimators with application to sar interferometry,” *IEEE Transactions on Geoscience and Remote Sensing*, vol. 36, no. 3, pp. 913–921, 1998.

[79] M. C. Cuenca, A. J. Hooper, and R. F. Hanssen, “A new method for temporal phase unwrapping of persistent scatterers insar time series,” *IEEE transactions on geoscience and remote sensing*, vol. 49, no. 11, pp. 4606–4615, 2011.

[80] M. Costantini, “A novel phase unwrapping method based on network programming,” *IEEE Transactions on geoscience and remote sensing*, vol. 36, no. 3, pp. 813–821, 1998.

[81] X. Chen, Z. Wen, and Q. Wu, “Residue classification-based robust phase unwrapping in high-noise region,” *Journal of Sensors*, vol. 2022, 2022.

[82] R. Marhamati and M. A. Masnadi-Shirazi, “The principles of proper placement of branch cut in phase unwrapping using combined and extended methods based on residue searching,” *Signal, Image and Video Processing*, vol. 14, pp. 593–600, 2020.

[83] M. D. Pritt and J. S. Shipman, “Least-squares two-dimensional phase unwrapping using fft’s,” *IEEE Transactions on geoscience and remote sensing*, vol. 32, no. 3, pp. 706–708, 1994.

[84] H. Takajo and T. Takahashi, “Noniterative method for obtaining the exact solution for the normal equation in least-squares phase estimation from the phase difference,” *JOSA A*, vol. 5, no. 11, pp. 1818–1827, 1988.

[85] R. Gens, “Quality assessment of sar interferometric data,” 1998.

[86] G. Fornaro and E. Sansosti, “A two-dimensional region growing least squares phase unwrapping algorithm for interferometric sar processing,” *IEEE transactions on geoscience and remote sensing*, vol. 37, no. 5, pp. 2215–2226, 1999.

[87] Y. Guo, X. Chen, and T. Zhang, “Robust phase unwrapping algorithm based on least squares,” *Optics and Lasers in Engineering*, vol. 63, pp. 25–29, 2014.

[88] H. A. Zebker and Y. Lu, “Phase unwrapping algorithms for radar interferometry: Residue-cut, least-squares, and synthesis algorithms,” *JOSA A*, vol. 15, no. 3, pp. 586–598, 1998.

[89] J. M. Huntley, “Three-dimensional noise-immune phase unwrapping algorithm,” *Applied Optics*, vol. 40, no. 23, pp. 3901–3908, 2001.

[90] F. Liu and B. Pan, “A new 3-d minimum cost flow phase unwrapping algorithm based on closure phase,” *IEEE Transactions on Geoscience and Remote Sensing*, vol. 58, no. 3, pp. 1857–1867, 2019.

[91] P. S. Mahapatra, S. Samiei-Esfahany, and R. F. Hanssen, “Geodetic network design for insar,” *IEEE Transactions on Geoscience and Remote Sensing*, vol. 53, no. 7, pp. 3669–3680, 2015.

[92] S. Williams, Y. Bock, and P. Fang, “Integrated satellite interferometry: Tropospheric noise, gps estimates and implications for interferometric synthetic aperture radar

products," *Journal of Geophysical Research: Solid Earth*, vol. 103, no. B11, pp. 27 051–27 067, 1998.

[93] G. Wadge, P. Webley, I. James, *et al.*, "Atmospheric models, gps and insar measurements of the tropospheric water vapour field over mount etna," *Geophysical Research Letters*, vol. 29, no. 19, pp. 11–1, 2002.

[94] X.-l. Ding, Z.-w. Li, J.-j. Zhu, G.-c. Feng, and J.-p. Long, "Atmospheric effects on insar measurements and their mitigation," *Sensors*, vol. 8, no. 9, pp. 5426–5448, 2008.

[95] H. Berrada Baby, P. Gole, and J. Lavergnat, "A model for the tropospheric excess path length of radio waves from surface meteorological measurements," *Radio science*, vol. 23, no. 6, pp. 1023–1038, 1988.

[96] H. A. Zebker, P. A. Rosen, and S. Hensley, "Atmospheric effects in interferometric synthetic aperture radar surface deformation and topographic maps," *Journal of geophysical research: solid earth*, vol. 102, no. B4, pp. 7547–7563, 1997.

[97] C. Yu, Z. Li, and N. T. Penna, "Interferometric synthetic aperture radar atmospheric correction using a gps-based iterative tropospheric decomposition model," *Remote Sensing of Environment*, vol. 204, pp. 109–121, 2018.

[98] X. Cong, U. Balss, F. Rodriguez Gonzalez, and M. Eineder, "Mitigation of tropospheric delay in sar and insar using nwp data: Its validation and application examples," *Remote Sensing*, vol. 10, no. 10, p. 1515, 2018.

[99] Y. Chen, Z. Li, L. Bai, J.-P. Muller, J. Zhang, and Q. Zeng, "Successful applications of generic atmospheric correction online service for insar (gacos) to the reduction of atmospheric effects on insar observations," *Journal of Geodesy and Geoinformation Science*, vol. 4, no. 1, p. 109, 2021.

[100] C. Yu, Z. Li, N. T. Penna, and P. Crippa, “Generic atmospheric correction model for interferometric synthetic aperture radar observations,” *Journal of Geophysical Research: Solid Earth*, vol. 123, no. 10, pp. 9202–9222, 2018.

[101] Q. Wang, W. Yu, B. Xu, and G. Wei, “Assessing the use of gacos products for sbas-insar deformation monitoring: A case in southern california,” *Sensors*, vol. 19, no. 18, p. 3894, 2019.

[102] S. Liu, “Satellite radar interferometry: estimation of atmospheric delay,” Ph.D. dissertation, Delft University of Technology, 2012.

[103] P. K. Kirui, E. Reinosch, N. Isya, B. Riedel, and M. Gerke, “Mitigation of atmospheric artefacts in multi-temporal insar: A review,” *PFG–Journal of Photogrammetry, Remote Sensing and Geoinformation Science*, vol. 89, no. 3, pp. 251–272, 2021.

[104] H. Ansari, F. De Zan, and A. Parizzi, “Study of systematic bias in measuring surface deformation with sar interferometry,” *IEEE Transactions on Geoscience and Remote Sensing*, vol. 59, no. 2, pp. 1285–1301, 2020.

[105] H. A. Zebker, J. Villasenor, *et al.*, “Decorrelation in interferometric radar echoes,” *IEEE Transactions on geoscience and remote sensing*, vol. 30, no. 5, pp. 950–959, 1992.

[106] R. I. González, J. J. M. Franquet, and X. F. Cànovas, “High-resolution space-borne and ground-based sar persistent scatterer interferometry for landslide monitoring,” Ph.D. dissertation, Universitat Politècnica de Catalunya, 2016.

[107] O. Monserrat, M. Crosetto, M. Cuevas, and B. Crippa, “The thermal expansion component of persistent scatterer interferometry observations,” *IEEE Geoscience and Remote Sensing Letters*, vol. 8, no. 5, pp. 864–868, 2011.

[108] P. Agram and M. Simons, “A noise model for insar time series,” *Journal of Geophysical Research: Solid Earth*, vol. 120, no. 4, pp. 2752–2771, 2015.

[109] H. Ansari, “Efficient high-precision time series analysis for synthetic aperture radar interferometry,” Ph.D. dissertation, 2019.

[110] R. J. Michaelides, H. A. Zebker, and Y. Zheng, “An algorithm for estimating and correcting decorrelation phase from insar data using closure phase triplets,” *IEEE Transactions on Geoscience and Remote Sensing*, vol. 57, no. 12, pp. 10 390–10 397, 2019.

[111] J. Biggs, T. Wright, Z. Lu, and B. Parsons, “Multi-interferogram method for measuring interseismic deformation: Denali fault, alaska,” *Geophysical Journal International*, vol. 170, no. 3, pp. 1165–1179, 2007.

[112] F. De Zan, M. Zonno, and P. Lopez-Dekker, “Phase inconsistencies and multiple scattering in sar interferometry,” *IEEE Transactions on Geoscience and Remote Sensing*, vol. 53, no. 12, pp. 6608–6616, 2015.

[113] R. Scheiber and A. Moreira, “Coregistration of interferometric sar images using spectral diversity,” *IEEE Transactions on Geoscience and Remote Sensing*, vol. 38, no. 5, pp. 2179–2191, 2000.

[114] E. Sansosti, P. Berardino, M. Manunta, F. Serafino, and G. Fornaro, “Geometrical sar image registration,” *IEEE Transactions on Geoscience and Remote Sensing*, vol. 44, no. 10, pp. 2861–2870, 2006.

[115] N. Yagüe-Martınez, P. Prats-Iraola, F. R. Gonzalez, *et al.*, “Interferometric processing of sentinel-1 tops data,” *IEEE Transactions on Geoscience and Remote Sensing*, vol. 54, no. 4, pp. 2220–2234, 2016.

[116] N. Yague-Martinez, F. De Zan, and P. Prats-Iraola, “Coregistration of interferometric stacks of sentinel-1 tops data,” *IEEE Geoscience and Remote Sensing Letters*, vol. 14, no. 7, pp. 1002–1006, 2017.

[117] R. Palamà, M. Crosetto, O. Monserrat, *et al.*, “Filtering of the atmospheric phase screen in insar data using the nonequispaced fast fourier transform,” in *2021 IEEE International Geoscience and Remote Sensing Symposium IGARSS*, IEEE, 2021, pp. 3979–3982.

[118] M. Crosetto, O. Monserrat, M. Cuevas, and B. Crippa, “Spaceborne differential sar interferometry: Data analysis tools for deformation measurement,” *Remote Sensing*, vol. 3, no. 2, pp. 305–318, 2011.

[119] E. Biescas, M. Crosetto, M. Agudo, O. Monserrat, and B. Crippa, “Two radar interferometric approaches to monitor slow and fast land deformation,” *Journal of Surveying Engineering*, vol. 133, no. 2, pp. 66–71, 2007.

[120] W. Baarda, “A testing procedijre for use in geodetic networks,” *Pub. on Geod., New Series*, vol. 2, no. 5, 1968.

[121] Å. Björck, *Numerical methods for least squares problems*. SIAM, 1996.

[122] J. Tribolet, “A new phase unwrapping algorithm,” *IEEE Transactions on Acoustics, Speech, and Signal Processing*, vol. 25, no. 2, pp. 170–177, 1977.

[123] M. Costantini, “A phase unwrapping method based on network programming,” in *ERS SAR Interferometry*, vol. 406, 1997, p. 261.

[124] C. Esch, J. Köhler, K. Gutjahr, and W.-D. Schuh, “On the analysis of the phase unwrapping process in a d-insar stack with special focus on the estimation of a motion model,” *Remote Sensing*, vol. 11, no. 19, p. 2295, 2019.

[125] O. Monserrat, M. Crosetto, R. Iglesias, G. Rossi, L. Calcagni, and B. Crippa, “A tool for 2+ 1d phase unwrapping: Application examples,” in *Proc. Fringe 2009 Workshop*, 2009.

[126] S. Montazeri, F. Rodrıguez González, and X. X. Zhu, “Geocoding error correction for insar point clouds,” *Remote Sensing*, vol. 10, no. 10, p. 1523, 2018.

[127] K. Zhang, Z. Li, G. Meng, and Y. Dai, “A very fast phase inversion approach for small baseline style interferogram stacks,” *ISPRS journal of photogrammetry and remote sensing*, vol. 97, pp. 1–8, 2014.

[128] G. H. Golub and C. F. Van Loan, *Matrix computations*. JHU press, 2013.

[129] A. R. Amiri-Simkooei, J. Asgari, F. Zangeneh-Nejad, and S. Zaminpardaz, “Basic concepts of optimization and design of geodetic networks,” *Journal of Surveying Engineering*, vol. 138, no. 4, pp. 172–183, 2012.

[130] N. Sneeuw, F. Krumm, and M. Roth, “Adjustment theory,” *University Stuttgart: Stuttgart, Germany*, 2008.

[131] F. Van Leijen, V. Ketelaar, P. Marinkovic, and R. Hanssen, “Persistent scatterer interferometry: Precision, reliability and integration,” in *Proceedings of ISPRS Hannover Workshop*, 2005.

APPENDICES

A1 List of Publications

Below the list of conference and journal papers published during the development of this thesis are presented.

Journal Papers

1 **Y. Wassie**, S. M. Mirmazloumi, M. Crosetto, R. Palamà, O. Monserrat, and B. Crippa, “Spatio-temporal quality indicators for differential interferometric synthetic aperture radar data,” Remote Sensing, vol. 14, no. 3, p. 798, 2022.

2 S. M. Mirmazloumi, **Y. Wassie**, J. A. Navarro, R. Palamà, V. Krishnakumar, A. Barra, M. Cuevas-González, M. Crosetto, and O. Monserrat, “Classification of ground deformation using sentinel-1 persistent scatterer interferometry time series,” GIScience Remote Sensing, vol. 59, no. 1, pp. 374–392, 2022.

3 S. M. Mirmazloumi, A. F. Gambin, R. Palamà, M.Crosetto, **Y. Wassie**, J.A.Navarro, A. Barra, and O. Monserrat, “Supervised machine learning algorithms for ground motion time series classification from InSAR data,” Remote Sensing, vol. 14, no. 15, p. 3821, 2022.

4 InSAR Time Series and LSTM model to Support Early Warning Detection Tools of Ground Instabilities: mining sites case studies, Bulletin of Engineering Geology and the Environment. (Submitted!).

Conference Papers

1 **Y. Wassie**, S.M. Mohammad Mirmazloumi, O. Monserrat, B. Crippa, R. Palamà, A. Barra, M. Crosetto, "Interferometric SAR deformation time-series: A quality index," in Microwave Remote Sensing: Data Processing and Applications, SPIE, vol. 11861, 2021, pp. 19–27.

2 **Y. Wassie**, Q. Gao, O. Monserrat, A. Barra, B. Crippa, and M. Crosetto, "Differential SAR interferometry for the monitoring of land subsidence along railway infrastructures," The International Archives of Photogrammetry, Remote Sensing and Spatial Information Sciences, vol. 43, pp. 361–366, 2022.

3 **Y. Wassie**, M. Crosetto, G. Luzi, O. Monserrat, A. Barra, R. Palamá, M. Cuevas-González, S.M. Mirmazloumi, P. Espín-López, B. Crippa, "Active reflectors for interferometric SAR deformation measurement," in Imaging Today, Foreseeing Tomorrow, Commission III: ISPRS Congress, Copernicus Publishing, vol. 43, 2021, pp. 177–182.

4 S. M. Mirmazloumi, **Y. Wassie**, J. A. Navarro, R. Palamà, M. Crosetto, and O. Monserrat, "Ground movement classification using statistical tests over persistent scatterer interferometry time series," Procedia Computer Science, vol. 196, pp. 21–26, 2022.

5 M. Crosetto, L. Solari, A. Barra, O. Monserrat, M. Cuevas-González, R. Palamà, **Y. Wassie**, S. Shahbazi, S. M. Mirmazloumi, B. Crippa, and M. Mróz, "Analysis of the products of the Copernicus ground motion service," International Archives of the Photogrammetry, Remote Sensing and Spatial Information Sciences, vol. 43, pp. 257–262, 2022.

6 S. M. Mirmazloumi, Á. F. Gambin, **Y. Wassie**, A. Barra, R. Palamà, M. Crosetto, O. Monserrat, and B. Crippa, “Insar deformation time series classification using a convolutional neural network,” The International Archives of Photogrammetry, Remote Sensing and Spatial Information Sciences, vol. 43, pp. 307–312, 2022.

7 M. Crosetto, G. Luzi, O. Monserrat, A. Barra, M. Cuevas-González, R. Palamá, V. Krishnakumar, **Y. Wassie**, S. M. Mirmazloumi, P. Espín-López, and B. Crippa, “Deformation monitoring using SAR interferometry and active and passive reflectors,” in ISPRS Congress. Commission III, Copernicus, vol. 43, 2020, pp. 287–292.

A2 Experimental results on the effect of PhU errors

The following are sample plots of an experiment on visualizing and deepening understanding of the effects of PhU error jumps in TS of phase estimation.

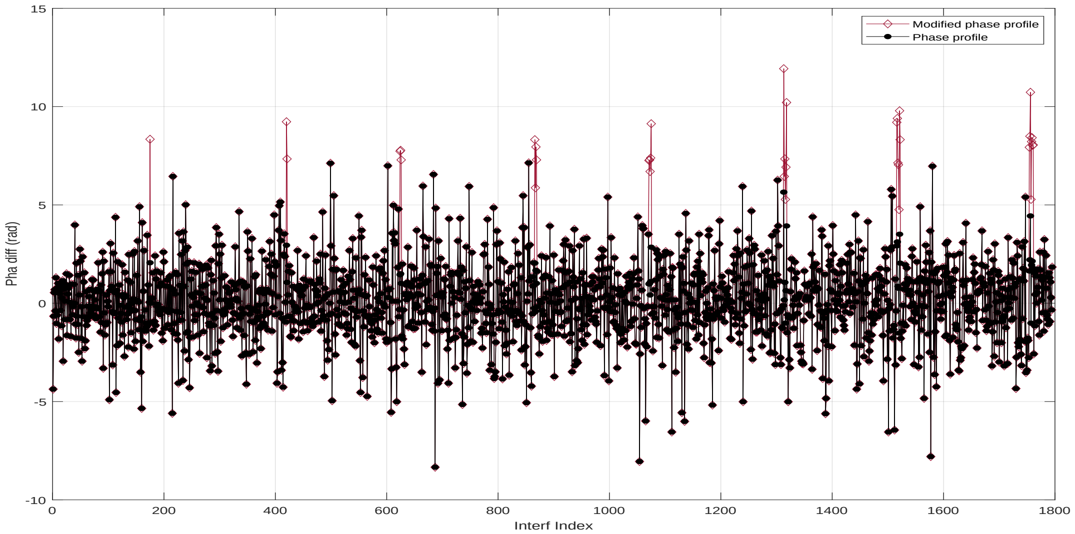

(a) Phase profile of a point over 1795 interferograms. Estimated unwrapped phases computed from the PSIG processing chain are indicated in the black curve and the one in the red curve is obtained by introducing PhU error to selected interferograms shown in red diamonds.

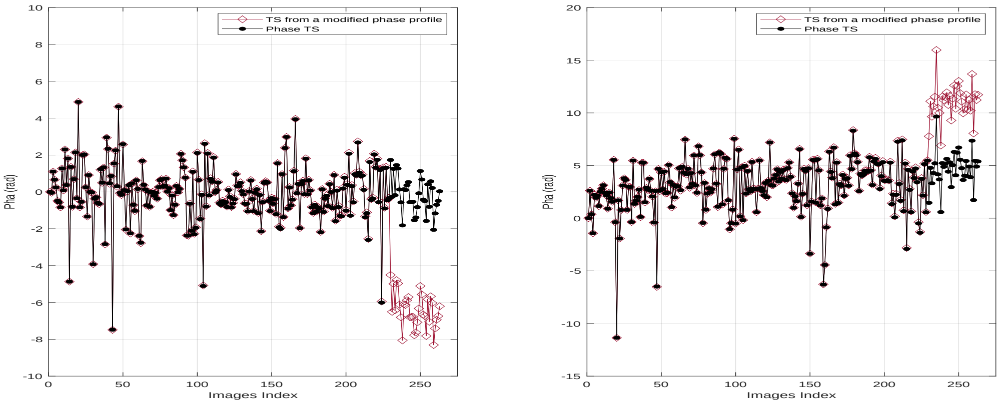

(b) Examples justifying effects of PhU errors at interferograms on the TS of estimated phases. Plots on the left and right correspond to the phase evolution of two different sample points over the 263 images.

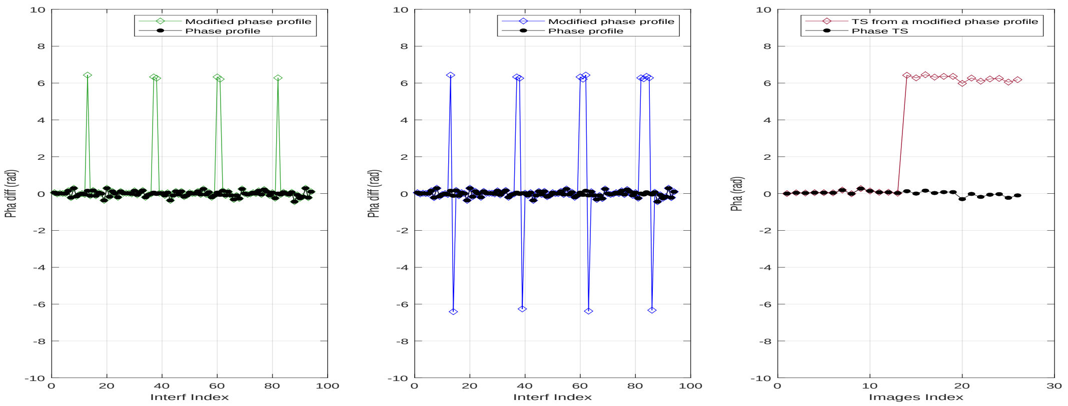

(c) Phase profile over the interferograms (the green curve) obtained by modifying only master images of the profile (the black curve) shown in the left plot). The middle plot represents similar information as in the left plot but for a different point. The blue curve indicates the modification of master and co-master images of selected interferograms. The plot on the right is the phase TS before (the black curve) and after modifying (the red curve) the phase profiles of a point in the interferograms. In these plots, 26 images and 94 interferograms were processed.

Figure A2.1: Plots of an experiment to visualize effects of PhU 2π jump on the estimated phase TS. It is good to note that a 2π jump in the profile of phases at the sequence of interferograms doesn't always appear to correspond to a 2π jump in the TS of phases.

A3 Data Integration and plots from Venice GPS measurements

Combining multiple InSAR datasets from different acquisition times or datasets from different sensors is supposed to provide a more comprehensive understanding of deformation processes and has the advantage to improve the accuracy and reliability of deformation monitoring. Multi-sensor measurements can be integrated to improve the spatial resolution and accuracy of deformation measurements mainly for areas with complex topography. MT-InSAR data can also be integrated with various auxiliary data, numerical weather models, terrestrial geodetic tools and corner reflectors. This can provide additional constraints on deformation processes and improve measurement accuracy. On the other hand, the data integration process demands specialized expertise in the field, as well as a deep understanding of the underlying physical processes. It also requires careful consideration of factors such as data quality, spatial and temporal coverage, and the suitability of different analysis techniques for the specific application. Unfortunately, no common framework addressing the required depth have been traced thus far.

A3.1 Integration of InSAR and GNSS measurements-GPSI

The integration of InSAR and GNSS measurements can provide complementary information and improve the accuracy and resolution of deformation monitoring. Both temporal and spatial variations in the atmosphere during satellite SAR measurement acquisitions typically produce artifacts, which are a common source of inaccuracies. The accuracy of GNSS measurements, on the other hand, is high though at sparsely distributed points. This makes them among the feasible options for the validation of MT-InSAR measurements. Apart from the accuracy, getting a high density of such measurements is costly, labor intensive, and difficult and/or impossible in some hazardous or human-unreachable areas— which are not as such issues for SAR measurements.

It is also good to note that deformation estimations of GNSS and MT-InSAR measurements are not directly comparable. While GNSS measurements provide absolute 3D velocities with respect to a regional or global geodetic reference system, deformation estimates of InSAR measurement direction are calculated in the LOS direction relative to a reference point taken from a scene and chosen during the PSI processing. In many cases, information about the height and stability of the reference point is not known prior to the processing but obtained from DEM— which may not be accurate in itself. Thereby, lead to misinterpretations of the deformation information that could result from inaccurate geocoding. In order to manage labor, cost, coverage and accuracy issues, GNSS and Interferometric measurements need to get advantages of each other.

In line with this, Figure A3.2 indicate plots of a preliminary assessment of an ongoing experiment that has been conducted to integrate measurements from GPS stations and PSI measurements from the Venice lagoon, Italy.

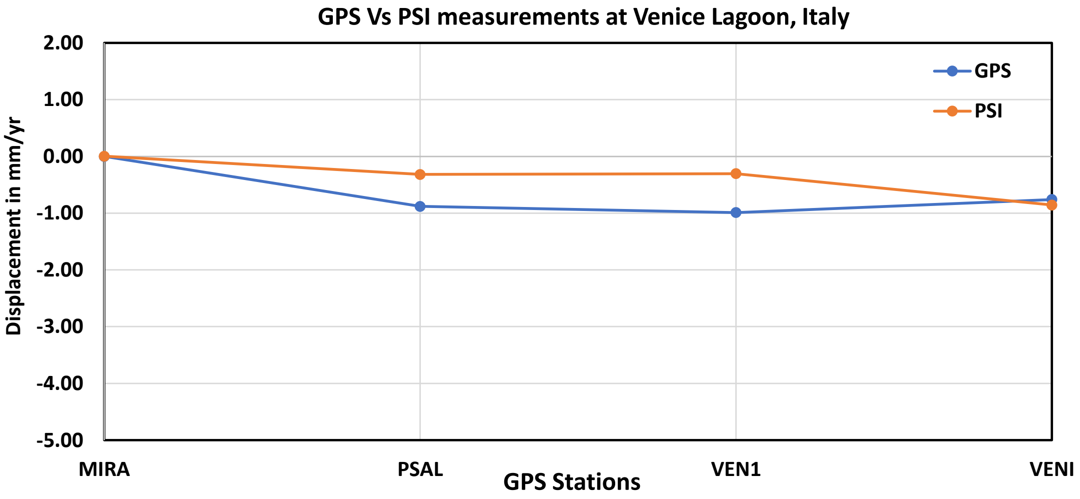

Figure A3.2: GPSI experiment—Comparison of GPS and PSI measurements at/around GPS stations in Venice lagoon.

For comparison purposes, average values of PSs located within a circle of radius 50m were considered. A better agreement between GPS and InSAR measurements is recorded at CGIA and VENI stations compared to VEN1 and PSAL. The maximum absolute difference of the measurements is close to 2 mm per year. Corresponding displacements at these GPS stations from year 2015 to 2020 are plotted in Figure A3.3 for further reference. Developing a standard approach that will minimize such effects is an important aspect to be addressed in the future.

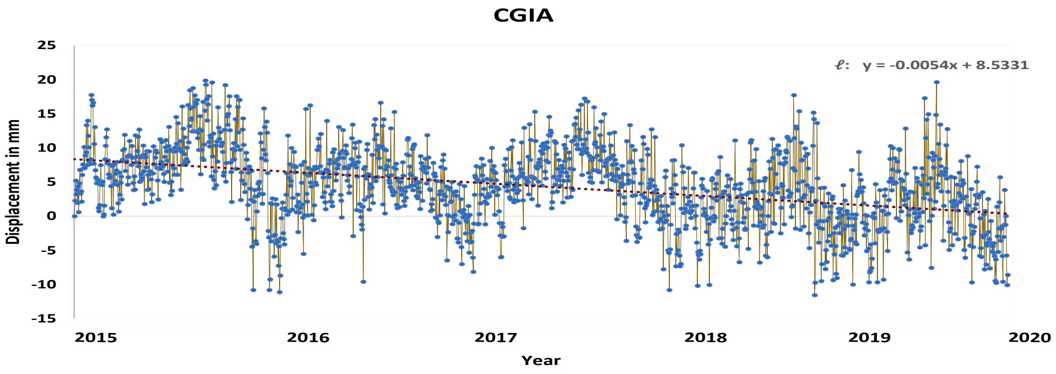

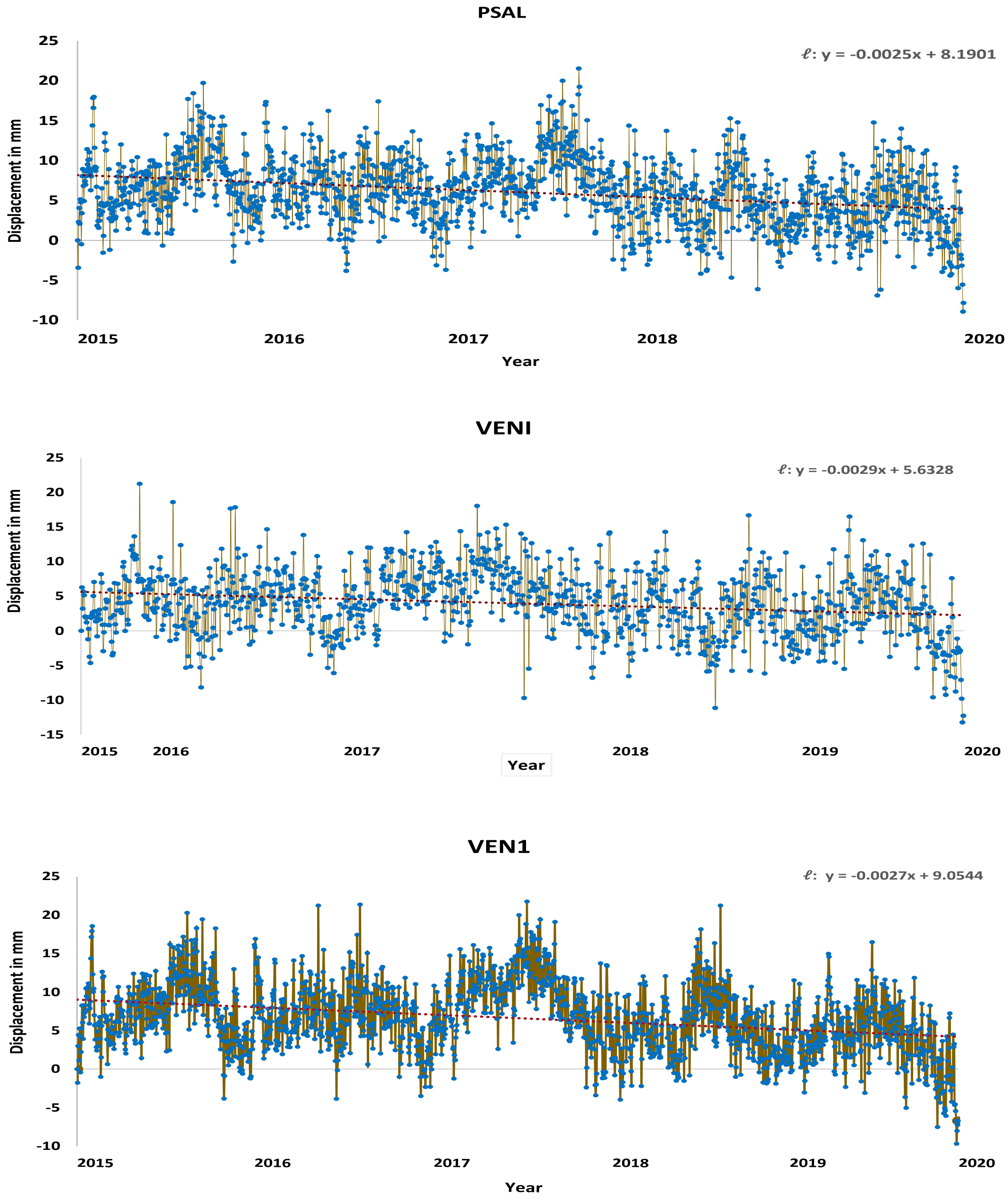

Figure A3.3: Plots of the vertical components of measurements from four GPS stations in the Venice lagoon, Italy

A4 Sentinel-1 Satellite single look complex datasets metadata

Table A4.1: C-SAR sensor Sentinel-1 processed images with IW beam mode from track 95 from Venice, Italy case area.

Platform	Orbit	Frame	Acq.@ Date & time	NS(Lat,Lon)	FS(Lat,Lon)	NE(Lat,Lon)	FE(Lat,Lon)	Size(MB)	R
Sentinel-1B	21646	440	2020-05-19T05:18:47	46.30, 14.33	46.70, 10.98	44.63, 13.86	45.03, 10.61	4543.30	7
Sentinel-1A	32542	440	2020-05-13T05:19:29	46.25, 14.30	46.65, 10.97	44.63, 13.85	45.03, 10.61	4422.06	7
Sentinel-1B	21471	440	2020-05-07T05:18:48	46.24, 14.31	46.64, 11.00	44.57, 13.84	44.97, 10.63	4413.37	8
Sentinel-1A	32367	440	2020-05-01T05:19:28	46.25, 14.30	46.65, 10.97	44.63, 13.85	45.03, 10.61	4427.31	9
Sentinel-1B	21296	440	2020-04-25T05:18:47	46.24, 14.31	46.64, 11.00	44.57, 13.84	44.97, 10.63	4438.60	10
Sentinel-1B	21121	443	2020-04-13T05:19:03	45.25, 14.05	45.65, 10.79	43.57, 13.58	43.97, 10.43	4272.19	11
Sentinel-1B	21121	438	2020-04-13T05:18:37	46.74, 14.44	47.14, 11.11	45.13, 13.98	45.52, 10.75	4432.92	11
Sentinel-1A	32017	440	2020-04-07T05:19:27	46.25, 14.30	46.65, 10.96	44.63, 13.84	45.03, 10.61	4342.56	12
Sentinel-1B	20946	443	2020-04-01T05:19:03	45.25, 14.05	45.65, 10.79	43.58, 13.58	43.97, 10.42	4373.92	13
Sentinel-1B	20946	438	2020-04-01T05:18:37	46.74, 14.44	47.14, 11.11	45.13, 13.98	45.52, 10.75	4384.26	13
Sentinel-1B	20771	443	2020-03-20T05:19:03	45.25, 14.05	45.65, 10.79	43.57, 13.58	43.97, 10.42	4288.52	13
Sentinel-1B	20771	438	2020-03-20T05:18:37	46.74, 14.44	47.14, 11.11	45.13, 13.98	45.52, 10.75	4430.83	13
Sentinel-1A	31667	440	2020-03-14T05:19:27	46.25, 14.30	46.65, 10.97	44.63, 13.84	45.03, 10.61	4426.86	13
Sentinel-1B	20596	443	2020-03-08T05:19:02	45.25, 14.05	45.65, 10.79	43.57, 13.58	43.97, 10.42	4421.44	13
Sentinel-1B	20596	438	2020-03-08T05:18:37	46.74, 14.44	47.14, 11.11	45.13, 13.98	45.52, 10.75	4460.06	13
Sentinel-1B	20421	443	2020-02-25T05:19:02	45.25, 14.05	45.65, 10.79	43.57, 13.58	43.97, 10.42	4321.97	14
Sentinel-1B	20421	438	2020-02-25T05:18:37	46.74, 14.44	47.14, 11.11	45.13, 13.98	45.52, 10.75	4425.47	14
Sentinel-1A	31317	440	2020-02-19T05:19:27	46.25, 14.30	46.65, 10.97	44.63, 13.85	45.03, 10.61	4353.18	14
Sentinel-1B	20246	443	2020-02-13T05:19:03	45.25, 14.05	45.65, 10.79	43.57, 13.58	43.97, 10.42	4278.65	14
Sentinel-1B	20246	438	2020-02-13T05:18:37	46.74, 14.44	47.14, 11.11	45.12, 13.98	45.52, 10.75	4415.95	14
Sentinel-1A	31142	440	2020-02-07T05:19:27	46.25, 14.30	46.65, 10.97	44.63, 13.84	45.03, 10.61	4342.71	14
Sentinel-1B	20071	443	2020-02-01T05:19:03	45.25, 14.05	45.65, 10.79	43.58, 13.59	43.97, 10.43	4319.20	15
Sentinel-1B	20071	438	2020-02-01T05:18:37	46.74, 14.45	47.14, 11.11	45.13, 13.99	45.52, 10.75	4452.91	15
Sentinel-1A	30967	440	2020-01-26T05:19:27	46.25, 14.30	46.65, 10.97	44.63, 13.84	45.03, 10.61	4440.28	15
Sentinel-1B	19896	443	2020-01-20T05:19:03	45.25, 14.05	45.65, 10.79	43.58, 13.59	43.97, 10.43	4487.91	15
Sentinel-1B	19896	438	2020-01-20T05:18:37	46.74, 14.45	47.14, 11.11	45.13, 13.99	45.52, 10.75	4424.12	15
Sentinel-1A	30792	440	2020-01-14T05:19:28	46.25, 14.30	46.65, 10.97	44.63, 13.85	45.03, 10.61	4325.59	15
Sentinel-1B	19721	443	2020-01-08T05:19:04	45.25, 14.05	45.65, 10.79	43.57, 13.58	43.97, 10.42	4406.72	16
Sentinel-1B	19721	438	2020-01-08T05:18:38	46.74, 14.44	47.14, 11.11	45.12, 13.98	45.52, 10.75	4423.86	16
Sentinel-1A	30617	440	2020-01-02T05:19:28	46.25, 14.30	46.65, 10.97	44.63, 13.85	45.03, 10.61	4366.19	16

Continued on next page...

Table A4.1 – continued from previous page

Platform	Orbit	Frame	Acq.@ Date & time	NS (Lat,Lon)	FS (Lat,Lon)	NE (Lat,Lon)	FE (Lat, Lon)	Size(MB)	R
Sentinel-1B	19546	443	2019-12-27T05:19:04	45.25, 14.05	45.65, 10.79	43.58, 13.58	43.97, 10.42	4425.33	16
Sentinel-1B	19546	438	2019-12-27T05:18:38	46.74, 14.44	47.14, 11.11	45.13, 13.98	45.52, 10.75	4457.12	16
Sentinel-1A	30442	440	2019-12-21T05:19:29	46.25, 14.30	46.65, 10.97	44.63, 13.85	45.03, 10.61	4563.49	16
Sentinel-1B	19371	443	2019-12-15T05:19:05	45.25, 14.05	45.65, 10.79	43.58, 13.58	43.97, 10.42	4395.20	16
Sentinel-1B	19371	438	2019-12-15T05:18:39	46.74, 14.44	47.14, 11.11	45.13, 13.98	45.52, 10.75	4460.88	16
Sentinel-1A	30267	440	2019-12-09T05:19:29	46.25, 14.30	46.65, 10.97	44.63, 13.85	45.03, 10.61	4410.29	16
Sentinel-1B	19196	443	2019-12-03T05:19:05	45.25, 14.05	45.65, 10.79	43.57, 13.58	43.97, 10.43	4537.09	16
Sentinel-1B	19196	438	2019-12-03T05:18:39	46.74, 14.45	47.14, 11.11	45.13, 13.98	45.52, 10.75	4467.63	16
Sentinel-1A	30092	440	2019-11-27T05:19:30	46.25, 14.30	46.65, 10.97	44.63, 13.84	45.03, 10.61	4435.74	16
Sentinel-1B	19021	443	2019-11-21T05:19:06	45.25, 14.05	45.65, 10.79	43.57, 13.58	43.97, 10.43	4444.25	16
Sentinel-1B	19021	438	2019-11-21T05:18:40	46.74, 14.45	47.14, 11.11	45.12, 13.98	45.52, 10.75	4498.66	16
Sentinel-1A	29917	440	2019-11-15T05:19:30	46.24, 14.30	46.65, 10.97	44.63, 13.84	45.03, 10.61	4552.75	16
Sentinel-1B	18846	443	2019-11-09T05:19:06	45.25, 14.05	45.65, 10.79	43.57, 13.59	43.97, 10.43	4528.22	16
Sentinel-1B	18846	438	2019-11-09T05:18:40	46.74, 14.45	47.14, 11.11	45.12, 13.99	45.52, 10.75	4515.12	16
Sentinel-1A	29742	440	2019-11-03T05:19:30	46.25, 14.30	46.65, 10.97	44.63, 13.85	45.03, 10.61	4498.43	16
Sentinel-1B	18671	440	2019-10-28T05:18:48	46.30, 14.33	46.70, 10.99	44.63, 13.86	45.03, 10.61	4477.63	16
Sentinel-1A	29567	440	2019-10-22T05:19:30	46.25, 14.30	46.65, 10.97	44.63, 13.85	45.03, 10.61	4400.52	16
Sentinel-1B	18496	440	2019-10-16T05:18:48	46.30, 14.33	46.70, 10.98	44.63, 13.86	45.03, 10.61	4631.59	16
Sentinel-1A	29392	440	2019-10-10T05:19:30	46.25, 14.30	46.65, 10.97	44.63, 13.85	45.03, 10.61	4425.99	16
Sentinel-1B	18321	440	2019-10-04T05:18:48	46.30, 14.33	46.70, 10.99	44.63, 13.86	45.03, 10.61	4552.03	16
Sentinel-1A	29217	440	2019-09-28T05:19:30	46.25, 14.30	46.65, 10.97	44.63, 13.84	45.03, 10.61	4420.54	16
Sentinel-1B	18146	440	2019-09-22T05:18:48	46.30, 14.33	46.70, 10.98	44.63, 13.86	45.03, 10.61	4516.42	16
Sentinel-1A	29042	440	2019-09-16T05:19:29	46.24, 14.30	46.65, 10.97	44.63, 13.84	45.03, 10.61	4377.00	16
Sentinel-1B	17971	440	2019-09-10T05:18:48	46.30, 14.33	46.70, 10.98	44.63, 13.86	45.03, 10.61	4593.86	16
Sentinel-1A	28867	440	2019-09-04T05:19:29	46.24, 14.30	46.65, 10.97	44.63, 13.84	45.03, 10.61	4425.12	16
Sentinel-1B	17796	440	2019-08-29T05:18:47	46.30, 14.33	46.70, 10.98	44.63, 13.86	45.03, 10.61	4541.25	16
Sentinel-1A	28692	440	2019-08-23T05:19:28	46.24, 14.30	46.65, 10.97	44.63, 13.84	45.03, 10.61	4460.07	16
Sentinel-1B	17621	440	2019-08-17T05:18:46	46.30, 14.33	46.70, 10.98	44.63, 13.86	45.03, 10.61	4516.83	16
Sentinel-1A	28517	440	2019-08-11T05:19:28	46.25, 14.30	46.65, 10.97	44.63, 13.84	45.03, 10.61	4428.67	16
Sentinel-1B	17446	440	2019-08-05T05:18:46	46.30, 14.33	46.70, 10.98	44.63, 13.86	45.03, 10.61	4531.21	16
Sentinel-1A	28342	440	2019-07-30T05:19:27	46.25, 14.30	46.65, 10.97	44.63, 13.84	45.03, 10.61	4391.21	16
Sentinel-1B	17271	440	2019-07-24T05:18:45	46.30, 14.33	46.70, 10.98	44.63, 13.86	45.03, 10.61	4470.77	16
Sentinel-1A	28167	440	2019-07-18T05:19:26	46.25, 14.30	46.65, 10.97	44.63, 13.84	45.03, 10.61	4439.78	16
Sentinel-1B	17096	440	2019-07-12T05:18:44	46.30, 14.33	46.70, 10.98	44.63, 13.86	45.03, 10.61	4528.17	16

Continued on next page...

Table A4.1 – continued from previous page

Platform	Orbit	Frame	Acq.@ Date & time	NS (Lat,Lon)	FS (Lat,Lon)	NE (Lat,Lon)	FE (Lat, Lon)	Size(MB)	R
Sentinel-1A	27992	440	2019-07-06T05:19:25	46.25, 14.30	46.65, 10.97	44.63, 13.84	45.03, 10.61	4414.65	16
Sentinel-1B	16921	440	2019-06-30T05:18:43	46.30, 14.33	46.70, 10.98	44.63, 13.86	45.03, 10.61	4510.91	16
Sentinel-1A	27817	440	2019-06-24T05:19:25	46.24, 14.31	46.65, 10.98	44.63, 13.86	45.03, 10.62	4404.26	15
Sentinel-1B	16746	440	2019-06-18T05:18:43	46.30, 14.34	46.70, 10.99	44.63, 13.87	45.03, 10.62	4522.80	15
Sentinel-1A	27642	440	2019-06-12T05:19:24	46.24, 14.31	46.65, 10.97	44.63, 13.86	45.03, 10.62	4430.79	15
Sentinel-1B	16571	440	2019-06-06T05:18:42	46.30, 14.34	46.70, 10.99	44.63, 13.87	45.03, 10.62	4549.53	15
Sentinel-1A	27467	440	2019-05-31T05:19:23	46.24, 14.31	46.65, 10.97	44.63, 13.86	45.03, 10.62	4410.41	15
Sentinel-1B	16396	440	2019-05-25T05:18:41	46.30, 14.34	46.70, 10.99	44.63, 13.87	45.03, 10.62	4486.04	15
Sentinel-1A	27292	440	2019-05-19T05:19:23	46.24, 14.31	46.65, 10.97	44.63, 13.86	45.03, 10.61	4491.08	15
Sentinel-1B	16221	441	2019-05-13T05:18:47	45.91, 14.23	46.31, 10.94	44.24, 13.76	44.64, 10.57	4504.87	15
Sentinel-1B	16046	441	2019-05-01T05:18:47	45.91, 14.23	46.31, 10.93	44.24, 13.76	44.64, 10.56	4324.57	15
Sentinel-1A	26942	440	2019-04-25T05:19:22	46.24, 14.31	46.65, 10.97	44.63, 13.86	45.03, 10.62	4428.68	15
Sentinel-1B	15871	441	2019-04-19T05:18:46	45.91, 14.23	46.31, 10.94	44.24, 13.76	44.64, 10.56	4346.93	15
Sentinel-1A	26767	440	2019-04-13T05:19:21	46.24, 14.31	46.65, 10.97	44.63, 13.86	45.03, 10.62	4432.90	15
Sentinel-1B	15696	441	2019-04-07T05:18:46	45.91, 14.23	46.31, 10.93	44.24, 13.76	44.64, 10.56	4366.53	15
Sentinel-1A	26592	440	2019-04-01T05:19:21	46.24, 14.31	46.65, 10.97	44.63, 13.86	45.03, 10.61	4336.29	15
Sentinel-1B	15521	441	2019-03-26T05:18:45	45.91, 14.23	46.31, 10.94	44.24, 13.76	44.64, 10.57	4470.50	15
Sentinel-1A	26417	440	2019-03-20T05:19:21	46.24, 14.31	46.65, 10.97	44.63, 13.86	45.03, 10.61	4382.19	15
Sentinel-1B	15346	441	2019-03-14T05:18:45	45.91, 14.23	46.31, 10.94	44.24, 13.76	44.64, 10.57	4325.98	16
Sentinel-1A	26242	440	2019-03-08T05:19:21	46.24, 14.31	46.65, 10.97	44.63, 13.86	45.03, 10.61	4361.78	16
Sentinel-1B	15171	441	2019-03-02T05:18:45	45.91, 14.23	46.31, 10.94	44.24, 13.76	44.64, 10.57	4288.23	16
Sentinel-1A	26067	440	2019-02-24T05:19:20	46.24, 14.31	46.65, 10.97	44.63, 13.86	45.03, 10.62	4341.42	16
Sentinel-1B	14996	441	2019-02-18T05:18:45	45.91, 14.23	46.31, 10.94	44.24, 13.76	44.64, 10.56	4279.79	16
Sentinel-1A	25892	440	2019-02-12T05:19:21	46.24, 14.32	46.65, 10.98	44.63, 13.86	45.03, 10.62	4368.56	16
Sentinel-1B	14821	441	2019-02-06T05:18:46	45.91, 14.23	46.31, 10.93	44.24, 13.76	44.64, 10.56	4410.35	16
Sentinel-1A	25717	440	2019-01-31T05:19:21	46.24, 14.31	46.65, 10.97	44.63, 13.86	45.03, 10.62	4378.77	16
Sentinel-1B	14646	441	2019-01-25T05:18:46	45.91, 14.23	46.31, 10.94	44.24, 13.76	44.64, 10.57	4354.07	16
Sentinel-1A	25542	440	2019-01-19T05:19:21	46.24, 14.31	46.65, 10.97	44.63, 13.86	45.03, 10.62	4407.27	16
Sentinel-1B	14471	441	2019-01-13T05:18:46	45.91, 14.23	46.31, 10.94	44.24, 13.77	44.64, 10.57	4338.65	15
Sentinel-1A	25367	440	2019-01-07T05:19:22	46.24, 14.31	46.65, 10.97	44.63, 13.86	45.03, 10.62	4356.37	15
Sentinel-1B	14296	441	2019-01-01T05:18:47	45.91, 14.23	46.31, 10.94	44.24, 13.77	44.64, 10.57	4415.83	15
Sentinel-1A	25192	440	2018-12-26T05:19:22	46.24, 14.31	46.65, 10.97	44.63, 13.86	45.03, 10.62	4390.59	15
Sentinel-1B	14121	441	2018-12-20T05:18:47	45.91, 14.23	46.31, 10.94	44.24, 13.76	44.64, 10.57	4517.49	15
Sentinel-1A	25017	440	2018-12-14T05:19:22	46.24, 14.32	46.65, 10.98	44.63, 13.86	45.03, 10.62	4377.65	15

Continued on next page...

Table A4.1 – continued from previous page

Platform	Orbit	Frame	Acq.@ Date & time	NS (Lat,Lon)	FS (Lat,Lon)	NE (Lat,Lon)	FE (Lat, Lon)	Size(MB)	R
Sentinel-1B	13946	441	2018-12-08T05:18:48	45.91, 14.23	46.31, 10.94	44.24, 13.76	44.64, 10.57	4571.11	15
Sentinel-1A	24842	440	2018-12-02T05:19:23	46.24, 14.32	46.65, 10.98	44.63, 13.86	45.03, 10.62	4424.19	15
Sentinel-1A	24667	440	2018-11-20T05:19:23	46.24, 14.32	46.65, 10.98	44.63, 13.86	45.03, 10.62	4519.68	15
Sentinel-1B	13596	440	2018-11-14T05:18:42	46.30, 14.34	46.70, 10.99	44.63, 13.87	45.03, 10.62	4580.50	15
Sentinel-1A	24492	440	2018-11-08T05:19:24	46.24, 14.31	46.65, 10.97	44.63, 13.86	45.03, 10.62	4475.83	15
Sentinel-1B	13421	440	2018-11-02T05:18:42	46.30, 14.34	46.70, 10.99	44.63, 13.87	45.03, 10.62	4617.69	15
Sentinel-1A	24317	440	2018-10-27T05:19:24	46.24, 14.31	46.65, 10.97	44.63, 13.86	45.03, 10.62	4452.47	15
Sentinel-1B	13246	440	2018-10-21T05:18:42	46.30, 14.34	46.70, 10.99	44.63, 13.87	45.03, 10.62	4495.28	15
Sentinel-1A	24142	440	2018-10-15T05:19:24	46.24, 14.31	46.65, 10.97	44.63, 13.86	45.03, 10.62	4376.21	15
Sentinel-1B	13071	440	2018-10-09T05:18:41	46.30, 14.34	46.70, 11.03	44.68, 13.88	45.07, 10.67	4386.84	15
Sentinel-1A	23967	440	2018-10-03T05:19:24	46.24, 14.32	46.65, 10.98	44.63, 13.86	45.03, 10.62	4402.04	16
Sentinel-1B	12896	441	2018-09-27T05:18:47	45.91, 14.23	46.31, 10.90	44.29, 13.78	44.70, 10.55	4284.76	16
Sentinel-1A	23792	440	2018-09-21T05:19:23	46.24, 14.31	46.64, 10.97	44.63, 13.86	45.03, 10.62	4395.85	16
Sentinel-1B	12721	440	2018-09-15T05:18:41	46.30, 14.34	46.70, 10.99	44.63, 13.87	45.03, 10.62	4598.65	16
Sentinel-1A	23617	440	2018-09-09T05:19:23	46.24, 14.31	46.64, 10.97	44.63, 13.86	45.03, 10.61	4428.55	16
Sentinel-1B	12546	440	2018-09-03T05:18:41	46.30, 14.34	46.70, 10.99	44.62, 13.87	45.03, 10.62	4589.37	16
Sentinel-1A	23442	440	2018-08-28T05:19:23	46.24, 14.31	46.64, 10.97	44.63, 13.86	45.03, 10.62	4448.18	16
Sentinel-1B	12371	440	2018-08-22T05:18:40	46.30, 14.34	46.70, 10.99	44.63, 13.87	45.03, 10.62	4549.90	16
Sentinel-1A	23267	440	2018-08-16T05:19:22	46.24, 14.31	46.64, 10.97	44.63, 13.86	45.03, 10.62	4457.04	16
Sentinel-1B	12196	440	2018-08-10T05:18:39	46.30, 14.34	46.70, 10.99	44.63, 13.87	45.03, 10.62	4548.70	16
Sentinel-1A	23092	440	2018-08-04T05:19:21	46.24, 14.31	46.65, 10.97	44.63, 13.86	45.03, 10.62	4455.25	16
Sentinel-1B	12021	440	2018-07-29T05:18:39	46.30, 14.34	46.70, 10.99	44.63, 13.87	45.03, 10.62	4527.67	16
Sentinel-1A	22917	440	2018-07-23T05:19:20	46.24, 14.31	46.65, 10.97	44.63, 13.86	45.03, 10.62	4467.07	16
Sentinel-1B	11846	440	2018-07-17T05:18:38	46.30, 14.34	46.70, 10.99	44.63, 13.87	45.03, 10.62	4582.72	16
Sentinel-1A	22742	440	2018-07-11T05:19:20	46.24, 14.31	46.65, 10.97	44.63, 13.86	45.03, 10.62	4502.33	16
Sentinel-1B	11671	443	2018-07-05T05:18:54	45.25, 14.05	45.65, 10.76	43.63, 13.60	44.04, 10.40	4173.06	16
Sentinel-1B	11671	438	2018-07-05T05:18:29	46.74, 14.46	47.14, 11.08	45.12, 14.00	45.53, 10.72	4506.91	16
Sentinel-1A	22567	440	2018-06-29T05:19:19	46.24, 14.31	46.65, 10.97	44.63, 13.86	45.03, 10.62	4424.73	16
Sentinel-1B	11496	441	2018-06-23T05:18:42	45.91, 14.23	46.32, 10.90	44.30, 13.78	44.70, 10.55	4348.01	16
Sentinel-1A	22392	440	2018-06-17T05:19:18	46.24, 14.31	46.65, 10.97	44.63, 13.86	45.03, 10.62	4414.84	16
Sentinel-1B	11321	441	2018-06-11T05:18:42	45.91, 14.23	46.32, 10.90	44.30, 13.78	44.70, 10.55	4243.83	16
Sentinel-1A	22217	440	2018-06-05T05:19:18	46.24, 14.32	46.65, 10.98	44.63, 13.86	45.03, 10.62	4429.83	16
Sentinel-1B	11146	441	2018-05-30T05:18:41	45.91, 14.24	46.32, 10.90	44.30, 13.78	44.70, 10.55	4232.10	16
Sentinel-1A	22042	440	2018-05-24T05:19:17	46.24, 14.31	46.65, 10.97	44.63, 13.86	45.03, 10.62	4441.31	16

Continued on next page...

Table A4.1 – continued from previous page

Platform	Orbit	Frame	Acq.@ Date & time	NS (Lat,Lon)	FS (Lat,Lon)	NE (Lat,Lon)	FE (Lat, Lon)	Size(MB)	R
Sentinel-1B	10971	441	2018-05-18T05:18:41	45.91, 14.24	46.31, 10.94	44.24, 13.77	44.64, 10.57	4365.80	16
Sentinel-1A	21867	440	2018-05-12T05:19:16	46.24, 14.31	46.65, 10.97	44.63, 13.86	45.03, 10.62	4378.65	16
Sentinel-1B	10796	441	2018-05-06T05:18:40	45.91, 14.24	46.31, 10.94	44.24, 13.77	44.64, 10.57	4387.96	16
Sentinel-1A	21692	440	2018-04-30T05:19:16	46.24, 14.31	46.65, 10.97	44.63, 13.86	45.03, 10.61	4420.46	16
Sentinel-1B	10621	441	2018-04-24T05:18:39	45.91, 14.24	46.32, 10.90	44.30, 13.78	44.70, 10.55	4180.87	16
Sentinel-1A	21517	440	2018-04-18T05:19:15	46.24, 14.31	46.64, 10.97	44.63, 13.86	45.03, 10.62	4395.18	16
Sentinel-1B	10446	441	2018-04-12T05:18:39	45.91, 14.23	46.31, 10.94	44.24, 13.77	44.64, 10.57	4538.51	16
Sentinel-1A	21342	440	2018-04-06T05:19:15	46.24, 14.31	46.64, 10.98	44.63, 13.86	45.03, 10.62	4397.27	16
Sentinel-1B	10271	441	2018-03-31T05:18:39	45.91, 14.23	46.31, 10.93	44.24, 13.76	44.64, 10.56	4498.90	16
Sentinel-1A	21167	440	2018-03-25T05:19:14	46.24, 14.32	46.65, 10.98	44.63, 13.86	45.03, 10.62	4398.86	16
Sentinel-1B	10096	441	2018-03-19T05:18:39	45.91, 14.23	46.31, 10.94	44.24, 13.77	44.64, 10.57	4600.76	16
Sentinel-1A	20992	440	2018-03-13T05:19:14	46.24, 14.31	46.65, 10.97	44.63, 13.86	45.03, 10.62	4412.65	16
Sentinel-1B	9921	441	2018-03-07T05:18:38	45.91, 14.24	46.31, 10.94	44.24, 13.77	44.64, 10.57	4438.17	16
Sentinel-1A	20817	440	2018-03-01T05:19:14	46.24, 14.31	46.65, 10.97	44.63, 13.86	45.03, 10.62	4316.02	16
Sentinel-1B	9746	441	2018-02-23T05:18:38	45.91, 14.24	46.31, 10.94	44.24, 13.77	44.64, 10.57	4596.68	16
Sentinel-1A	20642	440	2018-02-17T05:19:14	46.24, 14.31	46.64, 10.97	44.63, 13.86	45.03, 10.62	4326.47	16
Sentinel-1B	9571	441	2018-02-11T05:18:39	45.91, 14.24	46.31, 10.94	44.24, 13.77	44.64, 10.57	4454.41	16
Sentinel-1A	20467	440	2018-02-05T05:19:14	46.24, 14.31	46.65, 10.97	44.63, 13.86	45.03, 10.62	4419.02	16
Sentinel-1B	9396	441	2018-01-30T05:18:39	45.91, 14.24	46.31, 10.94	44.24, 13.77	44.64, 10.57	4402.38	16
Sentinel-1A	20292	440	2018-01-24T05:19:15	46.24, 14.32	46.65, 10.98	44.63, 13.86	45.03, 10.62	4326.52	16
Sentinel-1B	9221	441	2018-01-18T05:18:39	45.91, 14.24	46.31, 10.94	44.24, 13.77	44.64, 10.57	4440.04	16
Sentinel-1A	20117	440	2018-01-12T05:19:15	46.24, 14.32	46.65, 10.98	44.63, 13.86	45.03, 10.62	4444.92	16
Sentinel-1B	9046	441	2018-01-06T05:18:40	45.91, 14.24	46.31, 10.94	44.24, 13.77	44.64, 10.57	4414.97	15
Sentinel-1A	19942	440	2017-12-31T05:19:15	46.24, 14.32	46.65, 10.98	44.63, 13.86	45.03, 10.62	4336.91	15
Sentinel-1B	8871	441	2017-12-25T05:18:40	45.91, 14.24	46.31, 10.94	44.24, 13.77	44.64, 10.57	4294.47	14
Sentinel-1A	19767	440	2017-12-19T05:19:16	46.24, 14.31	46.65, 10.97	44.63, 13.86	45.03, 10.62	4329.63	14
Sentinel-1B	8696	441	2017-12-13T05:18:41	45.91, 14.24	46.31, 10.94	44.24, 13.77	44.64, 10.57	4503.51	14
Sentinel-1A	19592	440	2017-12-07T05:19:16	46.24, 14.32	46.65, 10.98	44.63, 13.86	45.03, 10.62	4340.09	14
Sentinel-1B	8521	441	2017-12-01T05:18:41	45.91, 14.24	46.31, 10.94	44.24, 13.77	44.64, 10.57	4415.21	14
Sentinel-1A	19417	440	2017-11-25T05:19:17	46.24, 14.32	46.65, 10.98	44.63, 13.86	45.03, 10.62	4388.16	14
Sentinel-1A	19242	440	2017-11-13T05:19:17	46.24, 14.32	46.64, 10.98	44.63, 13.86	45.03, 10.62	4546.46	14
Sentinel-1A	19067	440	2017-11-01T05:19:17	46.24, 14.31	46.65, 10.97	44.63, 13.86	45.03, 10.62	4365.02	14
Sentinel-1B	7996	441	2017-10-26T05:18:41	45.91, 14.24	46.31, 10.90	44.29, 13.78	44.70, 10.55	4283.11	14
Sentinel-1A	18892	440	2017-10-20T05:19:17	46.24, 14.31	46.65, 10.97	44.63, 13.86	45.03, 10.62	4349.89	14

Continued on next page...

Table A4.1 – continued from previous page

Platform	Orbit	Frame	Acq.@ Date & time	NS (Lat,Lon)	FS (Lat,Lon)	NE (Lat,Lon)	FE (Lat, Lon)	Size(MB)	R
Sentinel-1B	7821	441	2017-10-14T05:18:41	45.91, 14.24	46.31, 10.90	44.29, 13.79	44.70, 10.55	4239.08	14
Sentinel-1A	18717	440	2017-10-08T05:19:17	46.24, 14.31	46.65, 10.97	44.63, 13.86	45.03, 10.62	4404.09	14
Sentinel-1B	7646	441	2017-10-02T05:18:41	45.91, 14.24	46.31, 10.90	44.29, 13.78	44.70, 10.55	4306.69	14
Sentinel-1A	18542	440	2017-09-26T05:19:17	46.24, 14.31	46.64, 10.97	44.63, 13.86	45.03, 10.62	4423.07	15
Sentinel-1B	7471	441	2017-09-20T05:18:40	45.91, 14.23	46.31, 10.90	44.29, 13.78	44.70, 10.55	4400.58	15
Sentinel-1A	18367	440	2017-09-14T05:19:17	46.24, 14.31	46.64, 10.97	44.63, 13.86	45.03, 10.62	4451.87	16
Sentinel-1B	7296	441	2017-09-08T05:18:40	45.91, 14.24	46.31, 10.90	44.29, 13.78	44.70, 10.55	4353.76	16
Sentinel-1A	18192	440	2017-09-02T05:19:16	46.24, 14.31	46.64, 10.97	44.63, 13.86	45.03, 10.62	4471.01	16
Sentinel-1B	7121	441	2017-08-27T05:18:39	45.91, 14.24	46.32, 10.90	44.29, 13.78	44.70, 10.55	4197.57	16
Sentinel-1A	18017	440	2017-08-21T05:19:16	46.24, 14.31	46.64, 10.97	44.63, 13.86	45.03, 10.62	4439.22	16
Sentinel-1B	6946	441	2017-08-15T05:18:39	45.91, 14.24	46.32, 10.90	44.30, 13.78	44.70, 10.55	4220.76	16
Sentinel-1A	17842	440	2017-08-09T05:19:15	46.24, 14.31	46.65, 10.97	44.63, 13.86	45.03, 10.62	4433.09	16
Sentinel-1B	6771	441	2017-08-03T05:18:38	45.91, 14.24	46.32, 10.90	44.30, 13.78	44.70, 10.55	4230.41	16
Sentinel-1A	17667	440	2017-07-28T05:19:14	46.24, 14.31	46.65, 10.97	44.63, 13.86	45.03, 10.62	4429.79	16
Sentinel-1B	6596	441	2017-07-22T05:18:38	45.91, 14.23	46.32, 10.90	44.29, 13.78	44.70, 10.55	4296.19	16
Sentinel-1A	17492	440	2017-07-16T05:19:14	46.24, 14.31	46.65, 10.97	44.63, 13.86	45.03, 10.62	4440.37	16
Sentinel-1B	6421	441	2017-07-10T05:18:37	45.91, 14.23	46.32, 10.90	44.29, 13.78	44.70, 10.55	4293.48	16
Sentinel-1A	17317	440	2017-07-04T05:19:13	46.24, 14.31	46.65, 10.97	44.63, 13.86	45.03, 10.62	4433.60	16
Sentinel-1B	6246	441	2017-06-28T05:18:36	45.91, 14.24	46.31, 10.90	44.29, 13.78	44.70, 10.55	4298.15	16
Sentinel-1A	17142	440	2017-06-22T05:19:12	46.24, 14.31	46.65, 10.97	44.63, 13.86	45.03, 10.62	4376.79	16
Sentinel-1B	6071	441	2017-06-16T05:18:35	45.91, 14.24	46.32, 10.90	44.29, 13.78	44.70, 10.55	4227.74	16
Sentinel-1A	16967	440	2017-06-10T05:19:12	46.24, 14.31	46.65, 10.97	44.63, 13.86	45.03, 10.61	4356.16	16
Sentinel-1B	5896	441	2017-06-04T05:18:35	45.91, 14.24	46.32, 10.90	44.29, 13.78	44.70, 10.55	4281.71	16
Sentinel-1A	16792	440	2017-05-29T05:19:11	46.24, 14.31	46.65, 10.98	44.63, 13.86	45.03, 10.62	4354.89	16
Sentinel-1B	5721	441	2017-05-23T05:18:34	45.91, 14.23	46.32, 10.90	44.29, 13.78	44.70, 10.54	4181.69	16
Sentinel-1A	16617	443	2017-05-17T05:19:24	45.42, 14.08	45.82, 10.79	43.80, 13.63	44.20, 10.44	4158.94	16
Sentinel-1B	5546	441	2017-05-11T05:18:33	45.91, 14.23	46.32, 10.90	44.29, 13.78	44.70, 10.55	4307.20	16
Sentinel-1A	16442	443	2017-05-05T05:19:23	45.42, 14.08	45.82, 10.79	43.80, 13.63	44.20, 10.44	4291.14	16
Sentinel-1B	5371	441	2017-04-29T05:18:34	45.91, 14.23	46.31, 10.94	44.24, 13.77	44.64, 10.56	4431.93	16
Sentinel-1A	16267	443	2017-04-23T05:19:23	45.42, 14.08	45.82, 10.79	43.80, 13.63	44.20, 10.44	4170.41	16
Sentinel-1B	5196	441	2017-04-17T05:18:33	45.91, 14.24	46.31, 10.94	44.24, 13.77	44.64, 10.57	4420.58	16
Sentinel-1A	16092	443	2017-04-11T05:19:22	45.42, 14.08	45.82, 10.79	43.80, 13.63	44.20, 10.44	4099.81	16
Sentinel-1B	5021	441	2017-04-05T05:18:33	45.91, 14.23	46.31, 10.94	44.24, 13.77	44.64, 10.57	4409.89	16
Sentinel-1A	15917	443	2017-03-30T05:19:22	45.42, 14.08	45.82, 10.79	43.80, 13.63	44.20, 10.44	4085.90	16

Continued on next page...

Table A4.1 – continued from previous page

Platform	Orbit	Frame	Acq.@ Date & time	NS (Lat,Lon)	FS (Lat,Lon)	NE (Lat,Lon)	FE (Lat, Lon)	Size(MB)	R
Sentinel-1B	4846	441	2017-03-24T05:18:32	45.91, 14.24	46.31, 10.94	44.24, 13.77	44.64, 10.57	4307.07	16
Sentinel-1A	15742	443	2017-03-18T05:19:21	45.42, 14.08	45.82, 10.79	43.80, 13.63	44.20, 10.44	4154.28	16
Sentinel-1B	4671	441	2017-03-12T05:18:31	45.91, 14.23	46.31, 10.93	44.29, 13.78	44.69, 10.58	4168.18	16
Sentinel-1A	15567	443	2017-03-06T05:19:21	45.42, 14.08	45.82, 10.79	43.80, 13.63	44.20, 10.44	4183.41	15
Sentinel-1B	4496	441	2017-02-28T05:18:32	45.91, 14.24	46.31, 10.94	44.24, 13.77	44.64, 10.57	4409.57	15
Sentinel-1A	15392	443	2017-02-22T05:19:21	45.42, 14.08	45.82, 10.79	43.80, 13.63	44.20, 10.44	4164.83	15
Sentinel-1B	4321	441	2017-02-16T05:18:31	45.91, 14.24	46.31, 10.94	44.29, 13.78	44.69, 10.58	4200.82	15
Sentinel-1A	15217	443	2017-02-10T05:19:21	45.42, 14.08	45.82, 10.79	43.80, 13.63	44.20, 10.44	4264.53	15
Sentinel-1B	4146	441	2017-02-04T05:18:32	45.91, 14.24	46.31, 10.94	44.24, 13.77	44.64, 10.57	4505.00	15
Sentinel-1A	15042	443	2017-01-29T05:19:22	45.42, 14.08	45.82, 10.79	43.80, 13.63	44.20, 10.44	4086.11	15
Sentinel-1B	3971	441	2017-01-23T05:18:32	45.91, 14.24	46.31, 10.94	44.24, 13.77	44.64, 10.57	4278.87	15
Sentinel-1B	3796	441	2017-01-11T05:18:33	45.91, 14.24	46.31, 10.94	44.24, 13.77	44.64, 10.57	4290.20	15
Sentinel-1A	14692	443	2017-01-05T05:19:22	45.42, 14.08	45.82, 10.80	43.80, 13.63	44.20, 10.44	4190.29	15
Sentinel-1B	3621	441	2016-12-30T05:18:34	45.91, 14.24	46.31, 10.94	44.24, 13.77	44.64, 10.56	4349.45	15
Sentinel-1A	14517	443	2016-12-24T05:19:24	45.42, 14.08	45.82, 10.79	43.80, 13.63	44.20, 10.44	4235.95	15
Sentinel-1B	3446	439	2016-12-18T05:18:23	46.57, 14.42	46.97, 11.09	44.96, 13.96	45.36, 10.73	4347.22	15
Sentinel-1A	14342	443	2016-12-12T05:19:24	45.42, 14.08	45.82, 10.79	43.80, 13.63	44.20, 10.44	4302.24	15
Sentinel-1B	3271	439	2016-12-06T05:18:23	46.57, 14.42	46.97, 11.09	44.96, 13.96	45.36, 10.73	4365.18	15
Sentinel-1A	14167	443	2016-11-30T05:19:25	45.42, 14.08	45.82, 10.79	43.80, 13.63	44.20, 10.44	4258.97	15
Sentinel-1B	3096	439	2016-11-24T05:18:23	46.57, 14.42	46.97, 11.09	44.96, 13.96	45.36, 10.73	4483.73	16
Sentinel-1A	13992	443	2016-11-18T05:19:25	45.42, 14.08	45.82, 10.79	43.80, 13.63	44.20, 10.44	4296.81	16
Sentinel-1B	2921	440	2016-11-12T05:18:29	46.24, 14.33	46.64, 11.02	44.63, 13.87	45.02, 10.66	4427.62	15
Sentinel-1A	13817	443	2016-11-06T05:19:25	45.42, 14.08	45.82, 10.79	43.80, 13.63	44.20, 10.44	4371.54	15
Sentinel-1B	2746	441	2016-10-31T05:18:35	45.91, 14.24	46.31, 10.90	44.29, 13.78	44.70, 10.55	4330.33	14
Sentinel-1A	13642	443	2016-10-25T05:19:25	45.42, 14.08	45.82, 10.79	43.80, 13.63	44.20, 10.44	4299.42	14
Sentinel-1B	2571	441	2016-10-19T05:18:35	45.91, 14.24	46.31, 10.90	44.29, 13.78	44.70, 10.55	4335.66	13
Sentinel-1A	13467	443	2016-10-13T05:19:25	45.42, 14.08	45.82, 10.79	43.80, 13.63	44.20, 10.44	4233.20	13
Sentinel-1B	2396	441	2016-10-07T05:18:35	45.91, 14.24	46.31, 10.90	44.29, 13.78	44.70, 10.55	4274.34	12
Sentinel-1A	13292	443	2016-10-01T05:19:25	45.42, 14.08	45.82, 10.79	43.80, 13.63	44.20, 10.44	4250.69	12
Sentinel-1A	13117	443	2016-09-19T05:19:25	45.42, 14.08	45.82, 10.79	43.80, 13.63	44.20, 10.44	4311.60	11
Sentinel-1A	12942	443	2016-09-07T05:19:24	45.42, 14.08	45.82, 10.79	43.80, 13.63	44.20, 10.44	4380.50	10
Sentinel-1A	12767	443	2016-08-26T05:19:24	45.42, 14.08	45.82, 10.79	43.80, 13.63	44.20, 10.44	4251.67	9
Sentinel-1A	12592	443	2016-08-14T05:19:23	45.42, 14.08	45.82, 10.79	43.80, 13.63	44.20, 10.44	4225.43	7
Sentinel-1A	12417	443	2016-08-02T05:19:23	45.42, 14.08	45.82, 10.79	43.80, 13.63	44.20, 10.44	4253.43	7

Continued on next page...

Table A4.1 – continued from previous page

Platform	Orbit	Frame	Acq.@ Date & time	NS (Lat,Lon)	FS (Lat,Lon)	NE (Lat,Lon)	FE (Lat, Lon)	Size(MB)	R
Sentinel-1A	12242	443	2016-07-21T05:19:22	45.42, 14.08	45.82, 10.79	43.80, 13.63	44.20, 10.44	4218.76	7
Sentinel-1A	12067	443	2016-07-09T05:19:21	45.42, 14.08	45.82, 10.79	43.80, 13.63	44.20, 10.44	4234.14	7
Sentinel-1A	11717	443	2016-06-15T05:19:20	45.42, 14.08	45.82, 10.79	43.80, 13.63	44.20, 10.44	4368.17	7
Sentinel-1A	11542	443	2016-06-03T05:19:19	45.42, 14.08	45.82, 10.79	43.80, 13.63	44.20, 10.44	4275.13	7
Sentinel-1A	11367	442	2016-05-22T05:19:17	45.59, 14.09	45.98, 10.86	43.91, 13.63	44.31, 10.50	4287.81	7
Sentinel-1A	11192	443	2016-05-10T05:19:22	45.26, 14.00	45.65, 10.79	43.58, 13.54	43.98, 10.43	4373.58	7
Sentinel-1A	11192	438	2016-05-10T05:18:56	46.75, 14.41	47.14, 11.12	45.13, 13.95	45.52, 10.76	4436.44	7
Sentinel-1A	11017	442	2016-04-28T05:19:16	45.59, 14.09	45.98, 10.87	43.91, 13.63	44.31, 10.50	4368.94	8
Sentinel-1A	10842	443	2016-04-16T05:19:21	45.26, 14.00	45.65, 10.80	43.58, 13.54	43.97, 10.43	4301.47	8
Sentinel-1A	10842	438	2016-04-16T05:18:55	46.75, 14.42	47.14, 11.12	45.13, 13.96	45.52, 10.76	4448.17	8
Sentinel-1A	10667	442	2016-04-04T05:19:15	45.59, 14.09	45.98, 10.86	43.91, 13.63	44.31, 10.50	4347.28	8
Sentinel-1A	10492	443	2016-03-23T05:19:20	45.26, 14.00	45.65, 10.79	43.58, 13.54	43.97, 10.43	4481.07	8
Sentinel-1A	10492	438	2016-03-23T05:18:54	46.74, 14.41	47.14, 11.12	45.13, 13.95	45.52, 10.76	4456.46	8
Sentinel-1A	10317	442	2016-03-11T05:19:14	45.59, 14.09	45.98, 10.86	43.91, 13.63	44.31, 10.50	4490.58	8
Sentinel-1A	10142	439	2016-02-28T05:18:56	46.58, 14.37	46.97, 11.09	44.96, 13.91	45.36, 10.73	4508.03	8
Sentinel-1A	9967	442	2016-02-16T05:19:14	45.59, 14.09	45.98, 10.87	43.91, 13.63	44.31, 10.50	4557.28	7
Sentinel-1A	9792	439	2016-02-04T05:18:57	46.58, 14.37	46.97, 11.09	44.96, 13.91	45.35, 10.73	4453.82	7
Sentinel-1A	9617	442	2016-01-23T05:19:14	45.59, 14.09	45.98, 10.86	43.91, 13.63	44.31, 10.50	4300.23	7
Sentinel-1A	9442	439	2016-01-11T05:18:57	46.58, 14.37	46.97, 11.09	44.96, 13.91	45.36, 10.73	4530.04	8
Sentinel-1A	9092	439	2015-12-18T05:18:58	46.58, 14.37	46.97, 11.09	44.96, 13.91	45.36, 10.73	4386.35	7
Sentinel-1A	8917	442	2015-12-06T05:19:16	45.59, 14.09	45.98, 10.87	43.91, 13.63	44.31, 10.50	4386.14	6
Sentinel-1A	8742	439	2015-11-24T05:18:59	46.58, 14.37	46.97, 11.09	44.96, 13.91	45.36, 10.73	4437.37	5
Sentinel-1A	8567	439	2015-11-12T05:18:59	46.58, 14.37	46.97, 11.09	44.96, 13.91	45.35, 10.73	4464.31	6
Sentinel-1A	8392	442	2015-10-31T05:19:16	45.58, 14.13	45.98, 10.83	43.97, 13.68	44.37, 10.47	4388.49	6
Sentinel-1A	7692	442	2015-09-13T05:19:15	45.58, 14.14	45.98, 10.83	43.96, 13.69	44.37, 10.47	4271.08	6
Sentinel-1A	7517	442	2015-09-01T05:19:15	45.58, 14.13	45.98, 10.83	43.96, 13.68	44.37, 10.47	4271.56	6
Sentinel-1A	7342	442	2015-08-20T05:19:14	45.58, 14.13	45.98, 10.83	43.96, 13.68	44.37, 10.47	4310.40	5
Sentinel-1A	7167	442	2015-08-08T05:19:14	45.58, 14.13	45.98, 10.83	43.96, 13.68	44.37, 10.47	4231.84	5
Sentinel-1A	6817	442	2015-07-15T05:19:12	45.58, 14.13	45.98, 10.83	43.96, 13.68	44.37, 10.47	4207.11	6
Sentinel-1A	6642	442	2015-07-03T05:19:12	45.58, 14.13	45.98, 10.83	43.96, 13.68	44.37, 10.47	4192.77	6
Sentinel-1A	6292	442	2015-06-09T05:19:11	45.58, 14.13	45.98, 10.83	43.96, 13.68	44.37, 10.47	4261.24	5
Sentinel-1A	5942	442	2015-05-16T05:19:08	45.74, 14.19	46.15, 10.90	44.07, 13.73	44.47, 10.53	4478.99	5
Sentinel-1A	5767	442	2015-05-04T05:19:07	45.75, 14.17	46.15, 10.89	44.07, 13.71	44.47, 10.53	4423.07	6
Sentinel-1A	5592	439	2015-04-22T05:18:51	46.57, 14.41	46.97, 11.09	44.96, 13.95	45.36, 10.73	4414.07	7

Continued on next page...

Table A4.1 – continued from previous page

Platform	Orbit	Frame	Acq.@ Date & time	NS (Lat,Lon)	FS (Lat,Lon)	NE (Lat,Lon)	FE (Lat, Lon)	Size(MB)	R
Sentinel-1A	5417	439	2015-04-10T05:18:51	46.57, 14.41	46.97, 11.09	44.96, 13.95	45.36, 10.73	4459.32	7
Sentinel-1A	5242	439	2015-03-29T05:18:51	46.57, 14.41	46.97, 11.09	44.96, 13.95	45.36, 10.73	4507.89	7
Sentinel-1A	5067	439	2015-03-17T05:18:51	46.59, 14.41	46.98, 11.09	44.95, 13.95	45.35, 10.73	4620.44	8
Sentinel-1A	4892	439	2015-03-05T05:18:50	46.58, 14.41	46.98, 11.09	44.95, 13.95	45.35, 10.73	4575.48	7
Sentinel-1A	4717	439	2015-02-21T05:18:50	46.58, 14.41	46.98, 11.09	44.95, 13.95	45.35, 10.73	4525.57	7
Sentinel-1A	4542	439	2015-02-09T05:18:50	46.58, 14.41	46.98, 11.09	44.95, 13.95	45.35, 10.73	8364.73	7
Sentinel-1A	4367	439	2015-01-28T05:18:51	46.59, 14.38	46.98, 11.10	44.95, 13.91	45.35, 10.73	8148.96	6
Sentinel-1A	4017	440	2015-01-04T05:18:57	46.26, 14.28	46.65, 11.02	44.62, 13.82	45.02, 10.65	8148.56	8
Sentinel-1A	3842	439	2014-12-23T05:18:51	46.59, 14.38	46.98, 11.09	44.95, 13.91	45.35, 10.73	8148.87	7
Sentinel-1A	3492	439	2014-11-29T05:18:52	46.59, 14.38	46.98, 11.09	44.96, 13.91	45.35, 10.73	8149.03	5
Sentinel-1A	3317	439	2014-11-17T05:18:53	46.59, 14.38	46.98, 11.09	44.95, 13.91	45.35, 10.73	8148.82	5
Sentinel-1A	2967	443	2014-10-24T05:19:15	45.32, 14.02	45.72, 10.78	43.68, 13.56	44.07, 10.42	8502.72	5
Sentinel-1A	2967	438	2014-10-24T05:18:50	46.81, 14.43	47.21, 11.11	45.17, 13.96	45.56, 10.74	4650.68	5
Sentinel-1A	2792	443	2014-10-12T05:19:14	45.32, 14.02	45.72, 10.78	43.68, 13.56	44.07, 10.42	4403.02	5
Sentinel-1A	2792	438	2014-10-12T05:18:50	46.81, 14.44	47.21, 11.11	45.17, 13.97	45.56, 10.74	4670.80	5

NB:

Acq. is for acquired,

NS is for Near Start,

FS is for Far Start,

NE is for Near End,

FE is for Far End part of the SLC image and

R for Redundancy of images in the set of interferograms.

A5 Map of candidate measurement points & unwrapped phases

Figure A5.4: Map of selected points by the omega factor, from the Barcelona case area, Spain.

Figure A5.5: Map of unwrapped phases, from the Venice lagoon case area, Italy.